UNIVERSITÄT ZU LÜBECK
INSTITUTE OF MEDICAL ENGINEERING

From the Institute of Medical Engineering
of the University of Lübeck
Director: Prof. Dr. rer. nat. Thorsten M. Buzug

Measurement Biases in Double Diffusion Encoding Magnetic Resonance Imaging

Dissertation
for Fulfilment of
Requirements
for the Doctoral Degree
of the University of Lübeck

from the Section Informatics/Engineering

Submitted by

Patricia R. Ulloa Almendras
from Concepción, Chile

Lübeck 2021

First referee: Prof. Dr. rer. nat. Martin A. Koch
Second referee: Prof. Dr.-Ing. Alfred Mertins
Date of oral examination: 17 December 2021
Approved for printing. Lübeck, 3 January 2022

Acknowledgement

Throughout the course of the doctoral formation, I have received invaluable support and assistance. First I want to thank my supervisor, Prof. Martin Koch, for his great advice, continuous support and patience during my doctoral studies.

I would like to acknowledge the students that worked with me in specific DDE-related projects, Luise Preuße, Anastasia Benedik and Rabea Landmesser.

I am grateful to all the friends that supported me during the research and writing process. With special thanks to Vincent Methot, Pragathi Gurumurthy, Mariya S. Pravdivtseva and Isil Unal. For unconditional support, I thank my family, my parents and Thomas Friedrich.

I also want to thank the Graduate School for Computing in Medicine and Life Sciences at University of Lübeck funded by the German Excellence Initiative [DFG GSC 235/2-1], and German Research Foundation [DFG KO 3389/2-1] for financial support.

Abstract

Characterizing the microstructural properties of biological tissue is an important topic when understanding the processes involved in the brain's normal development, aging and disease. Invasive histology analysis is the current gold-standard when studying tissue. Diffusion-weighted MRI, which is performed by measuring the displacement of water molecules, appears as an attractive alternative to the invasive study of tissue microstructure.

Double diffusion encoding (DDE) is an extension of the classical diffusion-weighted technique, which can be used to non-invasively assess cellular size, shape and membrane permeability, characteristics that are important to determine, for example, grading of cancerous tissue. However, those characteristics are tangled together in the acquired data. This generates measurement biases, which affect the estimated microstructural parameters.

In this thesis, two measurement biases are studied. Firstly, it has been observed an overestimation in axonal diameters on the human corticospinal tract. This raises the question of the degree to which extra-axonal space contributes to size estimates based on DDE. Here, the fact that the DDE-weighted MR signal is also sensitive to pore shape is exploited. Measurements of excised porcine spinal cord and of *in vivo* human corticospinal tracts are presented. The results suggest that the size estimation based on DDE is likely to be considerably influenced by the extra-axonal compartment.

Secondly, it has been reported that DDE measurements can be related to molecular exchange in terms of apparent exchange rate (AXR). However, the effect of compartmental size has not been considered so far. Here, this effect is studied in simulations and experiments in a water-in-oil emulsion in absence of molecular exchange. Results showed that it is possible to estimate an AXR in a sample where no molecular exchange is expected due solely to the effect of compartmental size. It can be concluded that the effect of cell size is relevant, and it needs to be accounted for when studying samples with large size compartments.

Kurzfassung

Die Charakterisierung der mikrostrukturellen Eigenschaften von biologischem Gewebe ist ein wichtiges Thema, wenn es darum geht, die Prozesse zu verstehen, die bei der normalen Entwicklung des Gehirns, beim Altern oder bei Krankheiten ablaufen. Dafür ist die histologische Analyse der aktuelle Goldstandard. Die diffusionsgewichtete MRT, kann über die Messung der Verschiebung von Wassermolekülen, eine attraktive Alternative zur invasiven Untersuchung der Gewebemikrostruktur bieten.

Die doppelte Diffusionskodierung (DDE) ist eine Erweiterung der klassischen diffusionsgewichteten Technik, die zur nicht-invasiven Beurteilung von Zellgröße, -form und Membranpermeabilität verwendet werden kann. Diese Eigenschaften sind z.B. wichtig um das Grading von Krebsgewebe zu bestimmen. Allerdings werden die Parameter der Gewebemikrostruktur in den erfassten Daten miteinander vermengt, und dadurch werden Messergebnisse verzerrt, was die geschätzten Parameter beeinflussen kann.

In dieser Arbeit werden zwei Messverzerrungen untersucht. Erstens wurde eine wesentliche Überschätzung der Axonaldurchmesser im menschlichen kortikospinalen Trakt beobachtet, da der extraaxonale Raum möglicherweise zur Größenschätzung auf Basis der DDE beiträgt. Dazu werden Messungen von exzidiertem Schweinerückenmark und von menschlichen kortikospinalen Bahnen in vivo vorgestellt. Die Ergebnisse deuten darauf hin, dass die auf DDE basierende Größenabschätzung wahrscheinlich erheblich durch den extraaxonalen Raum beeinflusst wird.

Zweitens wurde berichtet, dass DDE-Messungen mit der scheinbaren Austauschrate in Beziehung gesetzt werden können. Da der Effekt der Kompartimentgröße bisher nicht berücksichtigt wurde, wird dieser Effekt nun in Simulationen und Experimenten in Abwesenheit von molekularem Austausch untersucht. Die Ergebnisse zeigen, dass es allein aufgrund des Effekts der Kompartimentgröße möglich ist, eine Austauschrate in einer Probe abzuschätzen, in der kein molekularer Austausch zu erwarten ist. Folglich spielt der Effekt der Zellgröße eine wesentliche Rolle bei der Untersuchung von Proben mit großen Kompartimenten.

Contents

1 Introduction

1.1 Introduction

Since the mid-1980s, diffusion-weighted magnetic resonance imaging (MRI) has become the mainstay of neuroimaging, especially in stroke imaging [1]. Molecular diffusion effects were first described by Hahn [2] back in 1950 in his paper titled "Spin echoes". He observed that the magnetic resonance (MR) signal in liquids was not only affected by T_1 and T_2 relaxation times, but also by self-diffusion of water molecules, which generate an additional attenuation in the signal. During the early stages of MR research, diffusion was an unwanted effect in the MR signal. It was not until Stejskal and Tanner [3] developed the pulsed field gradient technique that diffusion could be quantified in terms of apparent diffusion coefficient.

Nowadays, the applications of diffusion-weighted MRI in the area of neuroradiology are remarkable. Changes in diffusion properties are known to represent microstructural characteristics in biological tissue, revealing them as changes in the apparent diffusion coefficient. It is not necessary to use elaborated diffusion-weighted acquisition schemes. Even the simple average among three perpendicular gradient directions can be tremendously useful for clinical neuroradiology. In the brain, for example, changes in the diffusion coefficient imply an alteration in the tissue at a microscopic level. Such changes have

been observed in many neurological conditions such as a stroke [4, 5, 6] or tumors [7, 8]. Additionally, with the use of the Stejskal and Tanner sequence, it is possible to study diffusion employing a tensor model: diffusion tensor imaging (DTI) [9], where the tensor describes diffusion anisotropy, which allows assessing the neuronal tracts inside the brain [10, 11].

Even though the diffusion MRI signal is largely sensitive to several effects, it has one significant limitation: it is not specific. As an example, it can be said that after four decades of development, there is still no consensus on the origin of the observed drop in the diffusion coefficient in the brain areas affected by a stroke [12, 13].

Several approaches aim to provide more information on the origin of the diffusion-weighted signal based on the Stejskal and Tanner pulse sequence, such as acquisitions using multiple gradient strengths [14, 15] and/or multiple gradient directions [9, 16]. Even though there have been significant advances in that field, those techniques have reduced its applicability in *in vivo* studies due to high hardware requirements and long scanning times.

One major drawback is that the Stejskal and Tanner sequence methodology struggles to accurately characterize samples containing compartments with different sizes or shapes, and/or orientated in different directions, as in biological tissue studies [17]. To overcome this issue, it is possible to make several assumptions on the composition of the sample, such as amount and geometry of compartments, fiber orientation, and membrane permeability, among others [18]. However, this is usually not enough when imaging living tissue, or in the case of pathologies [19, 20, 21].

In the study of cancerous tissue, for example, the structure and function of the pathological cells are different from healthy ones [22]. In tissue samples, histopathological studies are focused in the detection of cell shape and size irregularities, and their distribution in tissue [23]. These microstructural characteristics change as cancer becomes more invasive [24]. Tissue biopsies and subsequent histological microscopy analysis of stained samples are the gold-standard in cancer grading [25, 26]. As biopsies and histology are invasive techniques, there is a need for the development of non-invasive approaches. Advanced diffusion-weighted MRI appears as an alternative to provide more specificity to the diffusion-weighted signal.

Double diffusion encoding (DDE) is a natural extension of the Stejskal and Tanner sequence, which aims to overcome the lack of specificity on the said sequence. In DDE, two pairs of diffusion encoding gradient pulses (instead of one, as in the Stejskal and Tanner sequence and, therefore, referred to as single diffusion encoding or SDE) are applied successively between excitation and acquisition. This new extension adds de-

grees of freedom which do not have an equivalent in SDE: the possibility of having two different diffusion-weightings in the same pulse sequence, vary the angle between the diffusion-weightings and the time between them (mixing time). This opens the possibilities to new experiments that could reveal more characteristics of tissue composition and microstructure. First introduced by Cory et al. [27], DDE appears as an alternative to overcome some intrinsic limitations of SDE in the characterization of samples with complex microstructural organization. In biological tissue, for example, it is difficult to infer compartment sizes and shape from SDE. However, by means of DDE it is possible to study the size and shape of the compartments in complex samples by varying the angle and the time between the diffusion wave-vectors, respectively. The theoretical background for this effect was later developed by Mitra [28], providing a new tool to study restricted diffusion, even in the presence of randomly oriented compartments which are eccentric in shape, with the use of clinically available gradient systems. Promising results have been published, from experiments carried out in humans *in vivo*, which aimed at non-invasive characterization of tissue [29, 30, 31].

Additionally, DDE has other applications apart from the study of compartmental size and shape. It could be used to investigate the molecular exchange between compartments in terms of apparent exchange rate (AXR) [32]. By increasing the time between the wave-vectors, the DDE sequence is sensitive to water exchange, which can be related to membrane permeability in living tissue. This is important because a cell's ability to control the membrane exchange is highly regulated [33]. Small molecules, such as ethanol, use passive trans-membrane diffusion driven by electric and solute concentration gradients and do not require energy [34]. The transport of water through the membrane is performed by aquaporins (AQP), which belong to a family of passive transport channels [35]. Aquaporins are essential in the cells' function [36]. In the kidneys, for example, AQPs control water reabsorption [37]. In a healthy brain, the AQPs may not play a major role during its normal function. However, they become relevant in case of an illness [36]. Several studies relate the expression of AQPs being affected in cancerous tissue [38, 39, 36]. Therefore, non-invasive imaging techniques to access molecular exchange are of medical interest. By means of DDE, filter exchange spectroscopy [40] and imaging [32] is possible to non-invasively estimate membrane permeability.

Even though DDE provides more specificity than SDE, it has been challenging to design an experimental set-up specific to each effect. Measurement biases in DDE MRI arise when different factors interfere with the measured diffusion-weighted signal, resulting in erroneous parameter estimation.

Published results using DDE have shown an overestimation in the compartment size es-

timates in the corticospinal tract (CST) in humans *in vivo* [29]. Then, the question that arises is: which compartment size is being measured? The intra- or the extracellular space? In this thesis, the DDE's sensitivity to compartment geometry is exploited in order to investigate the origin of the DDE signal in CST.

The estimation of molecular exchange has shown promising results *in vitro* [32, 41] and in humans *in vivo* [42, 43, 44, 45]. However, this measure has several biases that need to be considered. It was reported that microscopic anisotropy affects AXR estimations [46]. Additionally, differences in T_2 between intra- and extracellular space influence the results [47]. However, the effects of restriction in the AXR results have not been investigated yet. In this thesis, the effect of microscopic restriction and compartment size in AXR estimations are studied. Additionally, solutions are presented to cancel the contribution of restriction to AXR.

1.2 Published work

During her doctoral studies, the author published research in the area of double diffusion encoding at several international conferences. Research on the origin of the DDE MR signal in the CST was published at the 48$^{\text{th}}$ annual conference of the German Society for Biomedical Engineering (DGBMT) (October 2014, Hannover - Germany) [U1], at the 49$^{\text{th}}$ annual conference of the DGBMT (September 2015, Lübeck - Germany) [U2], and at the 23$^{\text{rd}}$ annual meeting of the International Society for Magnetic Resonance in Medicine (ISMRM) (April 2015, Toronto - Canada) [U3].

Also, a water-in-oil emulsion as a phantom for validation of DDE sequences[1] was developed and presented during the 33$^{\text{rd}}$ annual scientific meeting of the European Society for Magnetic Resonance in Medicine and Biology (ESMRMB) (September 2016, Vienna - Austria) [U4]. The work obtained a certificate of merit poster award at the conference. The simulation results of the study of the bias in the apparent exchange measurements were presented at the 25$^{\text{th}}$ annual meeting of the ISMRM (April 2017, Honolulu - United States of America) [U5], where the study obtained a Magna cum laude merit award.
The experimental results were presented at the 51$^{\text{st}}$ annual conference of the DGBMT (September 2017, Dresden - Germany) [U6], and at the 34$^{\text{th}}$ annual scientific meeting of the ESMRMB (October 2017, Barcelona - Spain) [U7]. Additionally, the author participated other collaborative projects in the area of diffusion-weighted MRI [U8, U9, U10, U11], in 4D-Flow MRI [U12, U13, U14, U15, U16, U17, U18, U19] and other MRI related topics [U20, U21, U22, U23].

[1] Bachelor internship Anastasia Benedik and Rabea Landmesser, 2016

1.3 Aim of this thesis

This thesis aims to exploit double diffusion encoding (DDE) MRI sensitivity to pore shape, size and molecular exchange. The first objective is to obtain information on the origin of the DDE MR signal in the CST in humans *in vivo*. The second objective is to determine at what level the restriction effect affects the apparent exchange rate in the estimation of membrane permeability.

The organization of this thesis is as follow:

Chapter 2 introduces the basic concepts of magnetic resonance imaging, physical basics of diffusion and diffusion-weighted MRI.

Chapter 3 describes the implementation of the DDE sequences used in this work on a 3 T Philips clinical MR system.

Chapter 4 addresses the first objective of this thesis: the study of the extracellular contribution to the DDE signal.

Chapter 5 addresses the second objective for this thesis: the bias in apparent exchange rate measurement.

Chapter 6 summarizes the contributions and results of this thesis from a general point of view. Common pitfalls present in DDE experiments are discussed. In addition, possible future extensions are also presented.

2

Fundamentals

2.1 NMR basics

The atomic nucleus is conformed of protons and neutrons, which have an intrinsic angular momentum, or spin. The interaction between an external magnetic field and nuclei with a non-zero magnetic moment is the basis of nuclear magnetic resonance (NMR). Given that water constitutes around 60% of the human body and approximately 73% of the human brain [48], hydrogen (H^1) is the nucleus of choice for NMR and magnetic resonance imaging (MRI), particularly in human studies. The research presented here is restricted to the hydrogen nucleus, which is a $\frac{1}{2}$-spin particle.

The angular momentum, **J**, generates a nuclear magnetic dipole, or magnetic moment, which is represented by a vector μ. These two vectors are related as

$$\mu = \gamma \mathbf{J}, \tag{2.1}$$

where γ is a constant called gyromagnetic ratio. In the case of hydrogen, γ corresponds to $2.675\,10^8$ $s^{-1}T^{-1}$. The definition of the magnitude of the magnetic moment ($\|\mu\| = \mu$), based on quantum mechanics, is

$$\mu = \gamma\hbar\sqrt{\mathrm{I}(\mathrm{I}+1)}, \tag{2.2}$$

where $\hbar$ is Planck's constant ($h = 6{,}6\,10^{-34}$ kg m^2 s^{-1}) divided by 2π and I is the spin

quantum number of the studied nucleus. In the case of hydrogen, $\mathrm{I} = \frac{1}{2}$. However, the direction of μ is completely random due to thermal motion at thermal equilibrium. It is in the presence of a strong external magnetic field, $\mathbf{B}_0$, that the magnetic moment of individual spins can be analyzed macroscopically. Following conventions, $\mathbf{B}_0$ is applied in the z-direction. Then, in case of $\frac{2}{1}$-spin system, there are two possible orientations for μ of individual spins: in direction of $\mathbf{B}_0$ (in a low energy state, $\mathrm{N}_\uparrow$), or in opposite direction (in a high energy state, $\mathrm{N}_\downarrow$). According to the laws of thermodynamics, the number of spins $\mathrm{N}_\uparrow$ in low energy state is slightly larger than the number of spins $\mathrm{N}_\downarrow$ in high energy state, resulting in a bulk magnetization. The bulk magnetization vector, $\mathbf{M}$, corresponds to the volume density of magnetic moments. This collective behavior of nuclei can be accurately described using classical mechanics [49]. Therefore, $\mathbf{M}$ is the classical magnetic moment vector that precesses about $\mathbf{B}_0$. The angular frequency of that nuclear precession, also called Larmor frequency, is

$$\omega_0 = \gamma B_0, \tag{2.3}$$

where $B_0 = \|\mathbf{B}_0\|$. In Eq. (2.3), when B_0 is not homogeneous, the spins with the same γ will have spatially depending Larmor frequencies.

2.1.1 NMR signal generation

Consider a scenario in which the protons of hydrogen atoms are precessing about an external magnetic field, $\mathbf{B}_0$, applied in the z-direction. This magnetized system corresponds to the sum of the individual spin of an object giving rise to a macroscopic magnetization vector $\mathbf{M}$ along the z-axis, where $\mathbf{M} = (M_x, M_y, M_z)$.

The Bloch equations [50, 51] describe the behavior of $\mathbf{M}$ in the of a presence magnetic field, $\mathbf{B}(t)$, as in

$$\frac{d\mathbf{M}(t)}{dt} = \gamma \mathbf{M}(t) \times \mathbf{B}(t). \tag{2.4}$$

Then, considering the constant magnetic field $\mathbf{B}_0$ applied along the z-axis in Eq. (2.4), the three components of the magnetization are

$$\begin{aligned} \frac{dM_x}{dt} &= \gamma M_y \mathbf{B}_0, \\ \frac{dM_y}{dt} &= -\gamma M_x \mathbf{B}_0, \\ \frac{dM_z}{dt} &= 0. \end{aligned} \tag{2.5}$$

Therefore, the magnetization of the spin system can be manipulated by additionally applying a time-varying magnetic field, $\mathbf{B}_1(t)$.

The $\mathbf{B}_1(t)$ field can be characterized by means of three parameters: envelope function, oscillating frequency and phase angle. The envelope function, $B_1^e(t)$, determines the shape and the duration of the pulse. The oscillating frequency, ω_{RF}, is the excitation frequency of the system, meaning the Larmor frequency ($\omega_{\text{RF}} = \omega_0$). Then, the effective $\mathbf{B}_1(t)$ field takes the form

$$\mathbf{B}_1(t) = \begin{bmatrix} B_1^e(t)\cos(\omega_{\text{RF}}\, t + \phi) \\ B_1^e(t)\sin(\omega_{\text{RF}}\, t + \phi) \\ 0 \end{bmatrix}, \tag{2.6}$$

when applied along the x-axis, where ϕ is the phase angle, which in this explanation is considered to be constant (zero). Then, superimposing $\mathbf{B}_0$, Eq. (2.4) can be rewritten as

$$\frac{d\mathbf{M}(t)}{dt} = \gamma \mathbf{M}(t) \times \begin{bmatrix} B_1^e(t)\cos(\omega_{\text{RF}}\, t) \\ B_1^e(t)\sin(\omega_{\text{RF}}\, t) \\ B_0 \end{bmatrix}. \tag{2.7}$$

Equation (2.7) describes the effects of applying an oscillating magnetic field $\mathbf{B}_1(t)$ to the bulk magnetization vector $\mathbf{M}$ in the presence of a strong external magnetic field $\mathbf{B}_0$. This process is called excitation.

So far, the effects of the magnetic field over the bulk magnetization vector have been described using the “laboratory frame of reference" as illustrated in Fig. 2.1 A (with orthogonal axes x, y, and z). However, this coordinate system is static, while $\mathbf{M}$ and $\mathbf{B}_1(t)$ are not, making the system difficult to analyze. Therefore, the excitation process is better explained using the rotating frame of reference (with orthogonal axes x', y', and z') as illustrated in Fig. 2.1 B. In this coordinate system, in the case of hydrogen, the x'-y'-plane rotates clockwise with a specific ω. The rotating frame can usually have two angular frequencies: $\omega = \omega_{\text{RF}}$, where the $x'y'$-plane rotates with the frequency of $\mathbf{B}_1(t)$, or $\omega = \omega_0$. Usually ω_{RF} corresponds to ω_0. Then, the time-varying $\mathbf{B}_1(t)$ in the laboratory frame becomes stationary $\mathbf{B}_1$ in the rotating frame.

In the rotating frame of reference, $\mathbf{B}_1$ tips the magnetization vector away from the direction of $\mathbf{B}_0$ with an angle that is determined by the characteristics of the RF pulse (flip angle). For example, if a RF excitation pulse is applied along the x'-axis. Then, immediately after the pulse, the M_z component of the bulk magnetization vector is zero, while the magnetization in the x'-y'-plane appears as $M_{y'} = M_0$. Finally, the excited system will begin to return to its equilibrium state after the RF pulse. This process is called relaxation. The time needed for the system to return to equilibrium is described in two time constants: longitudinal relaxation or T_1 and transverse relaxation or T_2. The time to recover the M_z component (longitudinal relaxation) until approximately 63% corresponds

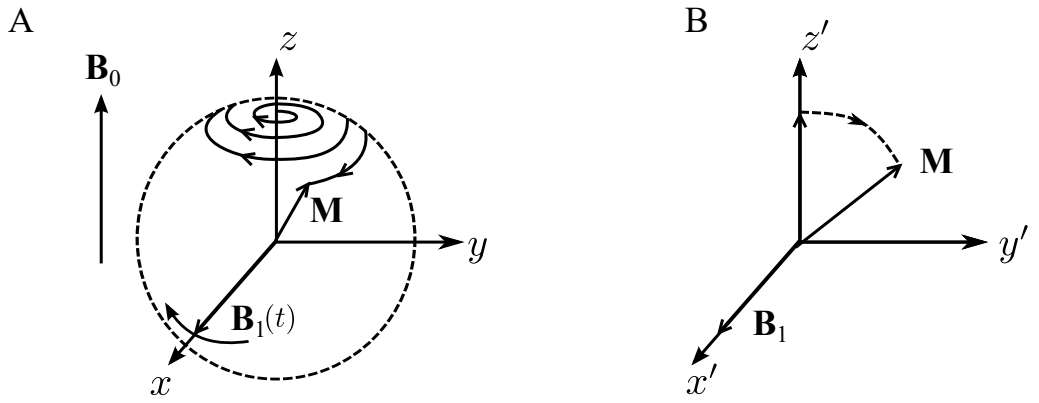

Figure 2.1: Effects of an excitation pulse. **A)** Laboratory frame of reference: $\mathbf{M}$ precesses about the z-axis and $\mathbf{B}_1$ oscillates with the Larmor frequency. **B)** Rotating frame of reference: $x'y'$-plane rotates with the Larmor frequency, making $\mathbf{M}$ and $\mathbf{B}_1$ appear static. Adapted from Liang and Lauterbur [52].

T_1. The time required for the extinction of the M_x and M_y components (transverse relaxation) until approximately 37% corresponds to T_2. These are called relaxation times and are the basis for the MRI signal contrast.

2.1.2 Bloch equations and relaxation processes

The Bloch equations [50] describe the time-dependent behavior of $\mathbf{M}$ in the presence of an external magnetic field $\mathbf{B}$. Including relaxation effects, Eq. (2.4) takes the form

$$\begin{aligned}
\frac{dM_x}{dt} &= \gamma(\mathbf{M}\times\mathbf{B})_x - \frac{M_x}{T_2} \\
\frac{dM_y}{dt} &= \gamma(\mathbf{M}\times\mathbf{B})_y - \frac{M_y}{T_2} \\
\frac{dM_z}{dt} &= \gamma(\mathbf{M}\times\mathbf{B})_z - \frac{M_z - M_0}{T_1},
\end{aligned} \tag{2.8}$$

where M_0 is the thermal equilibrium value for $\mathbf{M}$ in the presence of only $\mathbf{B}_0$, and T_1 and T_2 are time constants that describe the relaxation process of a spin system from excitation (immediately after the RF pulse) to thermal equilibrium. If $\mathbf{M}$ is disturbed from its equilibrium state (excited) then, immediately after the excitation RF pulse, $\mathbf{M}$ tends to realign with the remaining magnetic field. The time constant for longitudinal relaxation, or T_1, is a measurement of the recovery of the M_z magnetization, and the transverse relaxation, or T_2, measures the decay of the magnetization M_x and M_y. In the

rotating frame of reference, both processes follow an exponential decay

$$\begin{aligned} M_{x'y'}(t) &= M_{x'y'}(0_+)\exp(-t/T_2) \\ M_{z'}(t) &= M_z^0\big(1-\exp(-t/T_1)\big) + M_{z'}(0_+)\exp(-t/T_1), \end{aligned} \tag{2.9}$$

where $M_{x'y'}(0_+)$ is the maximum transverse magnetization observed immediately after the excitation, and M_z^0 and $M_{z'}(0_+)$ are the magnetization along the z'-axis before and after the RF pulse, respectively.

2.1.3 Signal detection

MR measurements require the magnetization vector to have a transverse component, which precesses about the z-axis and induces an oscillating voltage in a receiver coil, called free induction decay (FID). However, the NMR signal dephases due to magnetic field inhomogeneities as well, and the resulting FID, in practice, decays much faster than expected for the T_2 relaxation only. The decay due to inhomogeneities in the magnetic field can be characterized with a new time constant, T_2'. Then, the relation between those two effects is

$$\frac{1}{T_2^*} = \frac{1}{T_2} + \frac{1}{T_2'} \tag{2.10}$$

where T_2^* is called apparent relaxation time.

2.1.3.1 The spin echo

Hahn [2] introduced the concept of *spin echo* to recover the loss of transverse magnetization after a single excitation pulse. The spin echo (SE) is the recovery of spin phase coherence which was lost during the FID. The SE appears when more than one RF pulse is applied consecutively and its amplitude follows a T_2 exponential decay as a function of time.

If after a time t, (after excitation), an 180° pulse is applied along the x'-axis (in the rotating frame of reference), then the magnetization vectors are rotated by 180° about the x'-axis. After another period t, the spins will rephase, this time aligned along the y'-axis. This process is called refocusing. The signal generated now is known as the spin echo (see Figure 2.2). The echo time (TE) is the period between the excitation pulse and the signal maximum of the echo ($2t$).

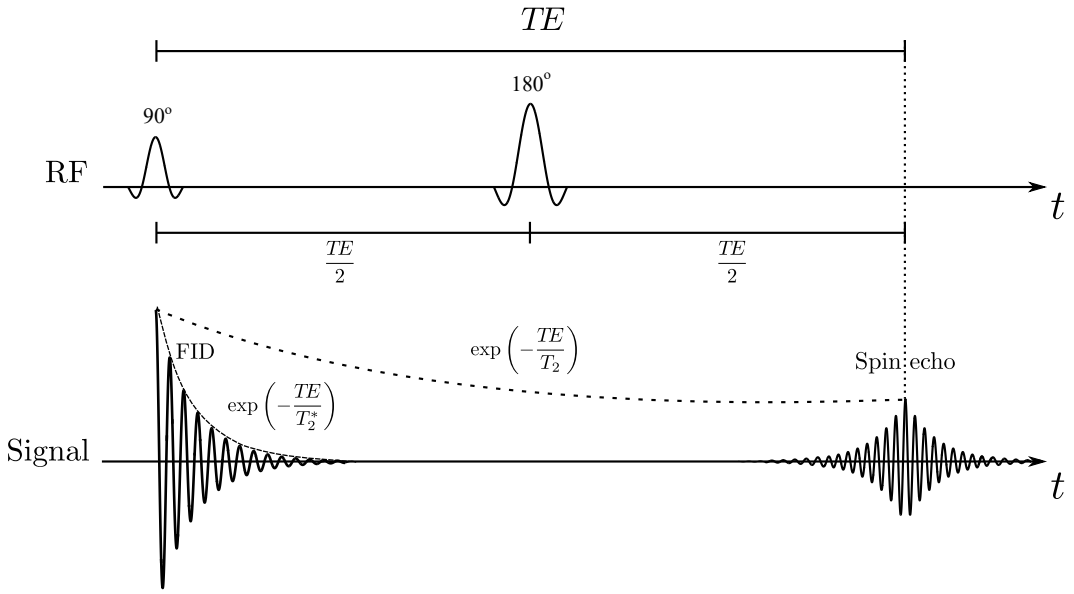

Figure 2.2: A spin echo is formed by one excitation pulse and one refocusing pulse. An FID is generated by the 90° (excitation) pulse. After a time t, a 180° (refocusing) pulse is applied and, after a second t period, a SE is observed. The FID generated by the excitation pulse follows a fast exponential decay that depends on T_2^*. The SE also has an exponential decay depending on T_2.

2.1.3.2 The stimulated echo

Whereas a pulse sequence with two RF pulses generates one SE, a sequence with three RF pulses generates a total of five echoes, out of which one is a stimulated echo (STE) (see Fig. 2.3). The STE arises from the combined effect of the three RF pulses.

Let us consider a sequence of three RF pulses in the rotating frame of reference. After the first RF pulse, the magnetization vector is flipped onto the transverse plane. The second RF pulse, besides generating a second FID, also creates the first SE of the pulse sequence, producing longitudinal magnetization. During the time between the second and the third RF pulses, the longitudinal magnetization is "stored" in the z'-axis. In that time, the magnetization is free from the effects of transverse relaxation, while under the effects of longitudinal relaxation. This "storage" effect is important when analyzing samples with short T_2, because it allows to use a longer TE while losing less signal than a sequence with only two RF pulses. The third RF pulse rotates the"stored" magnetization to the transverse plane, where it is once again affected by T_2 relaxation. The total number, N_E,

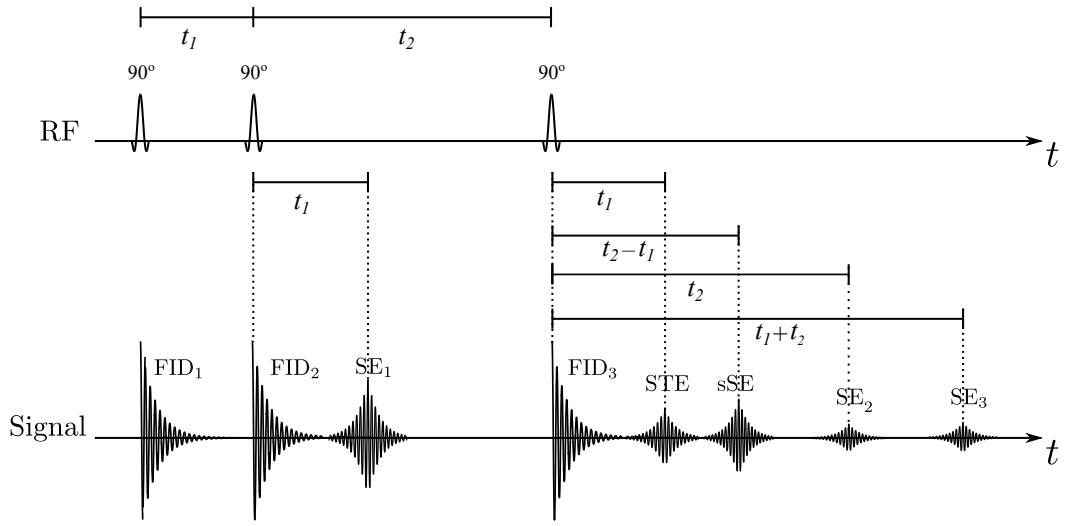

Figure 2.3: A three RF pulse sequence generates five echoes. The generation of the three primary echoes is due to the effect of the first RF pulse and the second RF pulse (SE_1), the effects of the second RF pulse and the third RF pulse (SE_2), and due to the effect of the first RF pulse and the third RF pulse (SE_3). The secondary echo (sSE) is formed by SE_1 and the third RF pulse. The stimulated echo (STE) is formed by the combined effects of the three RF pulses, in which the magnetization is stored during the t_2 period (also called TM).

of echoes generated by a sequence of N pulses can be calculated as

$$N_E = \frac{1}{2}\left(\frac{3^N - 1}{2} - N\right). \tag{2.11}$$

2.2 Magnetic resonance imaging

To reconstruct an image, the MR-generated signal needs to be spatially mapped. An MR image consists of a matrix of pixels, that pinpoint a specific region in an object. This is achieved by applying magnetic field gradients ($\mathbf{G} = G_x, G_y, G_z$). The Larmor frequency and phase depend on the spatial location of the nuclei of interest. For a 3 D object, the spatial encoding can be performed using slice-selection, frequency encoding (or read-out) and phase-encoding. Those gradients can be applied along any physical direction. Here, following conventions, these three steps are achieved by applying magnetic field gradients along z-, x- and y-axis, respectively.

2.2.1 Slice-selection

Slice-selection is achieved by applying an RF pulse in the presence of a magnetic field gradient, $\mathbf{G}_{\text{ss}}$. In the presence of $\mathbf{G}_{\text{ss}}$, the Larmor frequency can be rewritten as

$$\omega_0 = \gamma(B_0 + \mathbf{G}_{\text{ss}} \cdot \mathbf{r}), \tag{2.12}$$

where $\mathbf{r}$ is the displacement vector from the gradient isocenter. This generates a transverse magnetization distribution, called slice profile.The slice profile is determined by the envelope function, $B_1^e(t)$ in Eq. (2.6). If a slice in the xy-plane is wanted, then $\mathbf{G}_{\text{ss}}$ needs to be applied perpendicularly to that plane i.e., along the z-axis. The slice thickness Δz is determined by the pulse bandwidth ($\Delta\omega_{\text{RF}}$) and the amplitude of the slice-selection gradient ($\|\mathbf{G}_{\text{ss}}\| = G_{\text{ss}}$), as in

$$\Delta z = \frac{\Delta\omega_{\text{RF}}}{\gamma G_{\text{ss}}}. \tag{2.13}$$

2.2.2 Frequency-encoding

The frequency encoding gradient brings the spins out of phase, assigning different frequencies to different positions in the slice. If the slice-selection gradient is applied along the z-axis (to select a slice parallel to the xy-plane), then the frequency encoding gradient $\mathbf{G}_{\text{fe}}$ is typically applied along the x- or y-axis. In the presence of the main magnetic field $\mathbf{B}_0$, a frequency encoding magnetic field gradient is applied along the x-axis ($G_{\text{fe}} = G_x$). Then, the Larmor frequency at position x is

$$\omega_0(x) = \gamma(B_0 + G_x x) = \omega_{00} + \gamma G_x x, \tag{2.14}$$

where G_x is the amplitude of the frequency encoding gradient applied along the x-axis.

2.2.3 Phase-encoding

For the formation of an image, it is necessary to encode the signal in a third direction. As before, if the slice-selection gradient is applied along the z-axis, and the frequency encoding is applied along the x-axis (G_x), then the phase-encoding gradient ($\mathbf{G}_{\text{pe}}$) is applied perpendicular, along the y-axis ($\left\|\mathbf{G}_{\text{pe}}\right\| = G_y$). The phase-encoding gradient is applied before the frequency encoding during a short time, T_{pe}. During the $\mathbf{G}_{\text{pe}}$ application period, the signal acquires different phase angles linearly depending on the spin position along the y-axis. After T_{pe}, the signal has an initial phase angle

$$\phi(y) = -\gamma G_y y T_{\text{pe}}. \tag{2.15}$$

, where ϕ can be adjusted by varying the strength or duration of $\mathbf{G}_{\text{pe}}$.

2.2.4 k-space

After selecting a slice and applying frequency and phase-encoding, it is possible to form a 2 D image. The measured signal is sampled and organized in a discrete array of spatial frequencies. This array is known as k-space. The k-space is the Fourier transform of the proton density of the object being studied.

There are different schemes to sample k-space, also called trajectories. The Cartesian grid acquisition is the most popular technique to fill k-space [53, 54]. However, this trajectory is particularly time consuming, considering that every line in k-space requires a separated excitation pulse [53, 54]. To counteract this disadvantage, partial Fourier acquisition or parallel imaging are usually employed.

Echo planar imaging (EPI) [55, 56] is a fast imaging method to sample the k-space with one (or few) excitation pulses, also called "shots". This technique uses a series of gradient echoes as frequency encoding. A spin echo preparation with EPI read-out is shown in Fig. 2.4 A. In this manner, an echo train in which each echo corresponds to a line in k-space is generated as illustrated in Fig. 2.4 B. The phase-encoding"blips" (short duration and small amplitude gradient pulses) [57] mark the transition from one line to the next in k-space, reversing the read-out direction in each line.

The primary disadvantage of EPI is its sensitivity to magnetic field inhomogeneities (e.g., due to tissue-air interfaces or metallic objects), generating severe susceptibility artifacts [58]. System imperfections, like eddy currents or background gradients, can produce ghosting artifacts (or Nyquist ghosts) along the phase-encoding direction. Chemical shift artifacts are also present along the phase-encoding direction. Therefore, fat suppression techniques, like spectral presaturation with inversion recovery (SPIR) [59], are almost always required in EPI pulse sequences.

2.3 Diffusion

Brownian motion [60], also known as self-diffusion, is an essential physical process for living systems. Diffusion has been described using two approaches. A phenomenological view, which is described by Fick's laws of diffusion. Or a random-walk model for diffusing particles, which corresponds to Einstein's description of Brownian motion.

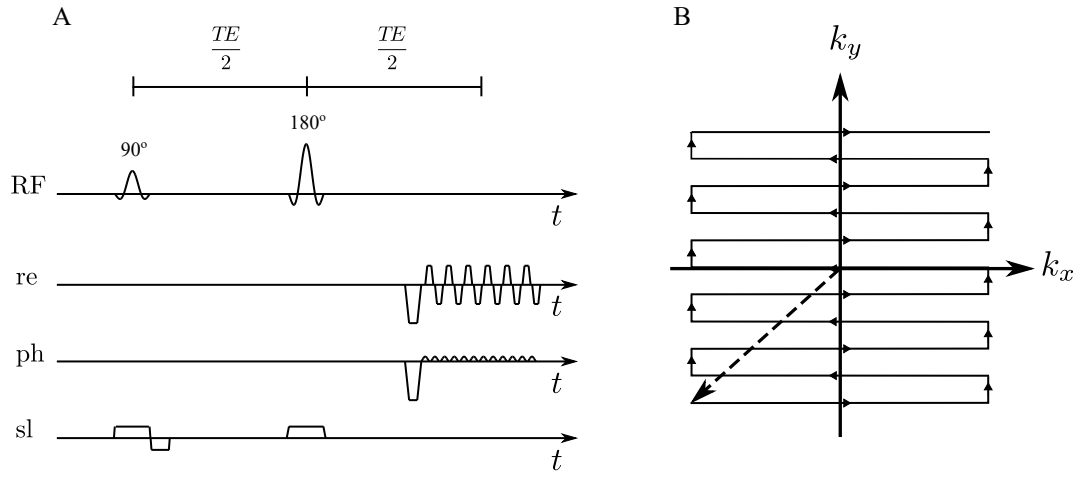

Figure 2.4: **A)** Spin echo sequence preparation with EPI read-out (re: read-out, ph: phase-encoding and sl: slice-selection). The RF time line shows the excitation and refocusing pulses. The read-out shows a series of bipolar frequency encoding gradients that generate a train of gradient echoes. The phase-encoding contains the gradient"blips", which mark the transition to the next line in k-space. The slice-selection time line illustrates the slice-selection gradients. **B)** k-space trajectory of the sequence in A. Arrows indicate the direction of the trajectory.

2.3.1 Phenomenological approach

In 1855, Fick [61] described the diffusion of molecules in the presence of a concentration gradient by

$$\mathbf{j}(\mathbf{r},t) = -D\nabla c(\mathbf{r},t), \tag{2.16}$$

where $\mathbf{j}(\mathbf{r},t)$ is the particle flux density at position $\mathbf{r}$ at time t, D is the diffusion coefficient, and $\nabla c(\mathbf{r},t)$ is the concentration gradient [62]. Equation (2.16) is known as Fick's first law. With increasing time, an irreversible flow of particles, from high to low concentration, will take place. This diffusion will continue until a steady-state is reached (when no concentration gradient is present).

Fick's second law is obtained by combining the continuity equation for mass

$$\frac{\partial c(\mathbf{r},t)}{\partial t} = -\nabla \cdot \mathbf{j}(\mathbf{r},t), \tag{2.17}$$

with Eq. (2.16) as in

$$\frac{\partial c(\mathbf{r},t)}{\partial t} = D\nabla^2 c(\mathbf{r},t). \tag{2.18}$$

Equation (2.18) is also known as the *diffusion equation*, which describes the diffusion process as the change of the concentration field over time. This equation is valid if

constant D is assumed, which is usually valid for diffusion in water. The fact that D is a scalar in Eq. (2.18) is indicative of isotropic diffusion.

However, in biological tissues, cellular microstructures can promote diffusion in a particular direction and hinder diffusion in another direction, resulting in anisotropic diffusion. For this reason, the diffusion tensor, **D**, is better suited to study anisotropic diffusion. The diffusion tensor, **D**, is a symmetric matrix which describes the relationship between molecular mobility (particle flux) and the probability gradient in any direction (displacement correlations). Then,

$$\mathbf{D} = \begin{bmatrix} D_{xx} & D_{xy} & D_{xz} \\ D_{yx} & D_{yy} & D_{yz} \\ D_{zx} & D_{zy} & D_{zz} \end{bmatrix}, \tag{2.19}$$

where the values of the tensor elements depend on the reference frame being used. The reference frame could be the frame defined by the diffusion measurement (i.e., the laboratory frame) or choosing a 3D rotation of the frame.

Then, Fick's first law (Eq. (2.16)) can be rewritten as

$$\mathbf{j}(\mathbf{r}, t) = -\mathbf{D}\nabla c(\mathbf{r}, t), \tag{2.20}$$

and Fick's second law (Eq. (2.18)) as

$$\frac{\partial c(\mathbf{r}, t)}{\partial t} = \nabla \cdot \mathbf{D}\nabla c(\mathbf{r}, t). \tag{2.21}$$

This is the basis of diffusion tensor imaging (DTI) MR, which will be explained in Section. 2.4.

2.3.1.1 Diffusion and Bloch-Torrey equation

In 1956, Torrey [63] incorporated the effects of diffusion from Fick's second law (Eq. (2.21)) into the phenomenological Bloch equations (Eq. (2.8))

$$\begin{aligned} \frac{\partial M_x}{\partial t} &= \gamma(\mathbf{M} \times \mathbf{B})_x - \frac{M_x}{T_2} + \nabla \cdot D\nabla(M_x - M_{x0}) \\ \frac{\partial M_y}{\partial t} &= \gamma(\mathbf{M} \times \mathbf{B})_y - \frac{M_y}{T_2} + \nabla \cdot D\nabla(M_y - M_{y0}) \\ \frac{\partial M_z}{\partial t} &= \gamma(\mathbf{M} \times \mathbf{B})_z - \frac{M_z - M_0}{T_1} + \nabla \cdot D\nabla(M_z - M_{z0}). \end{aligned} \tag{2.22}$$

Equation (2.22) is known as the Bloch-Torrey equation [63]. Stejskal [64] modified Torrey's approach in order to measure diffusion coefficients. This is the basis for the Stejskal and Tanner experiment, later referred to as single diffusion encoding. This experiment will be described in more depth in Section 2.4.1.

2.3.2 Random walk model approach and self-diffusion

While the phenomenological approach treated diffusion in a macroscopic way, the random walk model studies diffusion from the perspective of movement of microscopic molecules. In 1905, Einstein [65] related the molecular-kinetic theory of heat to observations made by Brown in terms of probabilities. He showed that the probability density, $p(\mathbf{r}, t)$, and the conditional probability density, $P(\mathbf{r}|\mathbf{r}_1, t)$, obey Fick's law. The probability density, $p(\mathbf{r}, t)$, represents a distribution of Brownian particle displacements over a time t, where $p(\mathbf{r}, t)d\mathbf{r}$ is the probability that $\mathbf{r}(t)$ (i.e. particle displacement) is in the range $\mathbf{r} < \mathbf{r}(t) \leqslant \mathbf{r} + d\mathbf{r}$. Then, it is possible to find the probability density at a time t_1, $p(\mathbf{r}_1, t_1)$, by integrating over all possible starting points

$$p(\mathbf{r}_1, t_1) = \int p(\mathbf{r}_0, 0) P(\mathbf{r}_0, t_0|\mathbf{r}_1, t_1) d\mathbf{r}_0, \tag{2.23}$$

where $\mathbf{r}$ is the starting coordinate and $\mathbf{r}_1$ is the final coordinate of a random particle, under arbitrary initial conditions, $p(\mathbf{r}_0, 0)$. As the diffusion is a Markovian process, where only the particle displacement (from $\mathbf{r}_0$ at t_0 to $\mathbf{r}_1$ at t_1) is important (not the time at the origin), $P(\mathbf{r}_0, t_0|\mathbf{r}_1, t_1)$ notation can be simplified to $P(\mathbf{r}_0|\mathbf{r}_1, t)$, where $t = t_1 - t_0$.

As $p(\mathbf{r}, t)$ obeys the diffusion equation (Fick's second law), then $P(\mathbf{r}|\mathbf{r}_1, t)$ also obeys Eq. (2.18)

$$\frac{\partial}{\partial t} P(\mathbf{r}|\mathbf{r}_1, t) = D\nabla^2 P(\mathbf{r}|\mathbf{r}_1, t). \tag{2.24}$$

where $P(\mathbf{r}|\mathbf{r}_1, t)$ is commonly referred to as Green's function or as the diffusion propagator [66]. Equation (2.24) is only valid for an isotropic medium (e.g., D is a scalar). In an anisotropic environment, D needs to be replaced by a diffusion tensor.

Then, under the assumption of an infinitely extended fluid, and given the initial condition in terms of a Dirac delta function (δ), $P(\mathbf{r}|\mathbf{r}_1, 0) = \delta(\mathbf{r}_1 - \mathbf{r})$. Therefore, Eq. (2.24) can be rewritten and simplified into [62]

$$P(\mathbf{r}|\mathbf{r}_1, t) = (4\pi D t)^{-3/2} \exp\left(- \frac{(\mathbf{r}_1 - \mathbf{r})^2}{4Dt} \right). \tag{2.25}$$

From Eq. (2.25) it can be seen that the diffusion propagator does not depend on the initial position of the particles, but rather on their net or dynamic displacement, $\langle(\mathbf{r} - \mathbf{r}_0)^2\rangle$,

$$\langle(\mathbf{r} - \mathbf{r}_0)^2\rangle = nDt, \tag{2.26}$$

where $\langle(\mathbf{r} - \mathbf{r}_0)^2\rangle$ corresponds to the ensemble average of all possible displacements, and $n = 2$, 4 or 6 for one, two or three dimensions, respectively [67]. Equation (2.26) is generally referred to as Einstein's equation [65] and it is equivalent to Fick's laws. This

equation assumes free diffusion in an infinite reservoir, where the molecular displacement varies linearly with increasing time.

However, in a system with impermeable compartments, where physical boundaries limit the motion of the molecules, Eq. (2.26) holds only when $t \to 0$, where the displacement of the molecules is so short that fewer particles are able to experience the boundaries. Nonetheless, for $t \to \infty$, the net displacement is constant due to the walls of the compartment. Then, Eq. (2.26) can be used to define a time-dependent diffusion coefficient as [68]

$$D(t) = \frac{\langle(\mathbf{r} - \mathbf{r}_0)^2\rangle}{nt}, \tag{2.27}$$

where $D(t)$ is also called effective diffusion coefficient, which calculates a diffusion coefficient by observing how far the particles have traveled in a fixed period of time.

As mentioned before, D in Eq. (2.24) needs to be replaced by a diffusion tensor (**D** as in Eq. (2.19) in case of anisotropic diffusion

$$\frac{\partial}{\partial t}P(\mathbf{r}|\mathbf{r}_1, t) = \nabla \cdot \mathbf{D}\nabla P(\mathbf{r}|\mathbf{r}_1, t). \tag{2.28}$$

Then, solving Eq. (2.28) results in [69]

$$P(\mathbf{r}|\mathbf{r}_1, t) = \frac{1}{(4\pi t\,|\mathbf{D}(t)|)^{3/2}} \exp\left(-\frac{(\mathbf{r}_1 - \mathbf{r})^T \mathbf{D}^{-1}(\mathbf{r}_1 - \mathbf{r})}{4\,t}\right), \tag{2.29}$$

where **|D|** is the determinant of **D** and T denotes transpose.

2.4 Diffusion-weighted MRI

The effects of molecular diffusion were detected during the early development stages of nuclear magnetic resonance technique. In 1946, Hahn [2] reported that in the case of molecules contained in low viscosity liquids, echo signal is attenuated not only due to the relaxation processes, but also to self-diffusion of the molecules.

In the beginning, diffusion was an unwanted effect on the MR signal. It was not until 1965, when Stejskal and Tanner [3] revolutionized the field with a technique that allowed to quantify the effects of diffusion. By applying a pair of gradient pulses before and after the radiofrequency pulse in a spin echo sequence, it was possible to sensitize the MR signal to the diffusion of water molecules within the tissue. In 1990, an important observation in diffusion-weighted MRI (DW-MRI) was done by Moseley et al. [1] while studying acute ischemia in cats. In that publication, a significant decrease in the measured apparent diffusion coefficient (ADC) is observed during the very early phase of acute

brain ischemia, while T_1- and T_2-weighted images showed limited information. This clinical application of DW-MRI attracted physicians, and implementation of diffusion-weighted MR sequences for clinical use began. Ever since, diffusion MRI has become an important technique for the study of the brain, reporting *in vivo* both anisotropy and microstructural information in neuronal tissue.

New diffusion MR techniques have been developed in the last decades. In 1990, and for the first time, Cory et al. [27] proposed the use of two diffusion encoding periods between excitation and acquisition, in order to study microstructural properties which are not easily available using non-invasive techniques. Henceforth, the Stejskal and Tanner experiment will be referred to as single diffusion encoding (SDE), while sequences containing two diffusion encoding periods will be referred to as double diffusion encoding (DDE), following the conventions from Shemesh et al. [70].

2.4.1 Single diffusion encoding

SDE is the most commonly used method of diffusion-weighting, both in clinical and research MRI [3, 71]. This method uses one pair of diffusion sensitizing gradient pulses with amplitude G and duration δ, separated by a time interval Δ. In a spin echo sequence, after the excitation pulse, the spins begin to dephase due to T_2 relaxation. The first diffusion gradient pulse alters the Larmor frequency and phase of the precessing spin, $\phi(t)$, according to

$$\phi(t) = \int_0^t \Delta\omega \, dt' = \gamma \int_0^t \mathbf{G}(t') \cdot \mathbf{r}(t') \, dt', \tag{2.30}$$

where $\phi(t)$ is the accumulated phase over time, $\Delta\omega$ is the change in resonance frequency, γ is the gyromagnetic ratio and $\mathbf{r}(t)$ is the spatial displacement of the spins. In the case of stationary molecules, the MR signal is only affected by relaxation process. However, mobile molecules do not maintain their original position during measurement. This leads to signal attenuation not only due to T_2 relaxation, but also to partial dephasing which arises from molecular diffusion. The diffusion-weighted signal, $S(b)$, is exponentially related to the phase of the precessing spins. Then, $S(b)$ in case of isotropic systems and in absence of net flow, is given by [64]

$$S(b) = S_0 \langle e^{-i\phi(t)} \rangle = S_0 \, e^{-bD}, \tag{2.31}$$

where $\langle e^{-i\phi} \rangle$ is the averaged phase dispersion of the spins, and S_0 is the MR signal from an identical sequence, only without diffusion gradient pulses. D is the diffusion coefficient, and b (in case of rectangular gradients) is [72, 73]

$$b = (\gamma \, G\delta)^2 t_d, \tag{2.32}$$

where δ is the duration of the diffusion gradients, $G = \|\mathbf{G}\|$. The diffusion time, t_d, is defined as $t_d = (\Delta - \frac{1}{3}\delta)$, where Δ corresponds to the time between the two gradient pulses, as shown in Fig. 2.5. The b-value [73, 74] is the degree of sensitization of the sequence to the effects of diffusion.

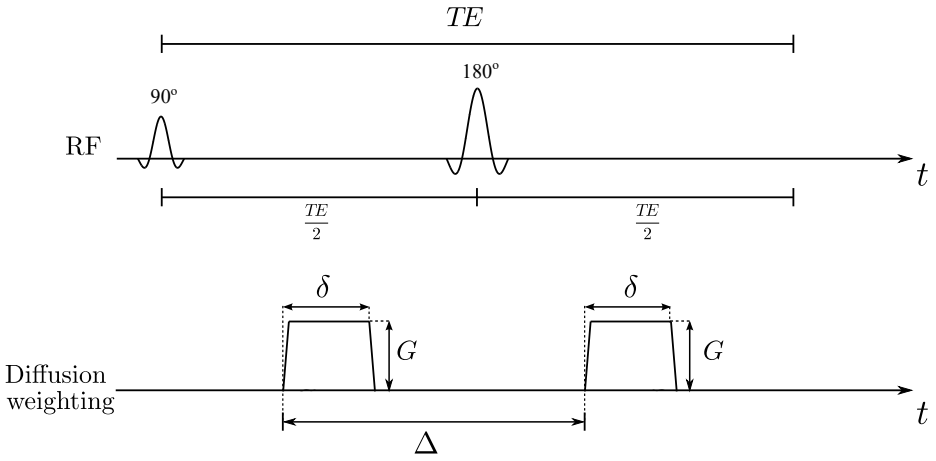

Figure 2.5: Schematic representation of the single diffusion encoding sequence in a spin echo preparation. The RF timeline contains an excitation pulse and a refocusing pulse. The diffusion weighting is shown in the timeline below with two identical gradient pulses of strength G, with pulse spacing Δ, and duration δ positioned before and after the refocusing pulse.

However, in an anisotropic system, as with biological tissues, phase distribution is no longer Gaussian due to the presence of barriers that interfere with the diffusion process, and only an apparent diffusion coefficient, ADC, can be defined using [3]

$$E(b) = \frac{S(b)}{S_0} = e^{-bADC}, \tag{2.33}$$

where $E(b)$ is the signal attenuation due to diffusion.

The concept of apparent diffusion coefficient was first introduced by Woessner [68], which represents the molecular self-diffusion coefficient. However, diffusion-weighted MRI is also sensitive to perfusion, which appears as pseudo-diffusion in this method. Intravoxel incoherent motion (IVIM) [73] is a manner to include all molecular displacements to which diffusion MRI may be sensitive.

When looking at isotropic diffusion due to restriction, the direction in which diffusion gradients are applied is irrelevant, and the signal will still obey Eq. (2.31). However, when speaking about anisotropic diffusion due to restriction, the diffusion-weighted signal depends on the direction of applied gradients and on the diffusion time [75]. Directional dependence of ADC was first reported in the human brain by Doran et al. [76] and

Chenevert et al. [77]. Consequently, it is essential to use multiple gradient directions in the study of anisotropic tissue.

In SDE it is possible to study diffusion using two approaches. The low b-regime, which includes DTI, and high b-regime, or q-space approach.

2.4.1.1 Diffusion tensor imaging

In anisotropic tissues, such as brain white matter, ADC varies with the tissue orientation with respect to the applied diffusion encoding, and vice versa. Stejskal [64] described the diffusion-weighted MR signal from anisotropic environments using a diffusion tensor. Diffusion tensor imaging, DTI, was proposed by Basser et al. [9, 69], making possible the study of diffusion anisotropy. Their approach helped to provide valuable microstructural information non-invasively [16].

In DTI, diagonal elements of the tensor in Eq. (2.19) correspond to diffusivities along three orthogonal axes (in the scanner reference frame), while the off-diagonal elements are the correlation of molecular displacements along those axes [78]. The tensor is represented by a 3×3 symmetric matrix, which describes molecular displacements along each axis and the correlation among those directions [64]. The b-value (a scalar) also needs to take on the form of a 3×3 symmetric matrix (b-matrix, $\mathbf{b}$), which is also expressed in terms of the scanner reference frame. If the scanner reference frame does correspond to the principal directions a sample diffusivity, the tensor is simplified to its diagonal terms. Those terms represent molecular displacements along the axes of the reference frame. However, in practice, the scanner reference frame does not coincide with the tissues's diffusion characteristics. Therefore, all elements of the tensor and $\mathbf{b}$-matrix need to be considered as in [9]

$$E(\mathbf{b}) = \frac{S(\mathbf{b})}{S_0} = e^{-b_{xx}D_{xx} - b_{yy}D_{yy} - b_{zz}D_{zz} - 2b_{xy}D_{xy} - 2b_{xz}D_{xz} - 2b_{yz}D_{yz}}. \tag{2.34}$$

To determine $\mathbf{D}$ using diffusion-weighted MRI, at least seven measurements are needed: one at lower b-value, b_0, (usually non-diffusion-weighted), and six with non-collinear, non-coplanar gradient orientations with $b \neq 0$. In practice, 20 to 30 isotropically distributed gradient directions are required for a robust estimation of parameters [79]. The optimal range of b-values for precise estimation of fiber orientation were determined by Alexander and Barker [80], with a range that lies between 700 and 1000 $\cdot 10^6$ s m^{-2}.

From the estimated $\mathbf{D}$, it is possible to perform an eigen decomposition of the diffusion tensor. Three eigenvalues, λ_1, λ_2 and λ_3, are used to characterize the shape and size of the diffusion tensor. Eigenvectors, $\hat{\mathbf{e}}_1$, $\hat{\mathbf{e}}_2$ and $\hat{\mathbf{e}}_3$ describe the orientation of the tensor, characterizing the diffusion anisotropy.

The simplest measurement that can be calculated from the **D** is the mean diffusivity (MD) [81], where

$$MD = \frac{1}{3}\text{Trace}(\mathbf{D}) = \frac{D_{xx} + D_{yy} + D_{zz}}{3} = \frac{\lambda_1 + \lambda_2 + \lambda_3}{3}, \tag{2.35}$$

and where λ_1, λ_2, and λ_3 are the tensor eigenvalues. This metric is a displacement average, and it is independent of the orientation of anisotropic pores within a voxel and gradient orientation. This parameter is of clinical relevance, particularly when monitoring stroke patients, as firstly shown by Warach et al. [82] in humans.

Fractional anisotropy (FA) [83] is a common measurement of a sample's degree of anisotropy, taking on values between 0 and 1, when diffusion is isotropic and limited along one axis only, respectively. It can be calculated as

$$FA = \sqrt{\frac{3}{2}}\frac{\sqrt{(\lambda_1 - MD)^2 + (\lambda_2 - MD)^2 + (\lambda_3 - MD)^2}}{\sqrt{\lambda_1^2 + \lambda_2^2 + \lambda_2^3}}. \tag{2.36}$$

Fiber tractography [69, 11, 84, 10, 85] in the brain is one of the most advanced clinical application of diffusion-weighted MRI, which in combination with functional MRI has opened a window into the study of functional connectivity [86].

However, the main limitation of DTI is its lack of specificity. Changes in the apparent diffusion tensor are sensitive to different simultaneous effects, such as membrane permeability, packing density, orientation distribution, and size and shape of cells. Therefore, it is difficult to associate the measurement of mean diffusivity and fractional anisotropy to a specific change in tissue structure [87]. As DTI completely characterizes diffusion using a three-dimensional Gaussian molecular displacement model, it does not correctly describe the displacement of spins trapped in closed pores [88, 89]. Additionally, in complex tissue structures (i.e., not coherently organized fiber orientations inside a voxel), the DTI voxel-average is not meaningful. This is especially critical in voxel containing crossing fibers in the brain.

2.4.1.2 q-space approach

DTI works under the assumption of Gaussian diffusion. However, it is well known that signal decay in confined spaces is not monoexponential at high b-values [14, 15, 90]. For restricted diffusion characterization in, e.g., neuronal tissue, a non-Gaussian molecular displacement distribution should be used.

The first analysis using q-space approach, which was firstly introduced by Callaghan [91], was performed by Cory and Garroway [92], showing that this method could provide additional structural information.

In q-space, it is necessary to define a reciprocal space

$$\mathbf{q} = (2\pi)^{-1}\gamma\delta G. \tag{2.37}$$

Then, it is possible to use the Fourier relationship between the MR signal decay due to diffusion and the 3 D displacement distribution function as

$$E_{\Delta}(\mathbf{q}) = \int \bar{P}_s(\mathbf{R}, t)e^{(i2\pi\mathbf{q}\cdot\mathbf{R})d\mathbf{R}}, \tag{2.38}$$

where $E_{\Delta}(\mathbf{q})$ is the signal attenuation as function of $\mathbf{q}$ for a specific Δ, $\mathbf{R} = \mathbf{r} - \mathbf{r}_0$ corresponds to the net displacement vector, while $\bar{P}_s(\mathbf{R}, t)$ is the averaged diffusion propagator. Then, applying the Fourier transform to Eq. (2.38), it is possible to determine a displacement distribution profile that can be used to extract microstructural information from heterogeneous systems [92, 15]. Therefore, the displacement distribution function can be characterized and quantified by means of the q-space approach, without any assumption on the tissues's diffusion characteristics.

Several applications of q-space imaging have been described in the literature. An example of q-space imaging was performed by Ong et al. [93], in which axon-diameter maps from an excised spinal cord sample were derived. This provided highly correlated results with histology. Another example shows that q-space imaging can detect changes in the maturation of rat's spinal cord. Changes in the displacement distribution function of axon myelination in rats have been identified as they age [88]. q-space imaging has proved to be sensitive to neuropathological conditions, such as myelin deficiency in rats [94]. Additionally, q-space imaging has improved detectability of experimental allergic encephalomyelitis in excised swine spinal cords [95], in accordance with histology. Such studies provided the possibility of performing a non-invasive "virtual histology" [17, 78].

The main advantage of q-space approach is that it provides a model-free way of obtaining a molecular displacement measurement, increasing the sensitivity to non-Gaussian diffusion. In this manner, q-space provides means to estimate the size of compartments. One approach to quantify the size of pores is by varying the diffusion time and keeping q constant [92]. A second approach is to keep the diffusion time constant and perform measurements in a range of q values [91].

However, one of its disadvantages is that it requires long acquisition times because the signal decay needs to be sampled at different q values. Additionally, such experiments require powerful gradients that are difficult to achieve in clinical MR systems [96]. To overcome these limitations, specific information on various compartments could be extracted by applying a model to the signal decay.

2.4.1.3 Models of diffusion in white matter

In q-space approach, the use of biophysical models to provide a geometrical representation of the tissue is a common practice, and depends on its application. In the case of white matter, different models have been suggested. One of the first models was proposed by Stanisz et al. [97] for the bovine optic nerve. They represented the tissue using three compartments. Glial cells are modeled as spheres, and axons are modeled as two prolate ellipsoids, one with a short dimension and a second with a long dimension, representing diffusion perpendicular and along to the fiber axis, respectively. Additionally, it includes membrane permeability, described by an exchange rate between intra- and extracellular compartments. The study estimates tissue characteristics which include diameter and length of axons and the diameter of glial cells. However, this study required careful positioning inside the scanner and high-quality MR data (SNR > 100). These characteristics are difficult to achieve *in vivo* in clinical scanners.

Behrens et al. [98] proposed a simpler two-compartment model: ball (isotropic diffusion) and stick (zero-radius cylinder), for extra- and intracellular axonal space, respectively. This approach can be extended to model multiple fiber orientations, by addition of more"sticks"[99]. However, as this model only considers diffusion along the sticks, and it does not take into account axial or radial diffusion. Therefore, it cannot provide microstructural information such as pore size.

The composite hindered and restricted model of diffusion (CHARMED) [100, 101] proposed a more realistic vision of the intra-axonal space: a distribution of cylinders, which is obtained from typical histological values in the spinal cord. The diffusion in white matter is modeled as restricted and hindered. Diffusion in the extracellular environment is considered hindered and characterized by a cylindrically symmetric diffusion ellipsoid, while the intra-axonal space assumes restricted diffusion within impermeable cylinders. This model can estimate fiber orientation, diffusivity inside and outside the fibers and respective volume fractions.

AxCaliber [102] is an extension of the CHARMED framework. AxCaliber can estimate an axon diameter distribution by assuming a Gamma distributed fiber orientation. This assumption is based on the histological work by Aboitiz et al. [103]. The data is acquired using multiple combinations of b- or q-values (also called "multiple shell" acquisition), where the diffusion gradients are always applied perpendicular to the fibers. Later, Barazany et al. [104] combined AxCaliber with imaging. In doing so, they presented the first *in vivo* non-invasive estimation of axonal diameter distribution in rat's *Corpus Callosum*, showing excellent agreement with histological analysis.

The critical assumption of previous models is that the fiber orientation is fixed and known,

perpendicular to applied diffusion gradients. For example, this condition can be satisfied in the spinal cord or in the *Corpus Callosum*. However, in other areas of the brain, where fiber crossing or fanning occurs, it would not be possible to apply gradients perpendicular to the fibers. Thus, a method that is rotationally invariant is needed.

While the previous methods require prior knowledge of the orientation of the axons or fiber, ActiveAx [105, 87] allows the estimation of axon diameter for unknown orientation distribution. Alexander et al. [87] combined the assumption of fibers as randomly packed identical cylinders with high angular resolution diffusion imaging (HARDI), providing a rotationally invariant estimate of a single axon diameter index [106]. However, a significant overestimation in the axon diameter index was observed during *in vivo* and *ex vivo* experiments [106].

2.4.1.4 Single diffusion encoding pitfalls

The MRI's ability to infer microstructure using restricted diffusion has been described here, so far, only using a Stejskal and Tanner sequence. Even though SDE has a vast variety of applications, such as fiber tracking in low q-regime and tissue characterization in high q-regime, it suffers a lack of specificity.

The SDE technique suffers from pitfalls when the sample under study has a complex structure. The problem arises in the characterization of heterogeneous systems where different microscopic features are entangled within the voxel. Therefore, SDE measurements can have difficulties in the characterization of samples with microstructures that include a distribution of compartment sizes and orientations. Under these circumstances, the q-space approach may result in an averaged pore size, especially due to hardware limitations where the duration of δ is long.

Additionally, samples containing randomly oriented anisotropic compartments will appear as isotropic in SDE measurements, losing important details in the microstructure information. This is especially relevant when referring to different orientations of neurites, dendrites and axons within the voxel. One approach to overcome this limitation is to apply a model that characterizes tissue properties.

Another critical issue to address is the need for strong diffusion gradients, since higher q-values are required to analyze smaller compartmental sizes. In addition, with increasing diffusion-weighing the signal-to-noise ratio decreases. These issues limit the applicability of q-space approach, even though it can provide relevant microstructural information. Additionally, the use of multiple shell acquisitions of different q-values make the diffusion MR measurements time consuming.

2.4.2 Double diffusion encoding

Double diffusion encoding (DDE) [70] (also known as double wave-vector (DWV) [107] or double pulse field gradient weighting (d-PFG) [108]) is an extension of the Stejskal and Tanner [3] experiment. This consists of the application of two diffusion-weighted periods between excitation and signal acquisition, separated by a mixing time. This kind of preparation has two pairs of diffusion gradient pulses, $\mathbf{G}^{(1)}$ and $\mathbf{G}^{(2)}$, with duration δ_1 and δ_2, and time between the gradient pulses Δ_1 and Δ_2 per diffusion-weighted period, as shown in Fig. 2.6. The corresponding $\mathbf{q}$ vectors for both encoding periods are $\mathbf{q}^{(1)} = \gamma\delta\mathbf{G}^{(1)}$ and $\mathbf{q}^{(2)} = \gamma\delta\mathbf{G}^{(2)}$, respectively. This new diffusion-weighting approach has several degrees of freedom: the direction and strength of each particular diffusion gradient, together with the gradient pulse duration and diffusion times, as in SDE. However, DDE incorporates two new parameters, namely mixing the time (τ_{m}) between the diffusion periods and the angle (ψ) between them, which do not have an equivalent in SDE. These new parameters provide the possibility to study molecular mobility at different gradient orientations and different time scales, improving the sensitivity of the diffusion-weighted signal to features that are difficult (or impossible) to reach using SDE. Figure 2.6 illustrates two different DDE pulse sequences, corresponding to a spin echo (Fig. 2.6 A) and to a stimulated echo preparation (Fig. 2.6 B), respectively. Figures 2.6 C and D illustrate the effective gradient waveform, coinciding with parallel ($\psi = 0$) and antiparallel ($\psi = \pi$) acquisitions following the conventions from Shemesh et al. [70].

DDE was first introduced by Cory et al. [27] as an alternative to study the effects of restricted diffusion in porous media. The theory behind this effect was developed by Mitra in 1995 [28], characterizing fully restricted diffusion in the low-q regime. Under idealized timing conditions, $\delta \ll \tau_{\mathrm{D}}$, $\tau_{\mathrm{D}} \ll \Delta$ (where $\tau_{\mathrm{D}} = a^2/2D$ is the mean time required by a spin to travel across a compartment or pore, a is the pore's size and D is the bulk diffusivity), Mitra [28] identified two limiting cases for the mixing time duration. Condition (i) considered long mixing time, $\tau_{\mathrm{m}} \to \infty$. Under this condition, Mitra predicted that for spherical compartments the diffusion-weighted signal will not depend on the angle between the diffusion-weighted periods. However, for eccentric pores, an angular dependence is expected. Therefore, it is possible to use DDE at $\tau_{\mathrm{m}} \to \infty$ to identify shape of compartments. Condition (ii) considered short mixing time, $\tau_{\mathrm{m}} = 0$. For vanishing mixing time, the diffusion signal will have a cosine dependence where the amplitude is proportional to the size of a compartment, independent of its shape. These two cases give access to microstructural information that is difficult or impossible to obtain using conventional diffusion MRI [109]. They will be analyzed afterward in the section 2.4.2.1 and section 2.4.2.2, for long and vanishing mixing time, respectively.

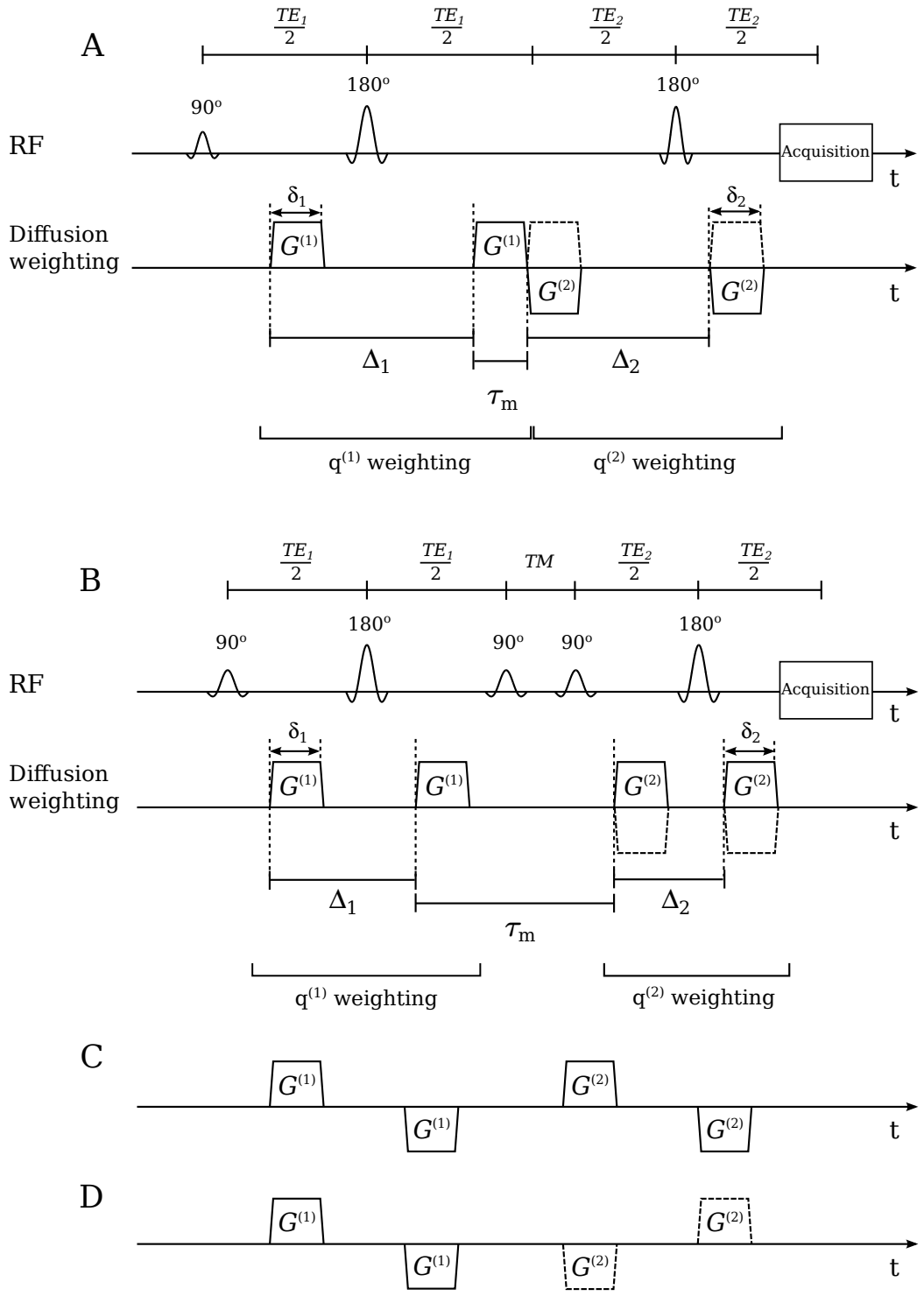

Figure 2.6: Double diffusion encoding pulse sequences. **A)** DDE spin echo sequence and **B)** DDE stimulated echo sequence. Solid lines show parallel gradient orientation ($\psi = 0$). Dashed lines represent antiparallel gradient orientation ($\psi = \pi$). **C)** Resulting waveform for parallel wave-vectors and **D)** resulting waveform for antiparallel wave-vectors, consistent with the definitions from Shemesh et al. [70].

Furthermore, DDE has been proposed as a technique to increase the sensitivity of the diffusion signal to water exchange between compartments [110, 40]. Diffusion exchange spectroscopy (DEXSY) was the first approach for molecular exchange rate measurement between compartments using DDE by Callaghan and Fur ó [110]. Later on, and based on the work in Ref. [110], Åslund et al. [40] developed filter-exchange spectroscopy (FEXSY), showing that exchange rates can be assessed in a sample with distinct compartments (yeast suspension). Based on filter exchange spectroscopy (FEXSI), Lasič et al. [32] implemented the imaging version of it, named filter exchange imaging (FEXI). They also introduced the concept of apparent exchange rate (AXR) as a method to estimate molecular exchange between compartments without assumptions on tissue characteristics. This method will be explained in more detail in section 2.4.2.3.

2.4.2.1 Microscopic anisotropy

"Microscopic anisotropy" is a controversial term, since it has been used to describe two different (but related) phenomena. Özarslan et al. [111] used this term to characterize local anisotropy induced by the presence of boundaries, e.g. cell membranes in biological tissue. In this definition, a spherical pore, as it has local anisotropy near the boundaries, is considered to be microscopic anisotropic, even though it is an isotropic compartment. The current definition for "microscopic anisotropy", following the naming conventions from Shemensh et al. [70], is related to diffusion that is anisotropic not due to the presence of boundaries, but to the shape of the compartment containing diffusing molecules as described by Callaghan and Furó [110] and Komlosh et al. [112]. Therefore, diffusion inside a spherical pore is not considered to have microscopic diffusion anisotropy. However, diffusion in eccentric pores is considered to be microscopic anisotropic. The terms compartment shape anisotropy [113], pore shape anisotropy [114] and apparent compartment shape eccentricity [115, 116] are equivalent to the current definition of "microscopic anisotropy" [70]. DDE experiments with long mixing times have been used for quantification of microscopic anisotropy in several phantom studies [117, 118, 119, 120] and in humans *in vivo* [121, 122, 123, 124, 125].

For further analysis let us assume an equal gradient strength for both diffusion-weighted periods, $\|\mathbf{G}^{(1)}\| = \|\mathbf{G}^{(2)}\| = G$. The gradient pulses have the same duration, $\delta_1 = \delta_2 = \delta$. The time between the gradient pulses is $\Delta_1 = \Delta_2 = \Delta$. Therefore, $\|\mathbf{q}^{(1)}\| = \|\mathbf{q}^{(2)}\| = q$.

For case (i) (i.e. $\Delta \rightarrow \infty$, $\delta \rightarrow 0$ and $\tau_{\mathrm{m}} \rightarrow \infty$), Mitra [28] considered heterogeneous media containing spherical or randomly oriented ellipsoidal pores. For spherical pores, Mitra predicted that DDE diffusion signal will not depend on the angle ψ between $\mathbf{q}^{(1)}$ and $\mathbf{q}^{(2)}$. However, there will be a signal difference between parallel ($\psi = 0$) and

perpendicular ($\psi = \pi/2$) diffusion gradients in the case of randomly oriented eccentric pores. This term arises from the fourth-order term in a power series of the DDE signal magnitude.

Later, Cheng and Cory [117] analyzed the parallel–perpendicular signal difference in a sample of yeast cells of different eccentricities at long mixing times, yielding the following expression for signal attenuation

$$E(q, \psi = 0) - E(q, \psi = \pi/2) = \frac{2}{375}(a^2 - b^2)^2 q^4, \tag{2.39}$$

where a and b denote the semi-major radii of the ellipsoids. In the case of spherical pores $a = b$, which vanishes the difference between parallel and perpendicular diffusion gradients.

It is important to note that this signal difference between perpendicular q is also present when the sample appears macroscopically isotropic, for example, due to isotropic orientation distribution of eccentric pores within a voxel [28, 108, 126]. This ability to detect microscopic anisotropy in samples that appear macroscopically isotropic is not available when using SDE.

The difference in the DDE signal attenuation when wave-vectors are perpendicular can be understood as explained by Finsterbusch [109]. He considered a mixture of two sets of anisotropic pores (u and v) with equal number of spins, perpendicular to each other and with diffusion coefficients D_u and D_v along orthogonal axes, respectively. In a DDE experiment with parallel or antiparallel diffusion periods, the obtained result is the same for both axes and is given by

$$E_{par} = \frac{1}{2}(e^{-bD_u} \cdot e^{-bD_u} + e^{-bD_v} \cdot e^{-bD_v}) \approx 1 - b(D_u + D_v) + b^2(D_u^2 + D_v^2), \tag{2.40}$$

where E_{par} corresponds to the DDE signal attenuation when $\psi = 0$ or $\psi = \pi$. This previous equation differs from a SDE experiment due to the effectively doubled diffusion weighting (b-value). However, in the case of perpendicular wave-vectors ($\psi = \pi/2$), the signal attenuation, E_{per}, is given by

$$E_{per} = e^{-bD_u} \cdot e^{-bD_v} = e^{-b(D_u + D_v)} \approx 1 - b(D_u + D_v) + \frac{1}{2}b^2(D_u + D_v)^2. \tag{2.41}$$

The signal attenuation difference between parallel and perpendicular orientations, $E_{par} - E_{per} = \frac{1}{2}b^2(D_u - D_v)^2$, is present for $D_u \neq D_v$ ($E_{par} > E_{per}$). This signal difference between parallel and perpendicular q's is not only present in cases of restricted diffusion but also when diffusion is hindered (like in extracellular space). DDE validation studies were performed in phantoms [127], in cells [121, 120, 119], rodents *in vivo* [119, 122, 128] and

in humans *in vivo* [123, 125]. A clinical application of microscopic anisotropy estimations via DDE was presented by Yang et al. [129]. They showed that DDE microscopic anisotropy derived metrics could better depict white matter lesions due to multiple sclerosis when compared with SDE.

2.4.2.2 Restriction effect and size estimates

In Mitra's case (ii) (i.e. $\Delta \to \infty$, $\delta \to 0$ and $\tau_{\mathrm{m}} = 0$) [28], the angular dependence of the DDE signal follows a negative cosine curve [130]. This can be characterized by a function that can be approximated to

$$\frac{S(q,\psi)}{S_0} = 1 - \frac{1}{3}q^2\langle R^2\rangle(2 - \cos(\psi)), \tag{2.42}$$

where $\langle R^2\rangle$ is the mean-squared radius of gyration of the pore, which is defined as the ensemble average of $\int \rho(\mathbf{r})(\mathbf{r} - \mathbf{r}_{\mathrm{com}})^2 d^3r / \int \rho(\mathbf{r}) d^3r$, where $\mathbf{r}_{\mathrm{com}}$ corresponds to the pore's center of mass and $\rho(\mathbf{r})$ to the mass' density. Then, for small values of q, the DDE signal attenuation for $\psi = 0$ (considering effective diffusion gradients) is $E_{par} = 1 - (\langle R^2\rangle/3)q^2$, and for $\psi = \pi$ is $E_{apar} = 1 - \langle R^2\rangle q^2$. Hence, the difference between parallel (E_{par}) and antiparallel (E_{apar}) signal attenuation provides a direct approach to the estimation of pores or compartments dimension. The cosine-shaped modulation reflects non-Gaussian diffusion and can be considered as a signature for restriction present in a sample [109]. Note that in Eq. (2.42) the factor $(2 - \cos(\psi))$ is not as in the original publication [28], because here the conventions from Shemesh et al. [70] are used. In the conventions paper for DDE nomenclature [70] the terms "parallel" and "antiparallel" are defined in terms of the effective wave-form. This considers the effect of RF pulses in the sign of the gradient pulses. Therefore, DDE experiments with $\mathbf{q}^{(1)} = \mathbf{q}^{(2)}$ correspond to $\psi = 0$ ("parallel").

The signal angular dependence will hold for any compartment shape (including spheres). Hereinafter, this effect will be referred to as "restriction effect" or "size effect". Finsterbusch [131] presented "phase-gymnastics" as an approach to intuitively explain the signal difference between parallel and antiparallel wave-vectors at short mixing times. In the case of free diffusion, no angular dependence of the MR signal is expected. However, in the case of restricted diffusion, from Eq. (2.42) it can be observed that the diffusion signal from antiparallel wave-vectors is reduced by a factor of $1/3$ in comparison with parallel wave-vector acquisition. To understand this behavior, Finsterbusch [131] considered restricted diffusion under the assumption of spins diffusing between two parallel planes and that the diffusion gradients are applied perpendicular to the planes. In this

explanation, effective wave-form of the diffusion gradients are assumed (a MR pulse sequence without refocusing pulses). For parallel wave-vectors, under the assumption that $\tau_m = \delta$ (no overlap between the inner gradients) and $\delta \to 0$ (the so called short gradient pulse (SGP) approximation), the inner gradient pulses have inverted polarities, canceling each other. This means that a DDE experiment with parallel wave-vectors is effectively an SDE measurement, with doubled diffusion time. However, as Δ is assumed to be long, additional time between the first and the fourth gradient pulse has no further effect in the diffusion-weighted MR signal. However, in the case of antiparallel wave-vectors, where the inner gradients have the same polarity, the diffusion-weighting is doubled.

It is important to note that ideal conditions from Mitra's theory are not met in a DDE acquisition protocol in clinical MR scanners. Therefore, experimental studies should consider finite sequence timing parameters, in order to avoid possible biases in the parameter's estimation [130]. Still, it has been shown that even when the short gradient pulse approximation is violated, it is possible to extract accurate size estimates in small compartments [130]. Özarslan et al. [108, 132] developed an approach that considers arbitrary timing parameters in the analysis of DDE signal for various geometries, which have shown to be more accurate in the estimation of compartment dimensions [130]. The DDE-based size estimation approach has been extensively studied theoretically [28, 108, 131], in computer simulations [126, 133, 134] and in phantoms [107, 135, 136]. They have shown promising results *ex vivo*[107, 137, 119, 138, 139] and *in vivo* [29, 31] applications

Nonetheless, the theoretical work of Jespersen [114] showed that in low-q regime the DDE and SDE provide equivalent information to determine pore dimensions. This is given because in both cases the diffusion signal can be related to a displacement correlation tensor [140], and this is possible to obtain using SDE acquisitions at different diffusion times. This was explained by Jespersen [141] by means of the experimental data presented by Morozov et al. [142], where the SDE signal in the same q-regime behaves as $S_{\text{SDE}} \approx 1 - q^2\langle R^2 \rangle$. This means that pore dimension can be calculated using different q values. This raises the question: is it worth the use DDE for pore size estimations instead of SDE? Taking into consideration that SDE is already implemented in clinical and preclinical MR scanner, it is easily accessible. Additionally, as SDE has one pair of diffusion gradients, the SNR is higher than the signal in a DDE sequence. Moreover, Jespersen [141] showed that size estimates using SDE or DDE have the same accuracy in size estimation in the presented phantom data. On the other hand, it has been shown that DDE may be a better tool to differentiate pores of different sizes in a sample [143]. Therefore, an advantage of DDE over SDE is its ability to determine pore size

distributions [144]. Additionally, DDE can be performed in a range of time-domains that would allow for studies that are sensitive to pore size and microscopic anisotropy in a single DDE acquisition. Microscopic anisotropy detection is not possible using SDE. Therefore, the most convenient diffusion-weighted approach will depend solely on the application's aim.

2.4.2.3 Molecular exchange

Molecular exchange across cell membranes is a highly regulated process. It helps regulate osmolarity inside the cell, and therefore, it is an essential process for normal physiological functions. Callaghan and Furó [110] first used DDE for molecular exchange, developing diffusion exchange spectroscopy (DEXSY) to study the diffusion properties across compartments. The method is based on the detection of the change in diffusion coefficients during molecular exchange. This is useful when studying systems in which molecules can be classified according to their diffusion characteristics. In DEXSY, the data is obtained by incrementing the gradient amplitude of both diffusion encoding periods. Δ_1 and Δ_2 need to be as short as possible, in order to neglect molecular exchange during that period. Hence, exchange occurs only during mixing time, τ_{m}. Several measurements are performed with increasing τ_{m}. Under the assumption that different compartments have different diffusion coefficients, the MR signal attenuation exhibits a multi-exponential decay. Therefore, in order to generate a spectrum of diffusion coefficients it is necessary to apply a 2 D inverse Laplace transformation. In the resulting 2 D spectrum, molecules that after several τ_{m} measurements did not move out of their original compartment will contribute to the diagonal elements of the DEXSY spectrum. However, those molecules that moved from one compartment to another contribute to the off-diagonal elements ("cross-peaks"), where their position corresponds to the affected volume fraction [110]. Nevertheless, the main limitation of DEXSY is that it requires long acquisition times.

Åslund et al. [40] based filter exchange spectroscopy (FEXSY) on the DEXSY method. As DEXSY, FEXSY uses two diffusion periods in a stimulated echo magnetization preparation (Fig. 2.6 B). However, the first diffusion-weighted block has a constant gradient amplitude in FEXSY, which acts as a diffusion filter for molecules with large ADC (fast diffusion). The optimization of this "filter block" is analogous to the Goldman-Shen sequence [145] or the double-quantum dipolar filter [146], in order to filter out rigid or mobile components, respectively. In the Goldman-Shen sequence [145] aims to separate slow- from fast- FID decaying components. These correspond to components with weak and strong dipolar coupling, respectively. Therefore, in order to filter the rigid components (fast-decaying), the parameters TE_1 and TE_2 need to be as short as possible. On

the contrary, with the double-quantum dipolar filter [147, 146] it is possible to select the signal arising from the most rigid components of a sample. This leads to the removal of the signal's mobiles components. This is achieved by setting up long values for TE. After the "filter block", molecular exchange between extra- and intracellular space occurs during the mixing time. Finally, during the second block, the amplitude of the diffusion gradients is incremented and the signal is measured as in a SDE experiment.

The theory of FEXSY considers a system with two compartments u and v, with diffusion coefficients D_u and D_v and fractional populations f_u^{eq} and f_v^{eq}. The relaxation rates of both compartments are assumed equal, and the sequence timing parameters are such that the exchange between compartments only occurs during τ_m and not during the Δ periods of the diffusion blocks ($\Delta \ll \tau_\mathrm{m}$). The exchange from u to v and vice versa is described with the rate constant k_{uv} and k_{vu}, respectively. The application of the filter block alters the system equilibrium, disturbing the fractional populations. This results in f_u^0 and $f_v^0 = 1 - f_u^0$. The system returns to equilibrium with increasing τ_m and the diffusion signal can be described as [40]

$$S(b, \tau_\mathrm{m}) = S_f(\tau_\mathrm{m})[f_u(\tau_\mathrm{m})e^{-bD_u} + f_v(\tau_\mathrm{m})e^{-bD_v}], \tag{2.43}$$

where $S_f(\tau_\mathrm{m})$ is the signal from an experiment with $G_2 = 0$, and $f_u(\tau_\mathrm{m})$ and $f_v(\tau_\mathrm{m})$ describe the evolution towards equilibrium. This method was tested by measuring the intracellular lifetime of baker's yeast cells [40].

Lasič et al. [32] implemented the imaging version of FEXSY, called filter exchange imaging (FEXI). There, the original protocol for FEXSY is optimized for low SNR conditions and hardware limitations (in particular gradient strength). The term "apparent exchange rate" (AXR) is introduced as a measurement of molecular exchange between compartments in heterogeneous media. In FEXI, Eq. (2.33) can be rewritten as

$$S(b, \tau_\mathrm{m}) = S_f(\tau_\mathrm{m})e^{-b\,ADC'(\tau_\mathrm{m})}, \tag{2.44}$$

where

$$ADC'(\tau_\mathrm{m}) = ADC[1 - \sigma e^{-AXR\cdot\tau_\mathrm{m}}]. \tag{2.45}$$

For a two-compartment system, $AXR = k_{uv} + k_{vu}$ and σ corresponds to the filter efficiency, defined as

$$\sigma = \frac{(D_u - D_v)(f_u^{eq} - f_v^0)}{ADC}. \tag{2.46}$$

Promising results have been published in estimating AXR in yeast cells [32], perfusion-fixated monkey brain [46], and in humans *in vivo* using clinical MR systems [42, 43, 44, 45].

2.4.2.4 DDE pulse sequences

DDE magnetic resonance (MR) sequences consist in the application of two diffusion-weighted periods between excitation and acquisition. In the literature, it is possible to find different magnetization preparations that contain two (or more) diffusion encoding. Spin echo preparations, consisting in one excitation and one refocusing pulse, with the diffusion gradient pulse pairs located before and after the refocusing pulse have been used principally in the study of microscopic anisotropy [123, 124, 125, 148, 149]. In this kind of pulse sequence, short mixing times are difficult to achieve. Given that the refocusing pulse separates the second and third gradient pulses, $\tau_{\mathrm{m}} = 0$ is impossible to reach. However, $\tau_{\mathrm{m}} = \delta$ may be possible to achieve depending on the duration of the diffusion gradients and other pulse sequence timing parameters, such as Δ and TE. An advantage of this magnetization preparation is that Δ can be short, which is convenient in cases where diffusion time is required to be as short as possible. This is the case during molecular exchange study. However, its applicability in that field is limited due to τ_{m} restrictions. This pulse sequence is appropriate to study the effects of microscopic anisotropy in diffusion-weighted signal, since short mixing times are not required. The viability of this pulse sequence in clinical routine has been under study. By implementing this pulse sequence in a clinical scanner, Yang et al. [30] proved its feasibility to detect microscopic anisotropy in patients *in vivo*. They observed a significant improved specificity in detecting microscopic anisotropy of DDE compared to the fractional anisotropy from SDE.

DDE pulse sequences with two refocusing pulses have been implemented mainly for the study of compartmental sizes [150, 107, 151, 152, 153, 135, 29, 121, 116, 128, 125, 142, 31]. In this pulse sequence, the diffusion gradients are applied before and after the refocusing pulses. The second and third diffusion gradients could be applied at the same time (allowing pulse gradient overlapping) or directly after the other. Therefore, it makes possible to reach short mixing times. However, it would allow a limited range of τ_{m}'s, depending on the timing parameters of the complete pulse sequence. The difference between parallel and antiparallel wave-vectors has been used to analyze the cosine signal modulation in order to extract compartmental dimensions. By means of this DDE pulse sequence, cell size estimates have been obtained in clinical scanners in rats [31] and in humans *in vivo* [29]. In the research performed in humans *in vivo* [29], the signal difference between antiparallel and parallel diffusion gradients was investigated in the corticospinal tract (CST). This resulted in a mean diameter estimation of 13 μm, which at first sight appears to be out of the expected size range of axons (1 to 3 μm) [154]. However, if the relative signal contributions of the axon volume is considered, then the

new mean size estimate is about 8 μm. The study shows the feasibility of DDE parallel–antiparallel signal difference to obtain compartment size estimates in humans *in vivo*. Nonetheless, there is an observed overestimation in the axonal diameters in CST using DDE. It was suggested that the extracellular space can be considered like "open pores", where hindered diffusion would influence the parallel–antiparallel signal difference, and thus, affecting the size estimates.

DDE stimulated echo preparations have applications in the study of microscopic anisotropy [27, 117, 127, 155] and in molecular exchange [110, 40, 32]. To make a diffusion-weighted measurement sensitive to exchange in SDE, it is necessary to increase the diffusion time to the time-scale in which molecular exchange takes place. However, when increasing the time between the diffusion gradients, the diffusion MR sequence also increase its sensitivity to restricted diffusion. Therefore, in SDE in long diffusion time regime, molecular exchange and restriction are entangled and inseparable effects. Additionally, increasing the diffusion time increases the echo time of the MR sequence, making the diffusion-weighted signal strongly influenced by T_2 relaxation. Thereby, in order to disentangle the effects of restriction and molecular exchange, the diffusion time should be kept as short as possible.

By implementing a stimulated echo version of a DDE preparation, it is possible to keep diffusion times short. Therefore, reducing the effect of restriction in the diffusion-weighted signal. Then, molecular exchange takes place during the z-storage period (or mixing time), where the spins experience only T_1 relaxation. This results in reduced signal attenuation due to T_2 relaxation. In the literature, there are two variants of DDE stimulated echo. The first one, introduced by Callaghan and Furó [110], consists in two pairs of collinear diffusion gradient pulses separated by a mixing time. The mixing time takes place during the z-storage between the second and third 90° RF pulses, and the diffusion gradient pulses are separated by an 180° RF pulse. This pulse sequence was also used by Åslund et al. [40] in NMR spectroscopy (FEXSY) and in its imaging version (FEXI) with clinical applications by Lasič et al. [32, 43], Nilsson et al. [42], Lampinen et al. [45] and Bai et al. [156]. The Bai et al. [156] investigated the feasibility of FEXI to evaluate exchange processes in the human brain by varying the strength of the first pair of diffusion gradients (also called filter block). By using low b-values in the filter block they showed that there is a high correlation between the strength of the diffusion filter and the intravoxel incoherent motion, which is related to blood perfusion. This gives the possibility to map exchange between vascular and extracellular water by using low b-values, while higher b-values are used to map molecular exchange between two water reservoirs. The second variant consists in a stimulated echo preparation with three 90°

RF pulses, also called double bipolar stimulated echo sequence [46]. In this sequence, the diffusion gradient pairs are not separated by an 180°; therefore, the polarity of the gradient pulses are inverted. The mixing time takes place during the z-storage, between the second and third RF pulses. Even though this pulse sequence is easier to implement than the first version, it has been used only in a MR spectrometer, and it is not used in clinical systems.

Other variant of DDE preparations include bipolar diffusion gradients [127, 120, 119, 120, 155, 136]. Such implementations are usually STE-based preparations, where 180° pulses divide each diffusion gradient pulse. The aim of the bipolar-DDE implementations is for microstructure characterization in samples affected by strong internal magnetic fields, generating severe magnetic field inhomogeneities. Bipolar gradients can effectively suppress the effects of background gradients [157]. However, these versions are used in applications in NMR spectrometers and are out of the scope of this work.

3

Pulse sequence implementation

3.1 Introduction

DDE MR sequences consist in the application of two diffusion-weighted periods between excitation and acquisition. In the literature, it is possible to find different magnetization preparations that contain two (or more) diffusion encodings such as spin echo, stimulated echo, and mixed bipolar implementations, as described in section 2.4.2.4. However, the implementation of such pulse sequences is not a simple task. Given that the RF field is not homogeneous over the sample, every additional RF pulse introduces unwanted signal pathways that may affect the echo of interest [158]. To counteract this problem, spoiler gradients are often employed.

In this thesis, two kinds of experiments were performed. The first one is the study of the extracellular contribution to the size estimates in corticospinal tract (CST) using a DDE-SE sequence, as illustrated in Fig. 3.1. In this experiment, an in-house implemented sequence was used, which included two pairs of diffusion gradient pulses and two refocusing pulses, as in Koch and Finsterbusch [29] in humans *in vivo*.

The second experiment studies how the results from FEXI/AXR experiments are influenced by the size of the compartments (restriction effect) present in the sample. Apparent exchange rate experiments require several measurements with increasing mixing

time. For that reason, a stimulated echo version of double diffusion encoding (DDE) was implemented. The DDE-STE preparation implemented here consists of a stimulated echo sequence with two refocusing pulses. The first of these refocusing pulses is located between the first and the second 90° pulse, and the second one is between the third 90° pulse and the image readout, as illustrated in Fig. 3.3. The diffusion gradient pulses are applied before and after the refocusing pulses. This pulse sequence has been used in previous DDE research regarding molecular exchange in yeast suspensions and in humans *in vivo* [32, 42, 43]. All the DDE experiments were approved by the University of Lübeck ethics committee.

Additionally, the background gradients (BGG) cross-terms are studied. This is because BGG are known to influence the quantification of the diffusion process[159]. As the influence of BGG is different for the diffusion gradients that have different polarities [160], they could affect the DDE results that use rotating gradients. Therefore, here is presented a systematic analysis of BGG in the DDE pulse sequences used during *in vivo*in MR measurements in clinical settings.

3.2 MR system and pulse programming environment

All experiments were performed on a whole-body 3 T MR system (Ingenia, Philips, Amsterdam), using an 8-channel head coil array (receive only). The system provides a maximum gradient strength of 45 $mT\,m^{-1}$ with a maximum slew rate of 120 $mT\,m^{-1}\,ms^{-1}$. The sequences were implemented for a Philips Ingenia 3 T system with release 5.1.8 using the Paradise sequence development tool, which runs in a virtual machine with Microsoft Windows 7. Philips Paradise development tool uses its own object-oriented language, called GOAL-C, which defines MR experimental parameters as objects, providing a relatively easy way to manage the elements of a MR pulse sequence.

3.3 Double diffusion encoding spin-echo

For the experiments presented in Chapter 4, an in-house implementation of a double diffusion encoding spin-echo DDE-SE preparation with a single-shot EPI read-out was used. Diffusion-weighted imaging is sensitive to motion at micro- and macroscopic level. The macroscopic motion, e.g. head movement, adds phase shifts to the microscopic motion due to diffusion, generating motion artifacts. In order to avoid this issue, one solution is to use imaging read-outs less susceptible to motion artifacts, such as echo-

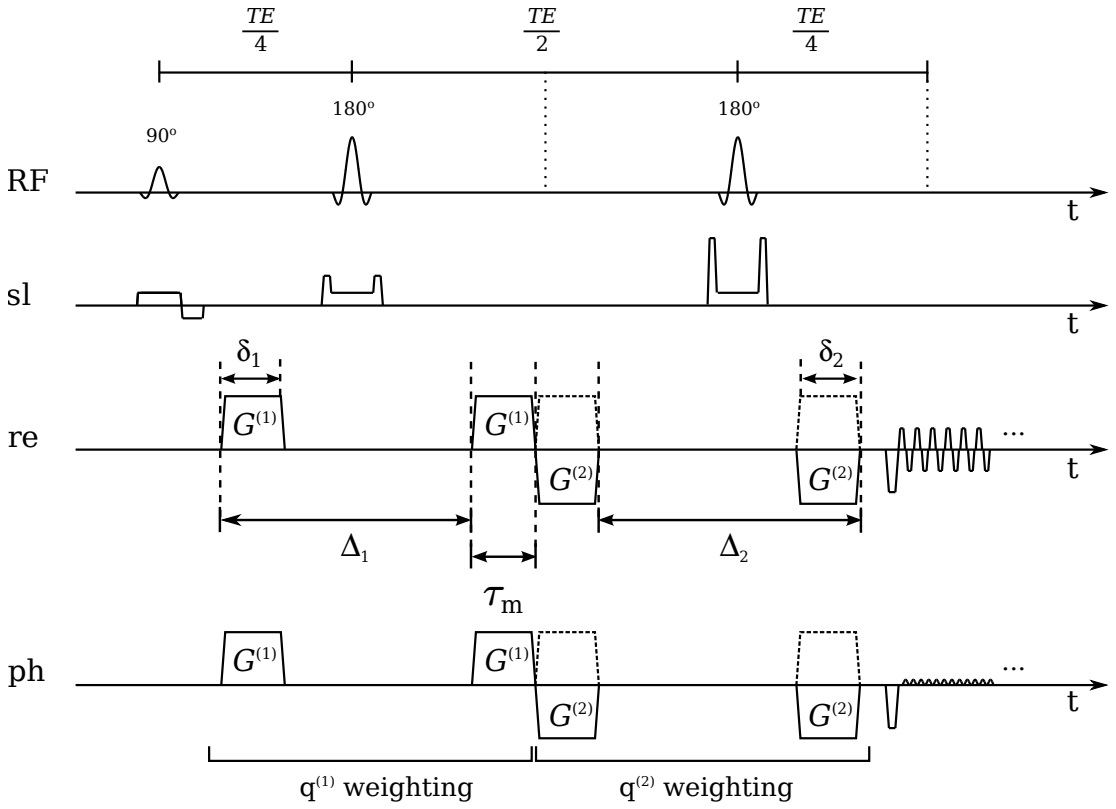

Figure 3.1: DDE-SE sequence with echo planar imaging (EPI) readout (sl: slice-selection, re: read-out, ph: phase-encoding). Dotted lines in the RF time-line show the occurrence of echoes. Crusher gradient pulses are shown in the slice-selection time-line, located before and after the refocusing pulses to suppress unwanted coherence pathways. Crusher gradients have the same duration and their amplitudes differ by a factor of two. Diffusion gradients are applied along the readout and phase-encoding directions. Diffusion gradients drawn with solid line correspond to an experiment with $\psi = 0$. Diffusion gradients drawn with dashed lines correspond to $\psi = \pi$. Amplitude and duration of the pulses are for schematic purposes only.

planar imaging (EPI). EPI is a fast imaging method, and also the most commonly used read-out in diffusion-weighted MRI [161]. With the use of this technique, it is possible to acquire a diffusion-weighted image in approximately 100 ms [162]. However, DDE pulse sequences have relatively long echo times, due to the additional pulses. Therefore, motion correction is advisable.

As shown in Figure 3.1, the implemented DDE-SE pulse sequence consists of one excitation pulse and two refocusing pulses. The first pair of diffusion gradient pulses are positioned before and after the first refocusing, while the second pair is located before and after the second refocusing pulse. The second and third diffusion gradient pulses (in between the first and second refocusing pulses) do not overlap. All RF pulses were slice-selective. Crusher gradient pulses were applied to dephase unwanted FIDs that arose

from non-ideal refocusing pulses, and to select a specific magnetization coherence pathway. All crusher gradient pulse pairs had the same duration and were applied along the slice-selection axis, before and after the 180° pulses.

In this experiment, the echo of interest was the secondary echo of a three-pulse sequence, which is shown in Fig. 3.1. In order to select that specific pathway (see Fig. 3.2), the amplitude of crushers around the second refocusing pulse was twice that of the crushers around the first one.

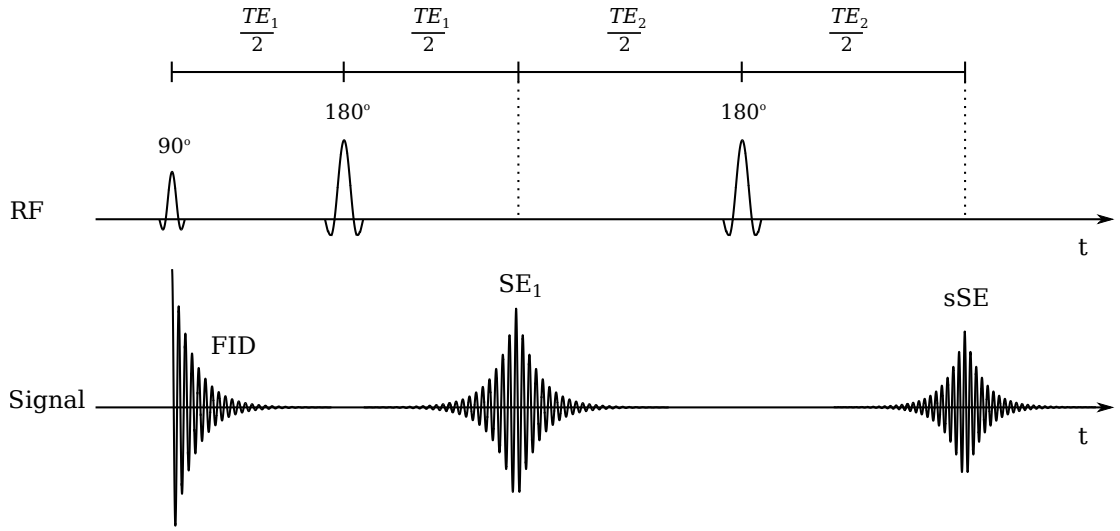

Figure 3.2: The DDE-SE MR signal arises from the effect of the first spin-echo (SE_1) and the second refocusing pulse. For the experiments presented here $TE_1 = TE_2$

3.4 Double diffusion encoding stimulated-echo

An in-house implementation of a double diffusion encoding stimulated-echo (DDE-STE) magnetization preparation, with an EPI read-out was used, as shown in Figure 3.3. Dotted lines in the RF timeline show the occurrence of echoes. All 90° and 180° pulses were slice-selective. Crusher gradients pairs were positioned immediately before and after the refocusing pulses, and before the second 90° and after the third 90° pulse. Each pair of crusher gradients was always applied perpendicular to the diffusion gradients, and their amplitude was set as twice that of the previous pair. A spoiler gradient was applied during the TM-period, as seen in Figure 3.3. This spoiler eliminates the transversal component of the magnetization during z-storage. Then, the echo of interest is the SE formed from the STE of the first SE generated by the excitation pulse and the first refocusing pulse, as

seen in Figure 3.4.

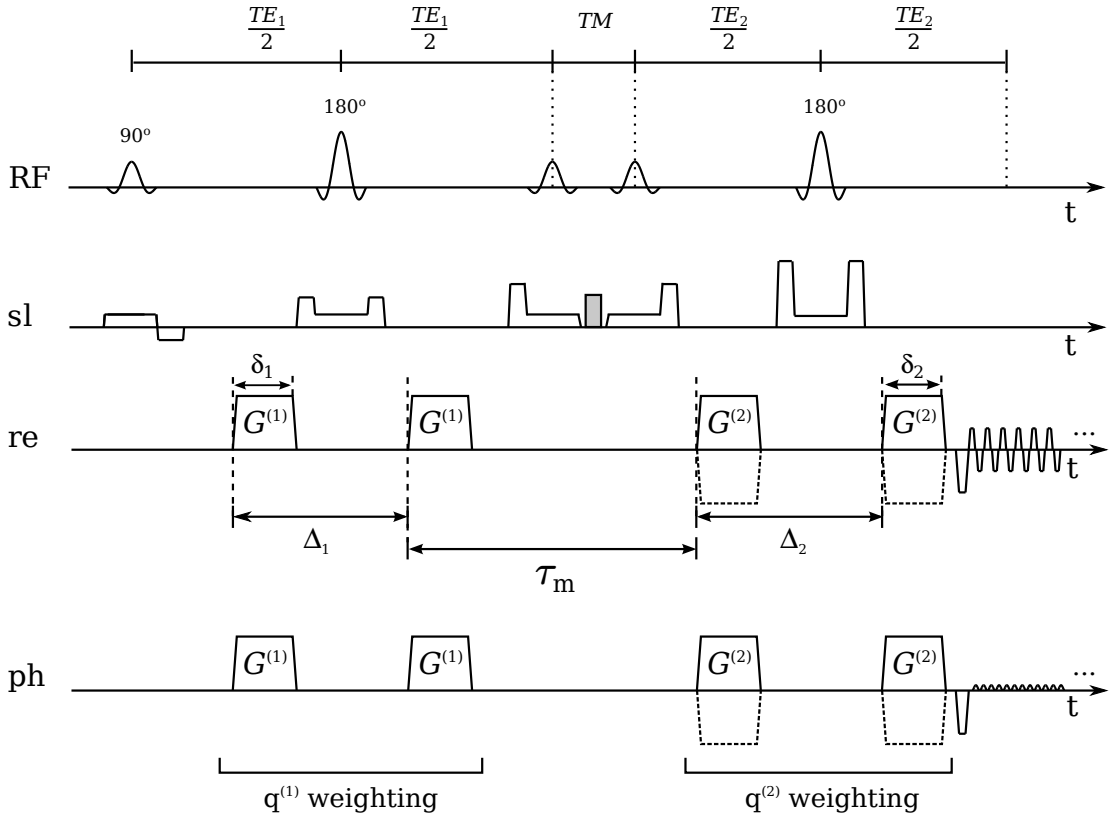

Figure 3.3: DDE-STE sequence with EPI readout (sl: slice-selection, re: read-out, ph: phase-encoding). Crusher gradients are shown in the sl time-line, together with the "homospoil" gradient pulse during the TM period (in gray). Crusher gradients have the same duration for all RF pulses. Their amplitudes differ by a factor of two, applied always perpendicular to the diffusion gradients. Diffusion gradients drawn with solid line correspond to an experiment with $\psi = 0$. Diffusion gradients drawn with dashed lines correspond to $\psi = \pi$. Amplitude and duration of the pulses are for schematic purposes only.

3.5 Rotation of diffusion gradients

As explained in Chapter 2, one of the advantages of DDE is the various degrees of freedom, which are not available for single diffusion encoding (SDE) sequences. The rotation of the diffusion gradients is implemented by means of the Rodrigues' rotation formula [163]. This is used to compute the rotation matrix $\mathbf{R}_a(\psi)$ that corresponds to a rotation by an angle ψ about a fixed axis specified by $\mathbf{a} = (\mathrm{a}_x, \mathrm{a}_y, \mathrm{a}_z) \in \mathbb{R}^3$. Then $\mathbf{R}_a(\psi)$ is given by

$$\mathbf{R}_a(\psi) = \mathbf{I} + \tilde{\mathbf{a}} \sin\psi + \tilde{\mathbf{a}}^2(1 - \cos\psi), \tag{3.1}$$

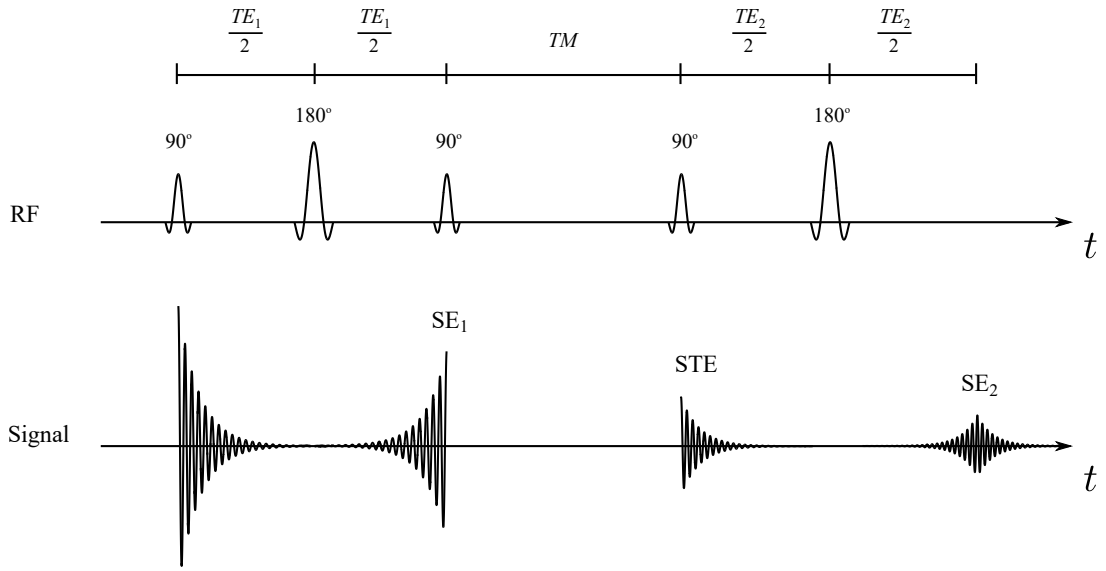

Figure 3.4: The DDE-STE MR signal arises (SE_2) from the effect the first spin echo (SE_1) and its stimulated echo (STE)

where $\mathbf{I}$ is the 3×3 identity matrix and $\tilde{\mathbf{a}}$ corresponds to

$$\tilde{\mathbf{a}} = \begin{bmatrix} 0 & -a_z & a_y \\ a_z & 0 & -a_x \\ -a_y & a_x & 0 \end{bmatrix}. \tag{3.2}$$

For the experiments performed here, the z-axis was the rotation axis for the diffusion gradients. The diffusion gradients are applied in the x-y plane. However, this could be changed as needed. The angle between $\mathbf{G}^{(1)}$ and $\mathbf{G}^{(2)}$ is referred as ψ. To begin the experiments, $\mathbf{G}^{(1)}$ is fixed in an angle ϕ while $\mathbf{G}^{(2)}$ rotates about the z-axis in ψ steps. The angle ϕ determines the direction of $\mathbf{G}^{(1)}$. This angle is chosen for some arbitrary orientation of the diffusion gradients with respect to the sample.

3.6 Background gradient calculations

Ever since the early development of diffusion-weighted MR it has been identified that the contribution of all magnetic field gradients in a pulse sequence influence the quantification of diffusion and, thus, should be taken into account [164]. Background gradients, also called static of internal magnetic gradients, arise from magnetic susceptibility of heterogeneous samples and magnetic field inhomogeneities [165]. This may introduce

additional diffusion-weighting and, if not taken into account, would lead to a systematic error in ADC estimations [166, 167].

Let us consider an SDE pulse sequence as described in Chapter 2: spin-echo preparation with two RF pulses and two gradient pulses positioned before and after the refocusing pulse. Under ideal conditions, i.e. identical rectangular diffusion gradient pulses, the only magnetic field gradients are those from the diffusion-weighting. While the sample has uniform temperature and its relaxation times do not interfere with the choice of Δ, the signal attenuation due to diffusion is $E(b) = e^{(-b\,ADC)}$. However, it is clear that these conditions are not met in experiments. In a realistic sense, the static magnetic field is not perfect, and heterogeneous samples, such as biological tissue, are subject to differences in their magnetic susceptibility, and consequently, to background gradients. For example, a significant difference in magnetic susceptibility in red blood cells, between intra- and extracellular space, has been found [168]. Furthermore, samples containing metal parts are also subject to differences in magnetic susceptibility [169]. Also, the presence of air bubbles in apples can produce large background gradients [167]. The same effect appears in air-tissue boundaries of the human brain, such as the paranasal sinuses area [125].

Considering the effect of an uniform background gradient, $\mathbf{g}_o$ of strength g_o in a Stejskal and Tanner pulse sequence with applied diffusion gradients $\mathbf{g}_a$, under the assumption that $\mathbf{g}_o$ and $\mathbf{g}_a$ are parallel ($\mathbf{g}_a \cdot \mathbf{g}_o = g_a g_o$), then [3, 165]

$$\ln\left[\frac{S^{t=acq}}{S^{t=0}}\right] = -D\gamma^2\left[g_a^2\delta^2\Big(\Delta - \frac{\delta}{3}\Big) + \Big(\frac{2}{3}\tau^3 g_o^2\Big) + \delta g_a g_o\Big(2\tau^2 - t_1^2 - t_2^2 - \delta(t_1 + t_2) - \frac{2}{3}\delta^2\Big)\right], \tag{3.3}$$

where $S^{t=acq}$ corresponds to the measured signal at ($2\tau = TE$), $S^{t=0}$ is the signal directly after the excitation pulse, and g_a is the magnitude of the applied diffusion gradients. In Eq. (3.3), it can be seen that the measured signal has contributions from all the magnetic field gradients, where the first term corresponds to the ideal diffusion weighting. The second term, as τ is constant, can be neglected. Still, if the background gradient is too large ($g_a\delta \gg g_o\tau$ does not hold), the g_o term can produce additional signal attenuation, reducing the SNR. The third term's situation is more complex than the g_a and g_o terms. The $g_a g_o$ term is called background gradient "cross-term", and it is usually not constant. The problem with the cross-term arises since it can introduce additional signal attenuation depending on the sequence timing parameters, such as δ, Δ, TE and the position in time of the diffusion gradient pulses. Additionally, the $g_a g_o$ term can introduce non-linearity in the relationship between the signal attenuation and the b-values, making the following signal analysis complicated [170, 160]. Furthermore, due to the cross-term, the measured diffusion-weighted signal can appear as anisotropic when it is not the case [171, 155].

In applications including DDE measurements, the effect of BGG has been a topic of interest. In DDE measurements, in which the diffusion gradients rotate, it can be expected that the effect of experimental imperfections will depend on the angle between the gradient pulses [121]. Koch and Finsterbusch [107] employed a DDE sequence with six π-pulses where, in order to suppress cross-terms, the time integral of the background gradient needs to be antisymmetric within each diffusion-weighted period. Later, Shemesh and Cohen [155] experimentally investigated the effects of BGG in SDE and DDE. They showed that the DDE signal modulation at short τ_{m} could be inverted in the presence of background gradients, masking the effects of restriction and microscopic anisotropy. They called this effect "apparent-Susceptibility-Induced-Anisotropy" (aSIA). In order to reduce the effect of the background gradients, they introduced bipolar diffusion gradients where each diffusion gradient pulse is divided by a π-pulse inverting the polarity of the second half. This approach has been extensively used in NMR spectroscopic, especially in samples with strong magnetic susceptibilities [127, 119, 120, 136, 116, 142, 172, 173, 138, 174, 175, 176].

In applications in clinical scanners, Lawrenz and Finsterbusch [121, 123, 125] reduced the effects of eddy currents and BGG by simply taking the geometric average of signal acquisitions performed with diffusion-weighted gradients with opposite polarities, as described by Neeman et al. [166]. However, a new magnetization preparation to compensate for cross-terms has been recently introduced by Lawrenz and Finsterbusch [177]. This pulse sequence includes inversion recovery and four additional π-pulses, and has shown better results than the use of the geometric average.

In the present thesis, an analysis of background gradient cross-terms in the most commonly used DDE sequence *in vivo* is presented. This analysis was performed following the procedure proposed by Zheng and Price [157], which considers a constant BGG. Then, the echo attenuation due to diffusion (without considering relaxation processes) can be calculated as [3]

$$\ln\left[\frac{S^{t=acq}}{S^{t=0}}\right] = -D\gamma^2 \int_0^t \left(\int_0^{t''} (-1)^{\mathrm{m}} g_{\mathrm{eff}}(t')dt' \right)^2 dt'', \tag{3.4}$$

where $S^{t=acq}$ corresponds to the measured signal and $S^{t=0}$ to the signal immediately after the first excitation pulse; D is the self-diffusion coefficient and γ is the gyromagnetic ratio. The effective gradient, $g_{\mathrm{eff}} = (-1)^{\mathrm{n}} \cdot g$, is the sum of all gradients present in the sequence time interval under study, where n is the number of π pulses applied after the gradient. In this manner, after every π pulse, the sign of the gradients is inverted. In a STE-based sequence, $\mathrm{m} = 1$ during the decoding interval (second diffusion-weighted period), otherwise $\mathrm{m} = 0$. This ensures that the gradients change sign during the decod-

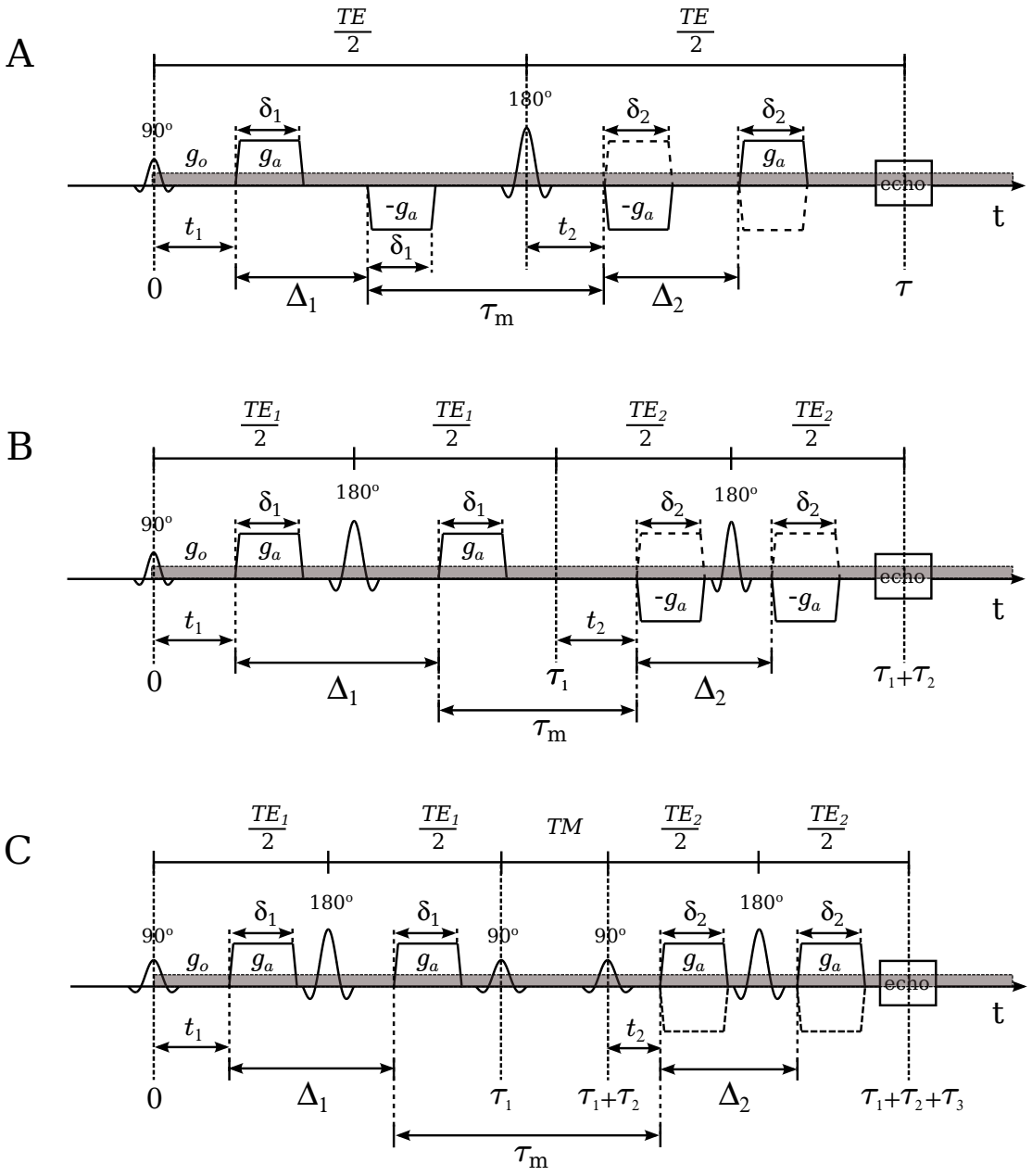

Figure 3.5: DDE MR sequences commonly used in *in vivo* measurements. **A)** Spin-echo DDE sequence, mainly used for microscopic anisotropy studies [123, 125, 124, 129]. **B)** Double spin-echo DDE sequence [178, 29, 125], used for compartment size estimations and microscopic anisotropy. **C)** Stimulated echo based DDE sequence, mainly used for membrane permeability estimations in FEXI experiments [32, 42, 43].

ing period. $g_{\text{eff}} = 0$ during the z-storage. In the calculations presented here (within the time interval as depicted in Fig. 3.5), g_a and g_o are the applied diffusion gradients and background gradients, respectively. g_o, with amplitude g_o, is considered to be constant

in time and space, and the applied diffusion gradients for the first and second diffusion encoding have equal amplitude, g_a, and duration, δ. Figure 3.5 A shows a spin-echo sequence with two pairs of diffusion gradient pulses separated by a single π pulse. This kind of sequence has been extensively used for *in vivo* microscopic anisotropy estimations [123, 125, 124, 129]. The diffusion signal attenuation has been calculated using Eq. (3.4) for $\psi = 0$ and $\psi = \pi$, resulting in

$$\ln\left[\frac{S^{t=acq}}{S^{t=0}}\right]_{\mathrm{A}}\Bigg|_{\psi=0} = -D\gamma^2\left[\frac{2}{3}\delta^2 g_a^2\Big(3\Delta-\delta\Big) + \frac{g_o^2}{12}\tau^3 + \Delta\delta g_a g_o\Big(2t_1 - 2t_2 + \tau\Big)\right] \tag{3.5}$$

and

$$\begin{aligned}\ln\left[\frac{S^{t=acq}}{S^{t=0}}\right]_{\mathrm{A}}\Bigg|_{\psi=\pi} = -D\gamma^2\Bigg[&\frac{2}{3}\delta^2 g_a^2\Big(3\Delta-\delta\Big) + \frac{g_o^2}{12}\tau^3 \\ &+ \Delta\delta g_a g_o\Big(2\Delta + 2\delta + 2t_1 + 2t_2 - \tau\Big)\Bigg],\end{aligned} \tag{3.6}$$

respectively. In Eq. (3.5), when $\psi = 0$, it can be observed that if $t_1 = t_2$ and the diffusion gradients are placed symmetrically before and after the refocusing pulse, then the cross-term depends solely on τ, which corresponds to the echo time. However, for $\psi = \pi$ with the symmetry described before, the cross-term from Eq. (3.6) cancels-out. Hence, it is shown that in the presence of timing symmetry, the cross-term depends on the angle between the diffusion wave-vectors, where $\psi = \pi$ suppresses the cross-term. Additionally, it is important to note that a DDE sequence with parallel diffusion gradients is flow-compensated and used for estimation of the intravoxel incoherent motion (IVIM) [179].

Figure 3.5 B[1] [180] shows a DDE sequence with two refocusing pulses, one in the center of each diffusion weighting, which reduces the background gradient cross-term [125]. For this sequence, the diffusion signal attenuation was calculated for $\psi = 0$ and $\psi = \pi$, resulting in

$$\begin{aligned}\ln\left[\frac{S^{t=acq}}{S^{t=0}}\right]_{\mathrm{B}}\Bigg|_{\psi=0} = -D\gamma^2\Bigg[&\delta^2 g_a^2\frac{2}{3}\Big(3\Delta-\delta\Big) + \frac{g_o^2}{12}\Big(\tau_1^3 + \tau_2^3\Big) \\ &- \delta g_a g_o\Big(2\Delta(t_1 - t_2 - \tau_1 + \tau_2) + \delta(2t_1 - 2t_2 - \tau_1 + \tau_2) \\ &- 2t_1(\tau_1 - t_1) + 2t_2(\tau_2 - t_2) + \frac{\tau_1^2}{2} - \frac{\tau_2^2}{2}\Big)\Bigg]\end{aligned} \tag{3.7}$$

[1] Bachelor thesis Luise Preuße, 2016

and

$$\ln\left[\frac{S^{t=acq}}{S^{t=0}}\right]_{\mathrm{B}}\Bigg|_{\psi=\pi} = -D\gamma^2\Bigg[\delta^2 g_a^2\frac{2}{3}\Big(3\Delta-\delta\Big)+\frac{g_o^2}{12}\Big(\tau_1^3+\tau_2^3\Big) - \delta g_a g_o\Big(2\Delta(\Delta+\delta+t_1+t_2-\tau_1-\tau_2) + \delta(\frac{4}{3}\delta+2t_1+2t_2-\tau_1-\tau_2)+2t_1(t_1-\tau_1)+2t_2(t_2-\tau_2) + \frac{\tau_1^2}{2}+\frac{\tau_2^2}{2}\Big)\Bigg], \tag{3.8}$$

respectively. In Eq. (3.7) it can be observed that if $t_1 = t_2$ and $\tau_1 = \tau_2$, then the cross-term is nullified. However, this does not occur if $\psi = \pi$ in Eq. (3.8). In this pulse sequence, the cross-terms depend on the direction of the diffusion gradients, just as for the sequence shown in Fig. 3.5 A. However, if Δ is relatively short, the cross-term is reduced, and could be neglected. Nonetheless, if long Δ is required, such as in the study of large compartment sizes, it is better to use a pulse sequence that completely suppresses the cross-term. The DDE sequence used by Koch and Finsterbusch [107] with two refocusing pulses per diffusion weighting is background gradient cross-term compensated, independent of timing parameters, which makes it a more appropriate option to perform measurements where long Δ is required.

Figure 3.5 C shows a stimulated version of DDE, commonly used for experiments that require long mixing time. Estimation of membrane permeability in terms of apparent exchange rate uses this kind of sequence because it makes possible to increment τ_{m} without losing signal due to T_2 relaxation. For the background gradient cross-term analysis, Δ_1 and Δ_2, and δ_1 and δ_2 are not necessarily equal. If parallel diffusion gradients are used, the natural logarithm of the diffusion signal attenuation is given by

$$\ln\left[\frac{S^{t=acq}}{S^{t=0}}\right]_{\mathrm{C}}\Bigg|_{\psi=0} = -D\gamma^2\Bigg[\frac{g_a^2}{3}\Big(\delta_1^2(3\Delta_1-\delta_1)+\delta_2^2(3\Delta_2-\delta_2)\Big)+\frac{g_o^2}{12}\Big(\tau_1^3+\tau_3^3\Big) - g_a g_o\Big(\Delta_1\delta_1(\Delta_1+\delta_1+2t_1-2\tau_1)+\Delta_2\delta_2(\Delta_2+\delta_2+2t_2-2\tau_3) + \delta_1^2(\frac{2}{3}\delta_1+2t_1-\tau_1)+\frac{\delta_1}{2}(2t_1-\tau_1)^2+\delta_2^2(\frac{2}{3}\delta_2+2t_2-\tau_3)+\frac{\delta_2}{2}(2t_2-\tau_3)^2\Big)\Bigg]. \tag{3.9}$$

On the other hand, when antiparallel diffusion gradients are used, then

$$\ln\left[\frac{S^{t=acq}}{S^{t=0}}\right]_{\mathrm{C}}\Bigg|_{\psi=\pi} = -D\gamma^2\Bigg[\frac{g_a^2}{3}\Big(\delta_1^2(3\Delta_1-\delta_1)+\delta_2^2(3\Delta_2-\delta_2)\Big)+\frac{g_o^2}{12}\Big(\tau_1^3+\tau_3^3\Big) - g_a g_o\Big(\Delta_1\delta_1(\Delta_1+\delta_1+2t_1-2\tau_1)-\Delta_2\delta_2(\Delta_2+\delta_2+2t_2-2\tau_3) +(\delta_1^2(\frac{2}{3}\delta_1+2t_1-\tau_1))+(\frac{\delta_1}{2}(2t_1-\tau_1)^2)-(\delta_2^2(\frac{2}{3}\delta_2+2t_2-\tau_3)) -(\frac{\delta_2}{2}(2t_2-\tau_3)^2)\Big)\Bigg], \tag{3.10}$$

where if $\delta_1 = \delta_2$, $\Delta_1 = \Delta_2$, $t_1 = t_2$ and $\tau_1 = \tau_3$, the $g_a g_o$ term is zero. Therefore, if timing symmetries occurred, one gradient orientation is cross-term compensated ($\psi = \pi$), but parallel wave-vectors will not be.

In the first pulse sequence implemented in this thesis, shown in Fig. 3.1 and Fig. 3.5 B, $\tau_1 = \tau_2$, but $t_1 \neq t_2$. Therefore, the cross-term is not compensated. In order to keep the duration of the pulse sequence as short as possible, and to a minimum τ_{m}, the last diffusion-weighted pulse is placed immediately after the last refocusing pulse. However, as the size of compartments studied *in vivo* is small, then the Δ value required is relatively short. Therefore, the effects of the cross-terms are expected to be negligible [29].

In the second implementation, shown in Fig. 3.3 and Fig. 3.5 C, $t_1 \neq t_2$, $\Delta_1 \neq \Delta_2$, and $TE_1 \neq TE_2$, the first diffusion gradient pulses are situated symmetrically before and after the pi-pulse, keeping TE_1 short. However, in order to keep TE_2 and Δ_2 short, the second diffusion-weighting is also placed immediately after the last π-pulse.

In summary, it is difficult to apply the above-described symmetries in experimental measurements. In order to satisfy the important timing requirements for an application, such as long or short τ_{m}, long or short Δ and ideally keeping the echo times short, compromises need to be made.

4

Extracellular contribution to DDE pore size estimates in the corticospinal tract

4.1 Introduction

Diffusion-weighted magnetic resonance imaging has evolved into a widely used tool for studying tissue microstructure [181, 182, 183, 184, 185]. In diffusion-weighted imaging, the magnetization preparation is most often based on the pulsed gradient spin echo [3]. However, modifications of this approach have been proposed in order to increase the sensitivity of the diffusion-weighted signal to various aspects of tissue microstructure. Recently, double diffusion encoding (DDE) [70] has been introduced as an extension of the conventional Stejskal-Tanner diffusion-weighted MRI [3] in which two (instead of one) pairs of diffusion-sensitized gradients are applied between excitation and signal acquisition in a sequence [27, 186, 28]. This set-up provides two additional degrees of freedom: it is possible to 1) vary the angle between the two diffusion-weighted periods (ψ), and 2) the time between them (also called mixing-time τ_m). These new parameters make possible to study microscopic characteristics that are not easily available using other non-invasive methods.

DDE experiments can be sensitive to different aspects of tissue microstructure [28], such

as microscopic anisotropy [112, 152], perfusion fraction [187], compartment size [117], and water exchange [40, 32]. However, it is difficult to design an experiment that is specific to an individual effect out of these.

Previous experiments estimated the size of compartments (e.g., cells) using the signal difference between parallel and antiparallel diffusion gradients in water-filled spaces around polymethyl methacrylate beads, radish root, and porcine spinal cord fixed in formalin [107, 188], hollow microcapillaries [130, 151, 135] (using spectrometer), rat spinal cord fixed in paraformaldehyde [137], cells of plants [189], yeast cells [136], and in humans *in vivo* [29, 123, 122].

Early applications of DDE weighting for an assessment of compartment size *in vivo* seemed to result in relatively large diameters [29]. Besides, preliminary work on patients with stroke-induced Wallerian degeneration of neurons in the cortical spinal tract revealed a reduced signal difference between parallel and antiparallel gradient orientations in the affected tract [190]. These *in vivo* results on human brain tissue raised the question to which degree the extracellular space contributes to the compartment size estimates gained by evaluating the DDE signal. On the other hand, it has been suggested that the signal difference between parallel and perpendicular gradient orientations may gather further information about pore shape when using long mixing times [27, 117, 191, 113, 120]. This approach was used recently to detect microscopic anisotropy in tissue which macroscopically appears isotropic in conventional (i.e., single diffusion encoding) diffusion-weighted measurements [121, 119, 123, 115]. Clinical applications of this approach were also investigated [129].

Considering DDE experiments on a sample comprising eccentric but randomly oriented water-filled pores, Mitra [28] distinguished between two effects. The "filter effect" leads to an attenuation difference between parallel and perpendicular gradient orientations. This is exploited in studies assessing microscopic anisotropy, independent of the mixing time. In contrast, the difference between parallel and antiparallel gradient orientations, which is exploited in attempts determining the pore or cell size, depends on τ_{m} being short. It should be noted that SDE and DDE experiments in principle yield equivalent information at low gradient amplitude, i.e. when only terms up to second order in the time integral of a single gradient pulse are considered [114].

In this work, the DDE unique sensitivity to pore shape is used to acquire information on the relative contribution of the extracellular space to the size estimates from DDE in applications to brain white matter *in vivo*. Additionally, left-right CST asymmetries are investigated using DDE.

4.2 Theory

In principle, DDE measurements in the long τ_m regime can be used to detect whether water in a sample is confined to spherical or eccentric compartments [27]. At long τ_m, water-filled spheres yield the same DDE signal for parallel and perpendicular gradient orientations. In contrast, eccentric pore shapes, such as ellipsoids, exhibit different signal amplitude in cases of parallel and perpendicular gradient orientations, even if the pores are randomly oriented [28]. The cases of water-filled spheres, parallel, tilted, and randomly oriented water-filled cylinders can be seen in Fig. 4.1, where the angular signal dependency of DDE signal is plotted for different structural environments at long τ_{m}. For spheres (Fig. 4.1 A), as isotropic compartments, the orientation of the diffusion gradient is not important. However, for cylinders, it is relevant to show the orientation of the plane spanned by the diffusion gradient with respect to the orientation of the cylinders. This is because the cross-section in the plane of the applied diffusion gradients influences the angular dependency at long τ_{m}, as shown in Figs. 4.1 B, C and D.

In coherent brain white matter, one would apply diffusion gradients in a plane perpendicular to the axonal axis. For our purposes, the white matter can be seen as a bundle of densely packed, infinitely long cylinders with circular base, as illustrated in Fig. 4.2 A. A perpendicular cross-section through such a bundle of same-size cylinders consists of circles (see Fig. 4.2 B), where as the compartments between these circles resemble equilateral triangles. This shape is sometimes called circular horn triangle. They possess a 3-fold symmetry axis (see Figs. 4.2 A and B). However, it is expected that a pore with a cross-section shaped like a circular horn triangle will not induce a measurable signal difference between parallel and perpendicular gradient orientations in DDE experiments. The pores cannot easily be distinguished from circular compartments, i.e., pores with C_∞ symmetry. This might be possible, however, using approaches designed to image the mean pore shape directly [192]. Nonetheless, when the cylinders are different in size and not too densely packed, the cross-section contains circular pores, and the space between the cylinders is "irregularly shaped" (Fig. 4.2 C), meaning here that no rotational symmetry exists. If sufficiently large, the deviation from a circle can be detected by DDE experiments comparing the signal for parallel and perpendicular diffusion gradient directions, with the diffusion gradients oriented in a plane perpendicular to the fiber axis. This is expected to work even in case of open pores in the plane spanned by the diffusion gradients [28]. Pores with circular cross-section will not exhibit a parallel–perpendicular signal difference in a DDE experiment (as shown in Fig. 4.1 A and B). Hence, the parallel–perpendicular signal difference might yield information about the shape of the compartment dominating the DDE pore size estimate in the corticospinal tract (CST).

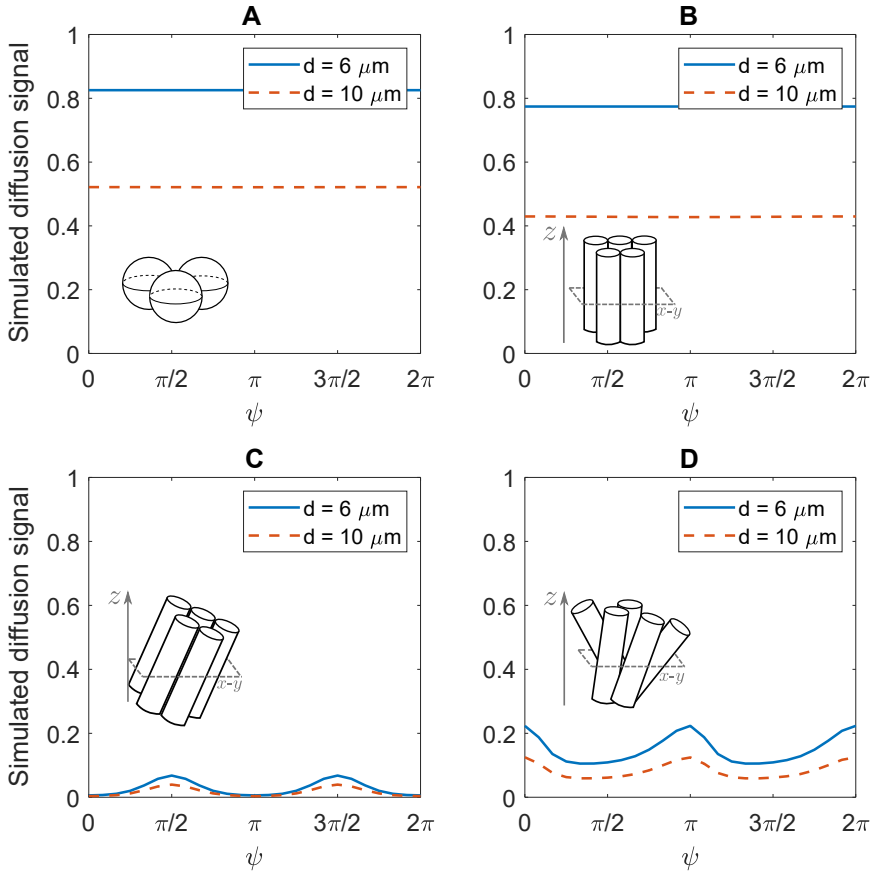

Figure 4.1: Simulated angular signal dependence of DDE sequences with long τ_m for water-filled **A**) spheres, **B**) straight parallel cylinders, **C**) tilted parallel cylinders and **D**) randomly oriented cylinders (average of 50 cylinders). Spheres and cylinders were simulated with diameters of 6 and 10 μm, separately. In sub-figures B, C and D, the grey arrow represents the z-axis of the gradient coordinate system. The diffusion gradients are applied in the x-y plane, showed in grey dashed lines. The simulations were performed using MISST with the following parameters: $\delta = 1$ ms, $\Delta = 100$ ms, $\tau_m = 20$ ms, and $G = 1$ T/m. A strong magnetic field is used in order to clearly observe the angular dependency.

The difference between parallel and perpendicular gradient orientations arises from the following reasoning. Consider a sample or voxel containing two sets of the same number of equally shaped, eccentric pores. The pores in each set may be all aligned along a given direction, the alignment directions of the two sets being perpendicular to each other. The signal attenuation may be written as $E(q,\psi) = S(q,\psi)/S_0$, where S_0 represents the signal with all diffusion gradients set to zero, q is the identical amplitude of both wavevectors, $\mathbf{q}^{(i)} = \gamma\delta\mathbf{G}^{(i)*}/(2\pi)$, $i = 1,2$, where $\mathbf{G}^{(i)*}$ denotes the field gradient vector associated with the first pulse in the effective diffusion-weighting gradient waveform of the i^{th} weighting, and ψ is the angle between the two $\mathbf{q}$ vectors [70]. For parallel ($\|$) and

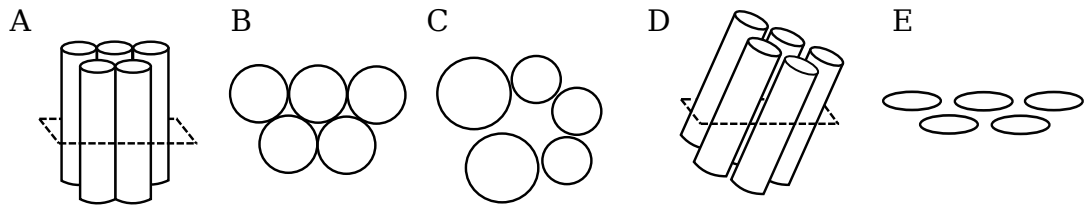

Figure 4.2: **A)** Packed circular cylinders, **B**) cross-section of densely packed cylinders as in A, **C**) possible cross-section with looser packing, **D)** tilted circular cylinders and **E)** cross-section of D (exaggerated) or untilted cylinders with elliptical base. **E)** Also pictures the cross-section of ellipse-based cylinders.

perpendicular ($\perp$) orientations of the diffusion wave vector, the signal attenuations may be expressed employing effective diffusion coefficients,

$$E_{\parallel} = E(q,0) = \frac{1}{2}e^{-bD_1}e^{-bD_1} + \frac{1}{2}e^{-bD_2}e^{-bD_2} \tag{4.1}$$

and

$$E_{\perp} = E(q,\pi/2) = \frac{1}{2}e^{-bD_1}e^{-bD_2} + \frac{1}{2}e^{-bD_2}e^{-bD_1}, \tag{4.2}$$

respectively, which in general are not equal. In these equations, D_1 and D_2 are the effective diffusion coefficients due to restriction along the two perpendicular diffusion gradient directions involved. The degree of diffusion-weighting, $b = \gamma^2 G^2 \delta^2 (\Delta - \delta/3)$ (γ: gyromagnetic ratio, $\mathbf{G} = \|G\| = G$: gradient strength, δ: gradient duration and Δ: temporal separation between diffusion gradients). $E_{\parallel}$ and $E_{\perp}$ are also unequal in samples with randomly oriented eccentric pores. This inequality reflects the physical basis that makes eccentricity estimation in DDE experiments possible [191].

In this work, we are concerned with size estimates which exploit the DDE signal difference between parallel and antiparallel gradient orientations. When applying this approach to a fiber bundle in brain white matter, the complication arises in that the plane spanned by the diffusion gradients may not be perfectly perpendicular to the fibers. In this case, the cross-section of a circular cylinder elliptical (Fig. 4.2 D and E). This eccentric shape also leads to differences between parallel and perpendicular gradient directions in the DDE signal [108], as shown in Fig. 4.1 C. Nevertheless, the difference arising from this situation can be removed by specific averaging of the signal for different gradient vectors. In a scenario where a voxel contains only a single orientation of eccentric 2 D pores, as would be the case depicted in Fig. 4.2 D and E,

$$E_{\parallel} = e^{-bD_1}e^{-bD_1} \neq e^{-bD_1}e^{-bD_2} = E_{\perp} \tag{4.3}$$

can occur. Rotating all gradients by $\pi/2$ will then yield

$$E'_{\parallel} = e^{-bD_2}e^{-bD_2} \neq e^{-bD_2}e^{-bD_1} = E'_{\perp}. \tag{4.4}$$

Calculating the geometric mean of the signals given in Equations (4.3) and (4.4), the signal difference between parallel and perpendicular gradient orientations should vanish, i.e. $(E_{\parallel}E'_{\parallel})^{1/2} = (E_{\perp}E'_{\perp})^{1/2}$.

This reasoning would apply for both, elliptic-based cylinders (tilted or not) and tilted circular cylinders, which generate elliptic pores in the cross-section spanned by the diffusion gradients. However, if the difference does not hold, i.e., if $\bar{E}_{\parallel} \neq \bar{E}_{\perp}$, then it can be inferred that the signal does not arise from parallel circular cylinders. The sample may then rather comprise parallel cylinders with eccentric bases that are not aligned with each other, or circular cylinders with more than one direction of inclination. Considering the homogeneous structure of the CST, different inclinations in a single voxel are unlikely. Hence, it can then be concluded that the space dominating the signal is irregularly shaped (i.e., its cross-section in the plane of the diffusion gradients is not circular). This would point to the extracellular space as the origin of the DDE signal. It should be noted that the rotationally invariant indices proposed for assessing pore shape [152, 115] are not particularly useful in the given situation. This is because it is beyond question that the compartments (probably both intra- and extracellular space) in white matter are not spherical. The question addressed by DDE means is rather whether the cross-section of the compartments (defined by the plane spanned by the diffusion gradients) is circular or eccentric, in order to determine whether the DDE size estimate rather refers to the intra- or extraxonal space. However, the approach used here is based on the idea to average out the influence of macroscopic anisotropy, which is also used in different microscopic anisotropy indices suggested [152, 115].

This simple reasoning must be changed if pores of different shapes are present. This would be the situation in a white matter voxel containing loosely packed axons and the plane of the diffusion gradients is not perpendicular to the axonal fibers, as depicted in Fig. 4.2 D and E. In summary, in a voxel containing two kind of pore shapes (eccentric and non-eccentric), the difference between parallel and perpendicular gradient orientations after the geometric mean of the DDE signal with all diffusion gradients rotated by $\pi/2$ (in the laboratory frame) will persist in two cases: a significant contribution to the DDE signal arising from a non-eccentric pore or due to randomly oriented compartments. In the following, we use a "(g)" superscript to denote the geometric mean, as in

$$\bar{E}_{\parallel}^{(g)} = \sqrt{\bar{E}_{\parallel}\bar{E}'_{\parallel}} \quad \text{and} \quad \bar{E}_{\perp}^{(g)} = \sqrt{\bar{E}_{\perp}\bar{E}'_{\perp}}. \tag{4.5}$$

4.3 Methods

4.3.1 Double diffusion encoding implementation

DDE measurements were performed using a diffusion-weighted double-spin echo magnetization preparation (see Fig. 4.3) with EPI read-out on a whole-body MRI system operating at 3 T magnetic field strength (Ingenia 3.0 T, Philips Healthcare, Best, The Netherlands), using an 8-channel head coil array. SPIR fat suppression [59] was employed. All RF pulses were slice-selective. All crusher gradient pulses had the same duration and were applied in the slice-selection direction, before and after the refocusing RF pulses. The amplitudes of the crusher pulse pairs differ by a factor of two to suppress unwanted coherence pathways. In all DDE experiments, the diffusion gradients were always perpendicular to the slice-select direction (z) to the axial imaging slice, to avoid cross-terms with the slice-selection gradients. Both the angle, ψ, subtended by the two diffusion wave vectors, $\mathbf{q}^{(1)}$ and $\mathbf{q}^{(2)}$, and ϕ, determining the orientation of $\mathbf{G}^{(1)}$ in the laboratory frame, were varied. $\phi = 0$ was chosen to correspond to $G_x^{(1)} = G_y^{(1)}$ and $G_z^{(1)} = 0$.

4.3.2 Simulations

Simulations were performed using the software package MISST v0.93[1] [193, 194, 195] with Matlab2015b (The MathWorks, Natick, Massachusetts, United States) to study the effect of the relative volume fractions of extra- and intracellular compartments on the DDE signal. In MISST, the diffusion-weighted MR signal is simulated using the matrix formalism introduced by Callaghan [196]. The parameter settings were chosen to match the settings in the *in vivo* experiments ($\delta = 10$ ms, $\Delta = 62$ ms, $b = 2 \cdot 812$ s mm^{-2} and $\tau_{\mathrm{m}} = 10.9$ ms).

A two-compartment model was used to represent the white matter structure in the CST, where the total MR signal originates from water inside the axons or in the extracellular space. The intracellular space was modeled as circular cylinders of diameters 1, 5, and 10 μm which are inclined with respect to the z-axis. The inclination angle, α, of the cylinders was obtained from the DTI results (mean of angle modulus over bilateral CST ROI), together with the azimuthal angle, β, of the cylinder axis' projection onto the x-y plane, as depicted in Fig. 4.5 B. The intrinsic diffusivity inside the cylinders was set to the free self-diffusion coefficient [197] of bulk water at 36 °C, $D_0 = 3 \cdot 10^{-9}$ m^2 s^{-1}.

[1] The package can be downloaded from https://www.nitrc.org/projects/misst

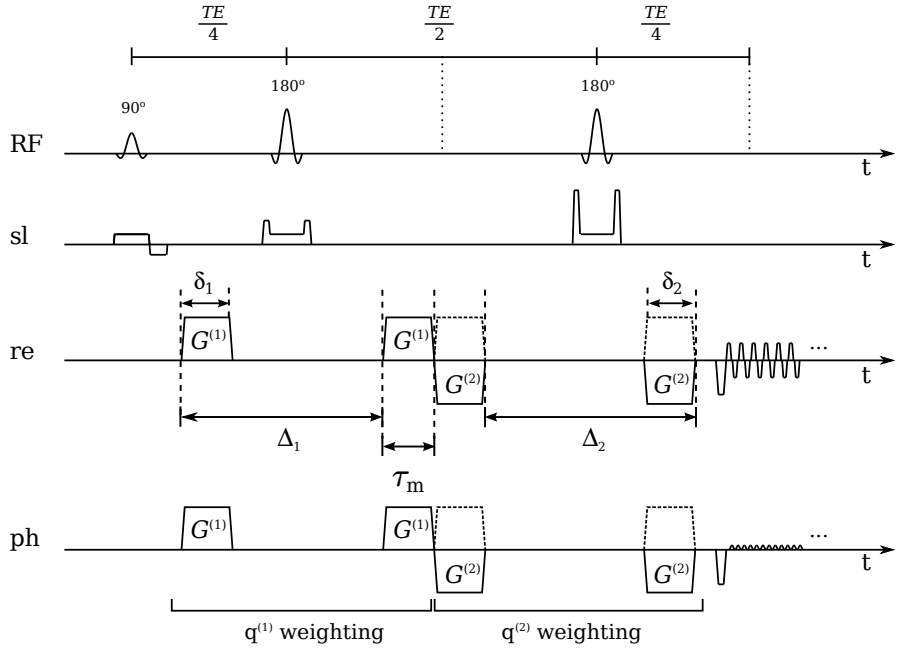

Figure 4.3: DDE imaging sequence with EPI readout (schematic) (sl: slice selection, re: readout, ph: phase encoding). Dotted lines in the RF timeline show the occurrence of echoes. Crusher gradients are shown in the slice selection timeline, located before and after the refocusing pulses to suppress unwanted coherence pathways. Crusher gradients have the same duration and their amplitude differ by a factor of two. Diffusion gradients are applied along with the readout and phase encoding directions. Diffusion gradients drawn with a solid line correspond to an experiment with $\psi = 0$ (i.e., $\mathbf{q}^{(1)} = \mathbf{q}^{(2)}$). Diffusion gradients drawn with dashed lines correspond to the $\psi = \pi$ case. Amplitude and duration of the pulses are not drawn to scale.

Diffusion in the extracellular space was described by an effective diffusion tensor. The diffusion tensor has six degrees of freedom: one parallel and two perpendicular diffusivities and three angles (α, β, and ζ) describing the orientation of the tensor.

The parallel diffusivity (d_{par} – the largest tensor eigenvalue) and perpendicular diffusivities (d_{per1} and d_{per2}) were obtained from the DTI data in the bilateral ROI for volunteer no. 8: $d_{\text{par}} = 1.35 \cdot 10^{-9}$ m^2 s^{-1}, $d_{\text{per1}} = 0.57 \cdot 10^{-9}$ m^2 s^{-1}, and $d_{\text{per2}} = 0.34 \cdot 10^{-9}$ m^2 s^{-1}. The largest-eigenvalue eigenvector of the tensor was aligned with the symmetry axis of the cylindrical intracellular compartment, given by the DTI-derived angles α and β. The simulation requires a third angle, ζ, which describes the rotation of the tensor about its axis. Here, it was set to 0. Simulations were performed with $\phi = 0$ and $\phi = \pi/2$ and the ψ values used *in vivo*. The results for $\phi = 0, \pi/2$ were averaged using a geometric mean. The simulations were run with three intracellular volume fractions, $f_{\text{in}} = 1$, 0.7, 0.5, and 0.3.

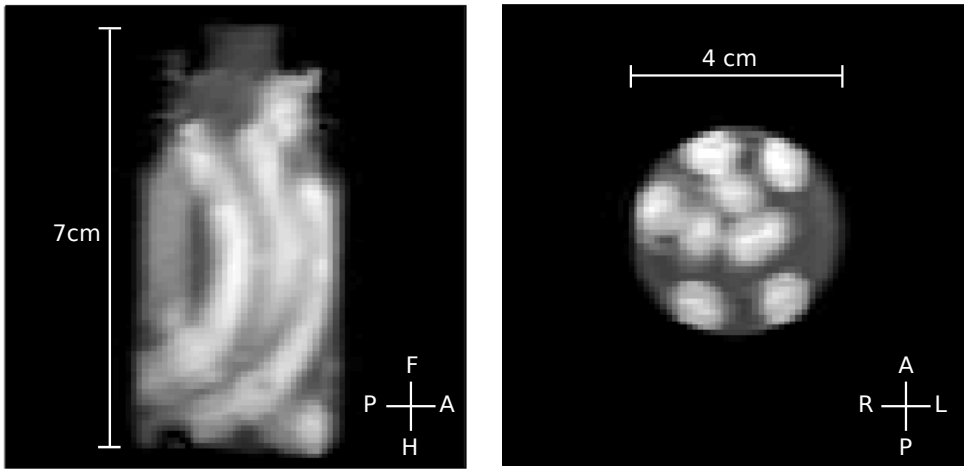

Figure 4.4: T_1-weighted turbo field echo (TFE) MR image of the porcine spinal cord sample fixed in formalin. Left and right images correspond to sagittal and coronal views, respectively.

4.3.3 Spinal cord experiment

A spinal cord sample was obtained from a pig, fixed in formalin and cut into pieces of 4 cm long approximately. The pieces were placed relatively parallel to each other in a 50 ml plastic bottle and submerge in formalin (see Figure 4.4). The DDE experiment was performed placing the bottle with its symmetry axis parallel to the main magnetic field (z-axis). The diffusion gradients were applied perpendicular to the main axis of the bottle in the x-y plane. A total of 32 gradient directions were acquired. ϕ was set to 0, $\pi/2$, π, and $3\pi/2$, while for each of these ϕ values, 8 equally spaced ψ values from 0 to $7\pi/4$ were chosen.

One axial slice of 4 mm thickness was acquired with $TE = 180$ ms, $TR = 6.5$ s. field-of-view (FOV) $= 72 \times 122$ mm^2 $b = 2 \cdot 812$ s mm^{-2} with a voxel size of 1.1×1.1 mm^2 and 10 signal repetitions to increase SNR. The DDE analysis was performed in a region of interest (ROI) defined by applying a threshold to the mean of all diffusion-weighted images. The threshold was chosen such that the ROI comprised the white matter in each section of the spinal cord sample. The overall duration of the DDE experiment was approximately 40 min.

4.3.4 *In vivo* experiments

DDE experiments were performed on eight healthy volunteers (four female, four male; mean age $= 25.75 \pm 2.31$ years, all right-handed) with no known history of neurological disease. Written informed consent was given prior to the scan. In the DDE experiment,

sixteen diffusion gradient directions were used as depicted in Fig. 4.5. Diffusion gradients were applied in the transversal plane (x-y) perpendicular to the subject′s body axis (z) to avoid cross-terms with the slice-selection gradients. Then, the CST can be easily identifiable as an area of hyperintense signal.

For data analysis, a ROI consisted of two parts, comprising the left and right corticospinal tracts in the slices used for diffusion imaging. The ROI was obtained by applying a threshold to the average of all diffusion-weighted images. Twenty axial slices of 3 mm thickness were acquired using 3×3 mm^2 nominal in-plane resolution. Echo and repetition times were $TE = 180$ ms and $TR = 6.5$ s. Additional experiments were performed with volunteers 1 ($TE = 180$ ms, $TR = 4.4$ s) and 7 ($TE = 200$ ms, $TR = 6.5$ s). The acquisition parameters were gradient duration $\delta = 10$ ms, gradient amplitude $\|\mathbf{G}\| = G^{(1)} = G^{(2)} = 44$ mT m^{-1}, diffusion time $\Delta = 62$ ms, gradient rise time $t_r = 900$ μs, mixing time $\tau_m = \delta + t_r$ for all eight volunteers, corresponding to a total diffusion weighting of $b = 2 \cdot 812$ smm^{-2} (and one image with $b = 0$) and 15 signal repetitions in order to increase SNR.

Additional DDE experiments were performed on volunteers no. 7 and 8. For volunteer 7, a longer echo time ($TE = 200$ ms) was chosen in order to accommodate a longer time between the weightings: $\tau_m = \delta + t_r + 15$ ms. For volunteer 8, two additional DDE experiments were performed, using a ψ increment of $\pi/4$ (and $\phi = 0, \pi/2$ only).

In addition, anatomical T_1-weighted images and DTI were acquired for estimating the fiber orientation in the tissue. In the DTI acquisition, a diffusion-weighted spin echo preparation with EPI read-out was employed, using $b = 0$ and 800 s mm^{-2} and thirty-two gradient directions. SPIR fat suppression [59] was also used here. The effective echo time was $TE = 60$ ms, $TR = 14.6$ s, FOV $= 224 \times 224$ mm^2, voxel size 2.1×2.1 mm^2, 70 slices with a thickness of 2 mm. The acquisition time for the DDE experiment was approximately 30 minutes. The total measurement did not take longer than 2 hours.

4.3.5 Data analysis

In spinal cord sample, the ROI over the white matter portion was defined using arbitrary threshold in the diffusion-weighted image created by averaging the DDE images for the 32 different gradient direction. In the *in vivo* acquisitions, the images were realigned to the non-diffusion-weighted image in order to correct for subject motion, using the Diffusion toolbox extension[2] for SPM12[3] in Matlab R2015b (The MathWorks, Natick,

[2]The package can be downloaded from http://sourceforge.net/projects/spmtools

[3]The package can be downloaded from https://www.fil.ion.ucl.ac.uk/spm/software/

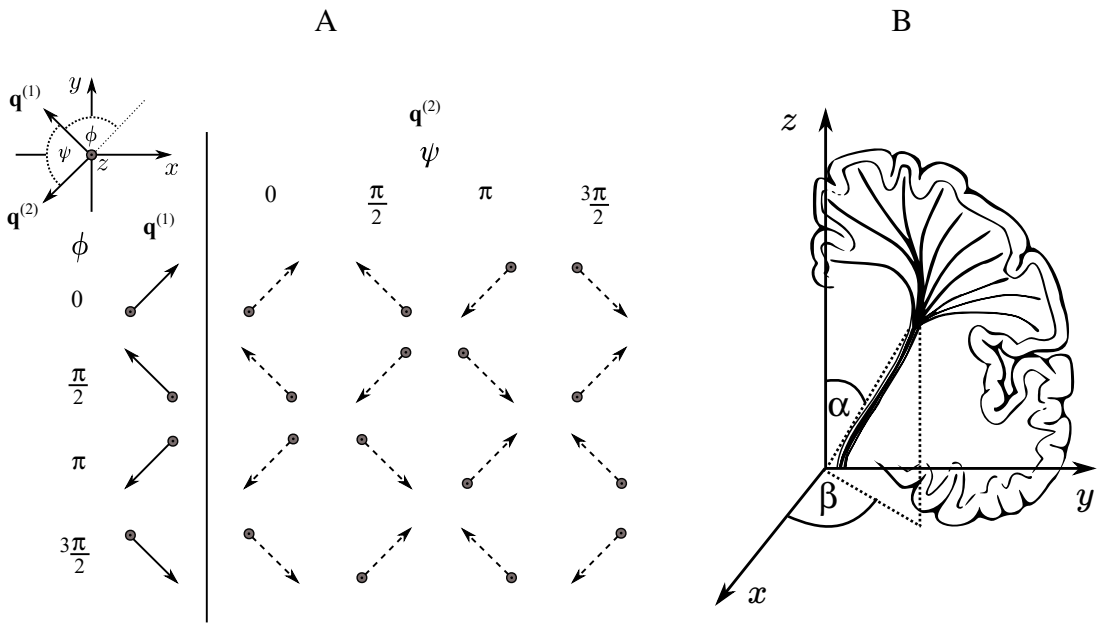

Figure 4.5: **A)** Overview of the diffusion gradient directions in the x-y plane used in the *in vivo* experiments. Sixteen different combinations of diffusion gradient orientations were used, where for a given angle ϕ, $\mathbf{q}^{(1)}$ (solid line) is fixed and $\mathbf{q}^{(2)}$ (dashed line) is rotated about an angle ψ. **B)** Schematic of the DTI-derived angles. α corresponds to the inclination angle of the CST axis with respect to the z-axis, and β specifies how the projection of the CST axis is oriented in the x-y plane.

Massachusetts). For DTI and DDE, the realignment in the *in vivo* images was based on the non-diffusion-weighted images. Any motion between acquiring the $b = 0$ images was not taken into consideration. In DTI only, the effect of motion correction on the value of the diffusion gradient components was accounted for [198].

Regions of interest comprising the left or right CST were defined using an arbitrary threshold in the diffusion-weighted image created by averaging the DDE images for the 16 different gradient direction settings. In the resulting regions, pixels certainly not belonging to the CSTs were manually removed.

As an estimate of the pore size, the scaled parallel–antiparallel attenuation difference,

$$\langle Q \rangle = \frac{3}{2} \frac{\bar{E}^{(g)}(q,0) - \bar{E}^{(g)}(q,\pi)}{q^2}, \tag{4.6}$$

was calculated. In the limiting case with $\delta \ll \tau_D \ll \Delta$ and $(2\pi qa)^2 \ll 1$, where "a" is a typical pore size, and τ_D is the mean time required for diffusion across the pore, the quantity $\langle Q \rangle$ yields the mean-squared radius of gyration if the sample consists of randomly oriented closed pores [28]. With the assumption that the pores are identical

upright cylinders with circular base, it can be translated to a diameter estimate,

$$2r_{\text{lim}} = 2\sqrt{\langle Q \rangle \frac{2}{3} c}, \tag{4.7}$$

with $c \approx 2$ ($c \approx 2.5$ for spheres). This can be found by using the conditions listed above for approximating the analytic signal expressions for spheres and cylinders [108]. By using the geometric mean over gradient orientations that are rotated by $\pi/2$ with respect to each other, the dependence of the attenuation on the fiber direction is removed (if the axons can be represented as cylinders). This can be inferred from the analytical expressions for the attenuation in infinite cylinders accounting for an inclination towards the diffusion gradients [108]. When comparing the *in vivo* results with [29], it should be noted that the latter employs an arithmetic average.

The difference between parallel and perpendicular gradient orientations after taking the geometric mean over gradient settings rotated by $\pi/2$ is given by $\bar{E}_{\parallel}^{(g)} - \bar{E}_{\perp}^{(g)}$, where

$$\bar{E}_{\parallel}^{(g)} = \sqrt{\bar{E}_{\parallel}\bar{E}'_{\parallel}} = \left[\frac{(E(q,0)+E(q,\pi))(E'(q,0)+E'(q,\pi))}{4}\right]^{\frac{1}{2}} \tag{4.8}$$

and

$$\bar{E}_{\perp}^{(g)} = \sqrt{\bar{E}_{\perp}\bar{E}'_{\perp}} = \left[\frac{(E(q,\frac{\pi}{2})+E(q,\frac{3\pi}{2}))(E'(q,\frac{\pi}{2})+E'(q,\frac{3\pi}{2}))}{4}\right]^{\frac{1}{2}}. \tag{4.9}$$

$\bar{E}_{\parallel}^{(g)}$ and $\bar{E}_{\perp}^{(g)}$ are going to be refereed simply as "parallel" and "perpendicular" orientations, respectively.

In the statistical analysis, for each volunteer, four hypotheses about the individual voxel data were statistically tested: (1) $H_{1,1}\colon \bar{E}^{(g)}(q,0) > \bar{E}^{(g)}(q,\pi/2)$ in a region of interest of the image comprising the right CST; (2) as in (1) but for the left CST; (3) as in (1) but for a region of interest comprising the bilateral corticospinal tracts; (4) $H_{1,4}\colon \langle Q \rangle$ is larger in the right than in the left corticospinal tract ROI. For the tests (1) to (3), a Wilcoxon signed-rank test was applied while in (4), a Mann Whitney U test was used. For all statistical tests, the significance level $\alpha = 0.05$ was chosen.

4.4 Results

4.4.1 Simulations

Simulations using MISST were performed to study the DDE diffusion signal in idealized compartments to compare them with the experimental MR results. The DTI information

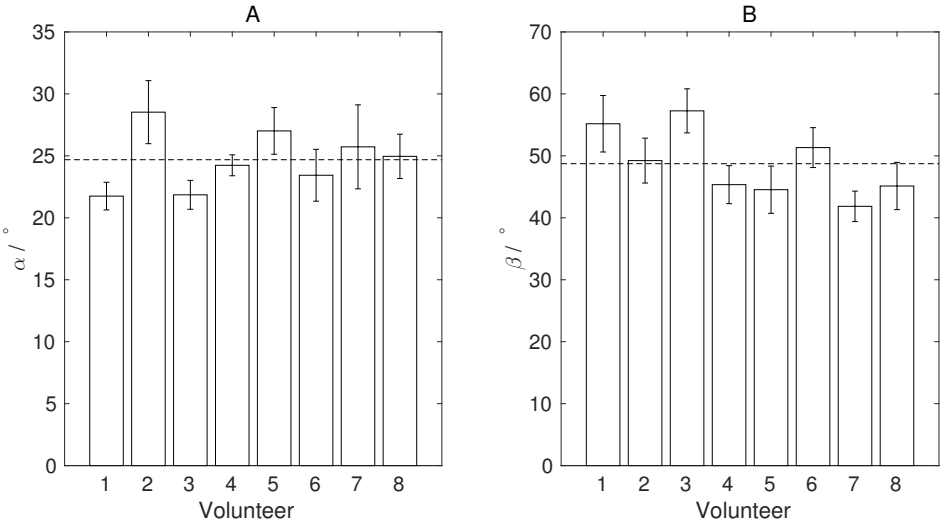

Figure 4.6: Bar plot showing **A)** mean inclination angle of the CST with respect to the z-axis (α), and **B)** the azimuthal angle of its projection on the x-y plane with respect to the x-axis (β). Dashed line shows the mean value among all volunteers (24.68 $\pm$ 2.38 $^\circ$ for α and 48.73 $\pm$ 2.48 $^\circ$ for β).

was used to extract the angle of inclination (α) of the CST with respect to the z-axis and the azimuthal angle (with respect to the x-axis) of its projection on the x-y plane (β). Those results are shown in Fig. 4.6 for all volunteers. For comparison with *in vivo* experiments, the simulations were performed using the DTI data from volunteer no. 8 ($\alpha = 25^\circ$ and $\beta = 45^\circ$).

Here, the feasibility of the geometric mean to average out the effect of microscopic anisotropy in tilted cylinders at short mixing time was explored. Figure 4.7 shows the simulated DDE signal with $\tau_\mathrm{m} = 10.9$ ms for cylinders with 5 different diameters. In Fig. 4.7 A), it can be observed that when the cylinders are not tilted (the plane of the diffusion gradients is perpendicular to the main axis of the cylinders e.g., circular cross-section), the signal intensity is higher for parallel gradients ($\psi = 0$) and lower for antiparallel ($\psi = \pi$), as expected. It shows the expected $\cos(\psi)$ profile for untilted cylinders, for which the amplitude depends on the diameter size. However, for tilted cylinders the signal modulation depends on the initial orientation of $\mathbf{G}^{(1)}$ and corresponds to a $\cos(2\psi)$ signal dependency. When $\mathbf{G}^{(1)}$ was applied in the x-y plane with $\phi = 0$ equivalent to the azimuthal angle obtained from the DTI data (β), the signal modulation shows 2 maxima at $\psi = \pi/2$ and $\psi = 3/2\pi$ and three minima at $\psi = 0$ and $\psi = \pi$, as shown in Fig. 4.7 B. However, when rotating $\mathbf{G}^{(1)}$ 90° ($\phi = \pi/2$) the signal modulation is inverted, as seen in Fig. 4.7 C. These results agree well with previous publication from Morozov et al. [175].

To study the DDE signal for different intraaxonal volume fractions, the simulated diffu-

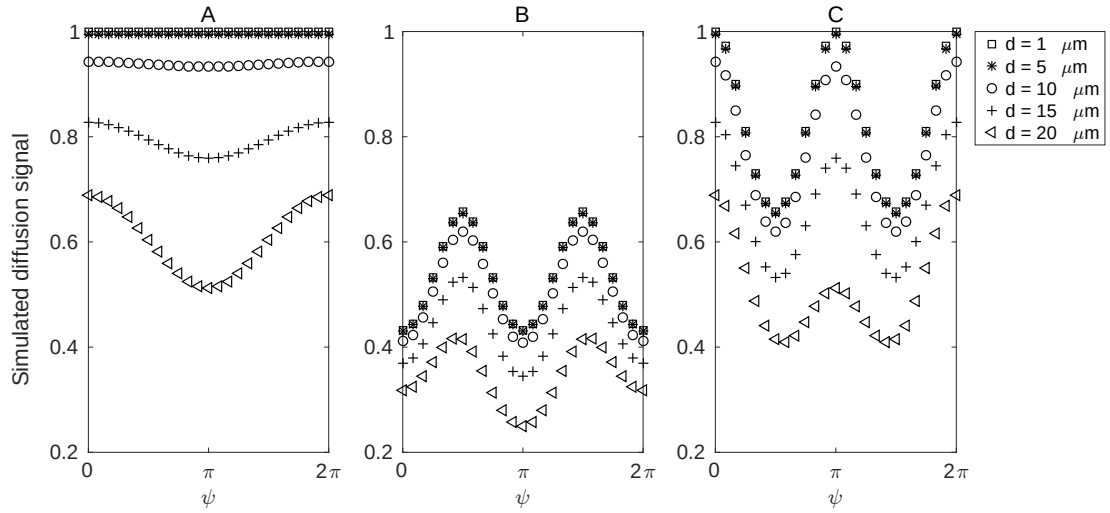

Figure 4.7: Simulated diffusion signal for water-filled cylinders of five different diameters. **A)** untilted cylinders, **B)** tilted cylinders ($\alpha = 24.5°$) with $\phi = 0$, and **C)** tilted cylinders with rotated diffusion gradients $\phi = \pi/2$.

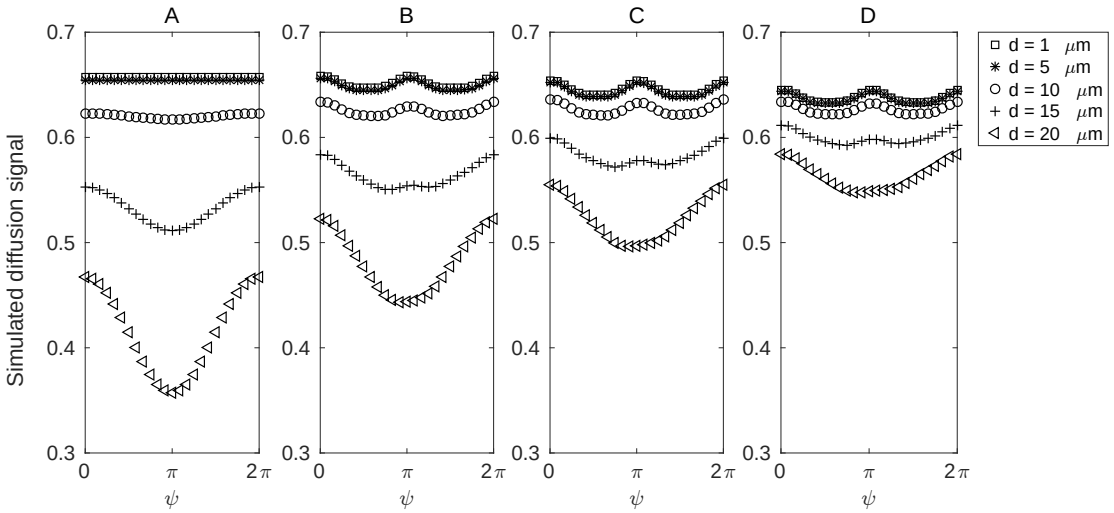

Figure 4.8: Simulated diffusion signal of different volume fractions after taking the geometric mean over the $\phi = 0$ and $\phi = \pi/2$ cases. The intracellular space (volume fraction f_i) is represented by cylinders of 3 different diameters, and the extracellular space is described by a diffusion tensor (diffusivities obtained from the DTI analysis performed on volunteer no. 8). **A)** $f_i = 1$ (no extracellular component), **B)** $f_i = 0.7$, **C)** $f_i = 0.5$, **D)** $f_i = 0.3$. For low intracellular volume fractions, the simulations show a W-shaped modulation, in particular for small cylinder diameters. This can be taken as a sign of an eccentric compartment dominating the DDE signal. For cylinders with a diameter larger than 10 μm, the W-shaped modulation disappears (data not shown).

sion signals from tilted cylinders (representing the intraaxonal space) and tensor (simulating extracellular space) were added in order to observe how the signal modulation behaves with different intra- and extracellular components. The angles α and β were extracted from the DTI acquisition from volunteer no. 8. Figure 4.8 shows the results for different volume fractions. In the first plot, corresponding to a situation without extracellular space, it can be seen that after the geometric mean over perpendicular orientations in the laboratory frame (specified by ϕ), the signal behaves just as if it came from untilted cylinders, showing a characteristic $\cos(\psi)$ profile if the cylinder diameter is large enough. For higher extracellular volume fractions, a W-shaped profile, $\cos(2\psi)$, occurs for cylinders with diameters below 10 μm (after the geometric mean).

4.4.2 Spinal cord experiment

Figure 4.9 A shows the signal modulation in the ROI comprising the white matter in the spinal cord sample. The signal modulation for each independent ϕ resembles the predicted cosine signal profile [28, 108]. However, not for all ϕ the minimum occurs at $\psi = \pi$. This is consistent with the presence of fibers that are, to some degree, tilted towards the plane of the diffusion gradients. After taking the geometric mean over absolute orientations (ϕ) in the laboratory frame, the signal showed the behavior expected for an untilted cylindrical compartment with C_∞ symmetry. Figure 4.9 B and Fig. 4.10 A show the parallel–perpendicular signal difference, which was calculated after taking the geometric mean over four perpendicular orientations in the laboratory frame (ϕ values).

Color-map of the parallel–perpendicular signal difference over a ROI covering the white matter of the spinal cord and its histogram are shown in Fig. 4.10 A and Fig. 4.9 B. The ROI mean of the parallel–perpendicular difference amounts to $(0.011 \pm 0.003$. The parallel–perpendicular signal difference was calculated after taking geometric mean among four perpendicular ϕ. In white matter in the spinal cord sample, the diffusion signals for the parallel orientations, $\bar{E}^{(g)}(q, 0)$, were not found to be significantly different from the perpendicular ones, $\bar{E}^{(g)}(q, \pi/2)$.

Figure 4.10 B and C show the color-maps $\langle Q \rangle$ and mean pore diameter estimation in the porcine spinal cord sample, where the means amount to (2.7 ± 0.9) μm^2 and (2.9 ± 0.4) μm, respectively.

4.4.3 *In vivo* experiments

The angular dependence of the geometric signal mean over the four perpendicular orientations of the gradient vectors in the laboratory system (i.e., over a column in Fig. 4.5

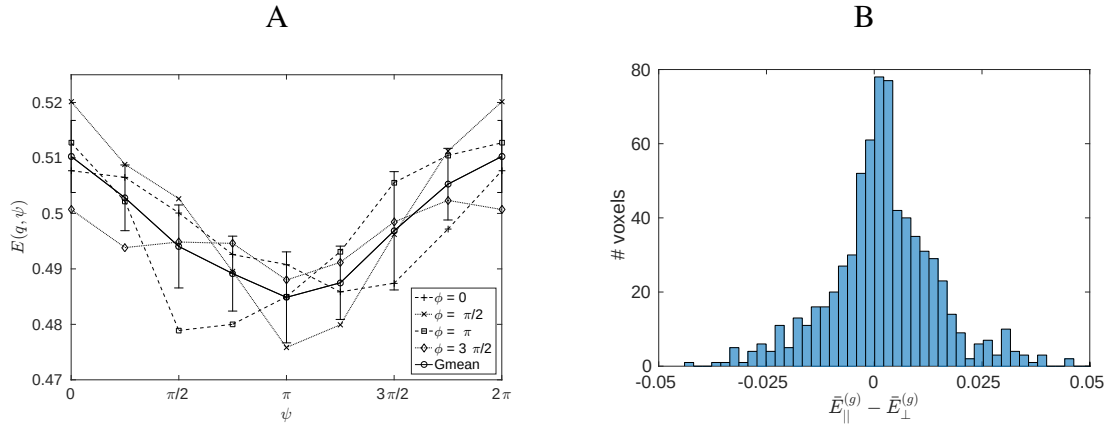

Figure 4.9: Analysis white matter section of the porcine spinal cord sample. **A)** Attenuation of the DDE-weighted signal vs. angle ψ between the diffusion wave-vectors, for different orientations ϕ in the laboratory frame. "Gmean" denotes the geometric mean overall ϕ, the bars represent the standard deviation between different ϕ values. After taking the geometric mean over ϕ, the signal modulation is consistent with the assumption that the signal arises from compartments that are circular cylinders, perpendicular to the plane spanned by the diffusion gradients. **B)** Histogram of the values within the ROI. The parallel–perpendicular attenuation difference (after geometric mean) amounts to a low average over the ROI, suggesting low in-plane eccentricity.

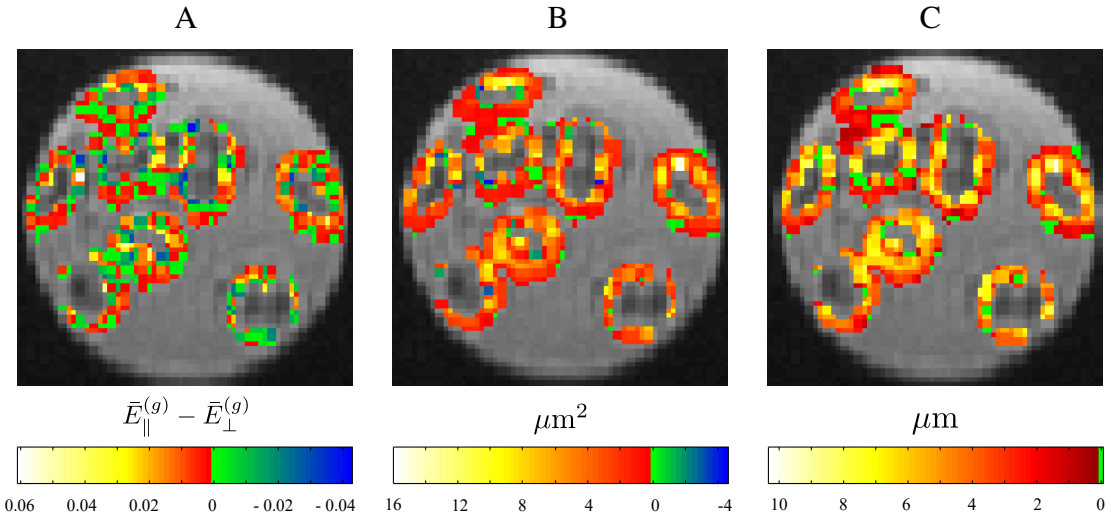

Figure 4.10: **A)** Color-coded map of the attenuation difference between parallel and perpendicular orientations (after taking the geometric mean among ϕ) in the ROI covering the white matter in the porcine spinal cord. In **B)** and **C)** Color coded maps of the mean squared radius of gyration $\langle Q \rangle$ and estimated pore diameters in the ROI. Maps are overlaid on an image of the average of thirty-two gradient directions.

A) can be seen in Fig. 4.11 A. The signal profile exhibits minima at the perpendicular directions ($\psi = \pi/2$ and $\psi = 3\pi/2$), which is consistent with the signal originating in an eccentric compartment. After separately averaging over parallel and antiparallel and between the perpendicular orientations, (as in Eq. (4.8) and Eq.(4.9)) the signal intensities from parallel orientations were significantly larger than those from perpendicular ones, yielding positive results ($\bar{E}^{(g)}(q,0) - \bar{E}^{(g)}(q,\pi/2) > 0$) in the region-of-interest (ROI) covering both CSTs in all volunteers. Figure 4.11 B shows a color map of this difference in the area covering the CST in volunteer no. 8 and Fig. 4.12 shows the mean difference between parallel and perpendicular gradient orientations for all volunteers. Figure 4.11 C shows the histogram of parallel–perpendicular differences in the CST ROI for volunteer no. 8.

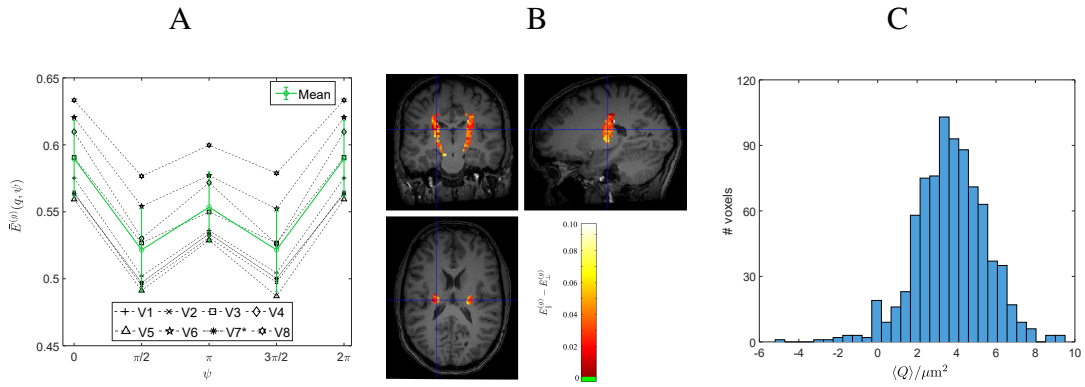

Figure 4.11: *In vivo* results in a ROI comprising both CST, defined using an arbitrary threshold. Voxels that did not belong to CST were manually removed. **A)** Attenuation of the DDE-weighted signal vs. angle ψ between the diffusion wave vectors, geometrically averaged over signals with all diffusion gradients rotated by $\pi/2$ and arithmetically averaged over the ROI. "Mean" is the arithmetic mean over all volunteers (*: $TE = 200$ ms). The geometric mean should have removed any signal modulation due to a simple inclination with respect to the plane spanned by the diffusion gradients. The minima at $\psi = \pi/2$ and $\psi = 3\pi/2$ suggest an eccentric shape of the signal-dominating compartment. **B)** *In vivo* results for subject no. 8; parallel–perpendicular attenuation difference for the DDE-weighted signal. After taking the geometric mean over signals with all diffusion gradients rotated by $\pi/2$ as in Fig. 4.9 B. In the bilateral CST ROI, overlaid with the T_1-weighted image (coronal, sagittal and axial view). The relatively large differences found in the CST suggest the protons to reside in a more eccentric compartment, as compared to the spinal cord sample. **C)** Histogram of the parallel–perpendicular differences shown in (A) for the ROI covering the CST

The volunteer-mean of the size estimate $\langle Q \rangle$ (shown in Fig. 4.13 A for volunteer no. 8) derived from the antiparallel–parallel signal difference *in vivo* was (3.9 ± 0.5) μm^2, in an area covering both CST, in an area covering both CSTs (ROI mean, averaged over all volunteers). This value agrees well with previously published results[29]. It corresponds

to a cylinder diameter of $2r_{\text{lim}} = (4.6 \pm 0.3)\ \mu$m.

Figures 4.13 B and 4.15 show a color-coded diameter map for volunteer no. 8 and average diameter for all volunteers, respectively. These results agrees well with previously published results [29].

A significant statistical difference in $\langle Q \rangle$ left and right CST was expected and was found for seven volunteers. Only volunteer no. 5 did not show a statistically significant difference between left and right $\langle Q \rangle$ in the CST. Figure 4.14 shows the $\langle Q \rangle$ results for all volunteers.

The two additional experiments with a smaller ψ increment were performed on volunteer no. 8. They aimed at studying the signal dependence on the angle ψ in left and right CST in more detail. The results are shown in Fig. 4.16, separately for the two ϕ values used, without employing a geometric mean. For the first experiment (Fig. 4.16 A, $\mathbf{G}^{(1)}$ was fixed to the $(x = 1, y = 1, z = 0)$ direction and $\mathbf{G}^{(2)}$ was rotated stepwise about the z-axis. The left CST shows minima for perpendicular gradient orientations ($\psi = \pi/2$ and $\psi = 3\pi/2$). As far as the noise level permits, a more complex profile can be observed in the right CST DDE signal: it is shifted, and the minima exhibit different signal levels. The opposite behavior was observed in the second experiment (Fig. 4.16 B), where $\mathbf{G}^{(1)}$ was fixed to the $(1, \text{-}1, 0)$ direction.

Experiment on volunteer no. 7, where a longer τ_{m} was used ($\tau_{\text{m}} = 25.9$ ms) ($TE = 200$ ms) did not a show significant difference with the acquisition at short τ_{m}.

4.5 Discussion

4.5.1 Simulations

The DDE signal depends on the inter-weighting angle, a $\cos(2\psi)$ dependence can indicate the presence of compartments that do not have rotational (C_∞) symmetry in the plane of the diffusion gradients. In a bundle of parallel fibers, the complication arises when the signal also shows such a dependence if the fibers resemble circular cylinders but are not perpendicular to the diffusion gradient plane, leading to eccentric cross-sections. The main approach in this work is to use the geometric mean over perpendicular orientations of the diffusion gradient pair in the laboratory frame. This is a way to eliminate the effect of eccentric cross-sections that arise from an inclination of fibers towards the plane spanned by the diffusion gradients. This is used to investigate how far the extracellular compartment contributes to DDE-based measurements of pore size. For tilted parallel cylinders without extracellular space, Fig. 4.8 (case $f_i = 1$) demonstrates that taking the

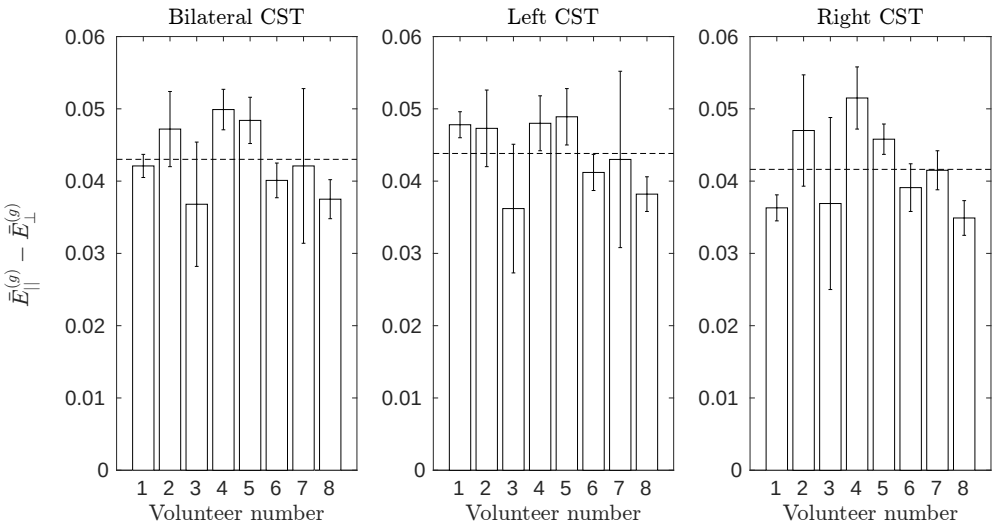

Figure 4.12: The bar plot shows the parallel–perpendicular gradient orientation difference (after the geometric mean over ψ) for all volunteers. Dashed line marks the mean value of the parallel–perpendicular signal difference. **A)** For a ROI covering both CST the mean value ($\pm$ standard deviation) is (0.043 ± 0.005); **B)** for a ROI covering the left CST (0.044 ± 0.005), and **C)** for a ROI covering the right CST is (0.042 ± 0.006).

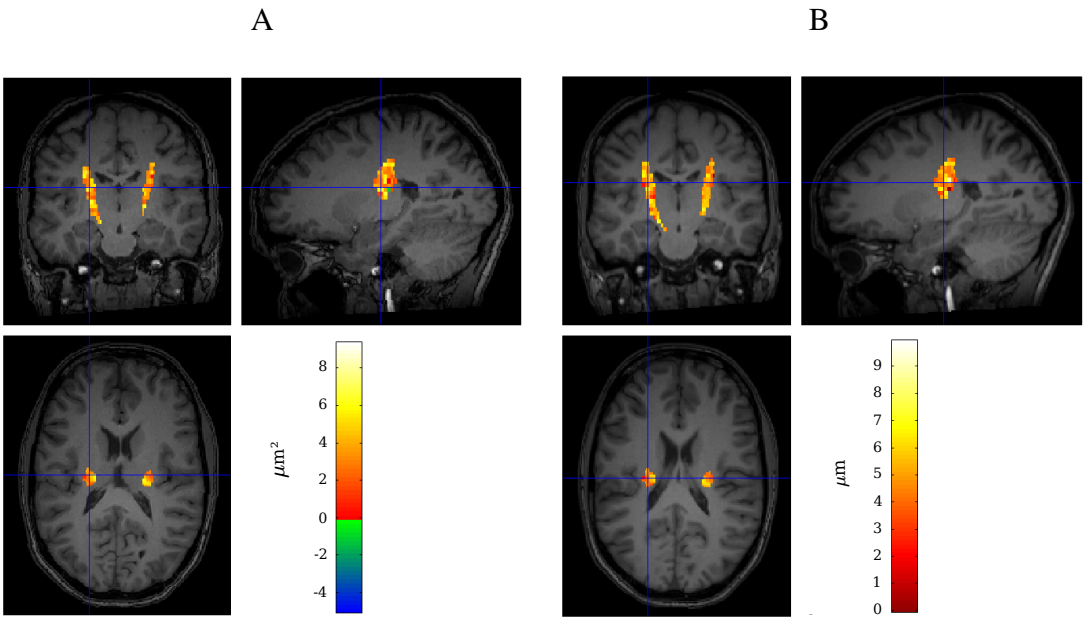

Figure 4.13: **A)** Color-coded map of the $\langle Q \rangle$ for volunteer no. 8, superimposed on a T_1 weighted image. Negative values could occur due to noise (if $E(q,0) < E(q,\pi)$). **B)** Color-coded map of the estimated compartment diameter size for subject no. 8 in CST, overlaid on a T_1-weighted image. Coronal, sagittal and axial view of the human brain are shown.

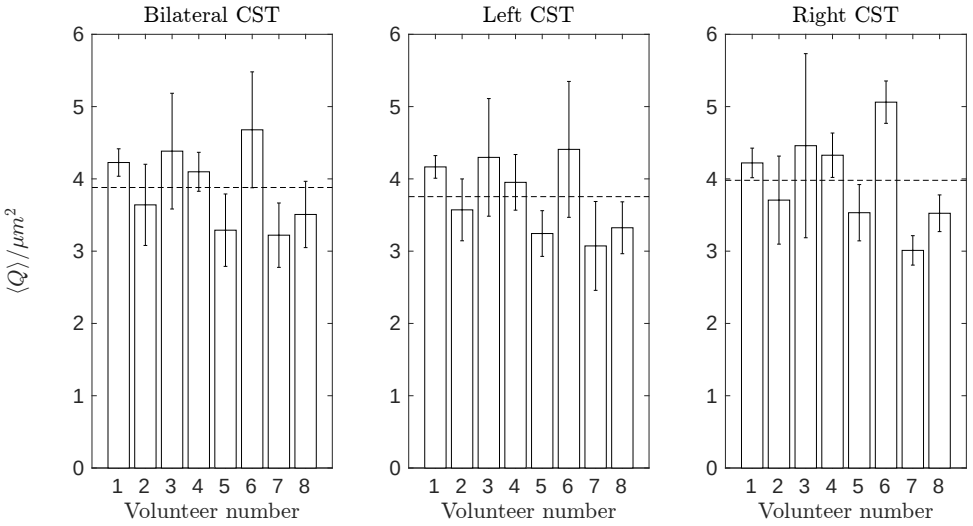

Figure 4.14: Bar plot showing the $\langle Q \rangle$ results for all volunteers. Dashed line marks the mean value of $\langle Q \rangle$. **A)** For a ROI covering both CST the mean value ($\pm$ standard deviation) is (3.9 ± 0.5) μm^2; **B)** for a ROI covering the left CST (3.8 ± 0.5) μm^2 and **C)** for a ROI covering the right CST is (4.0 ± 0.7) μm^2.

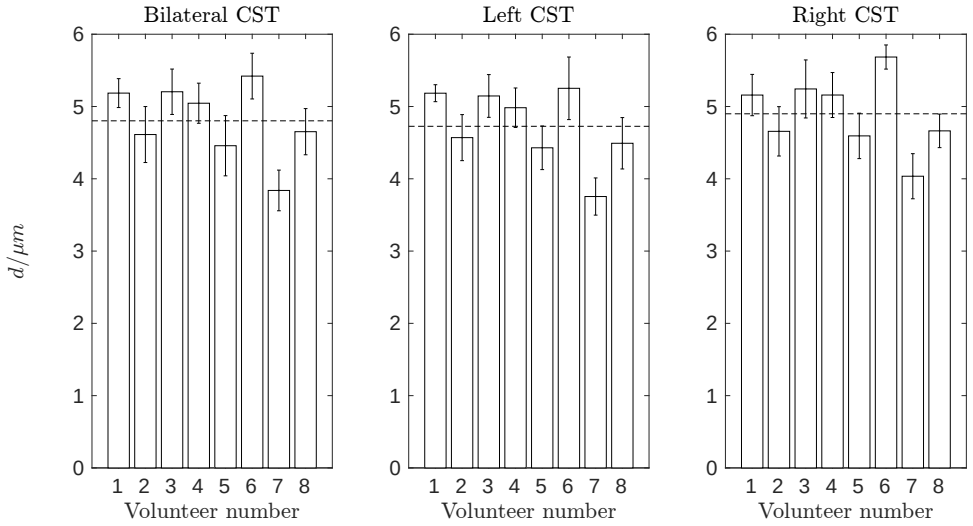

Figure 4.15: Bar plot showing the estimated diameter d in the area of the CST for all volunteers. Dashed lines mark the mean diameter among the volunteers. **A)** For a ROI covering both CST the mean value ($\pm$ standard deviation) is (4.8 ± 0.5) μm; **B)** for a ROI covering the left CST is (4.7 ± 0.5) μm, and **C)** for a ROI covering the right CST is (4.9 ± 0.5) μm.

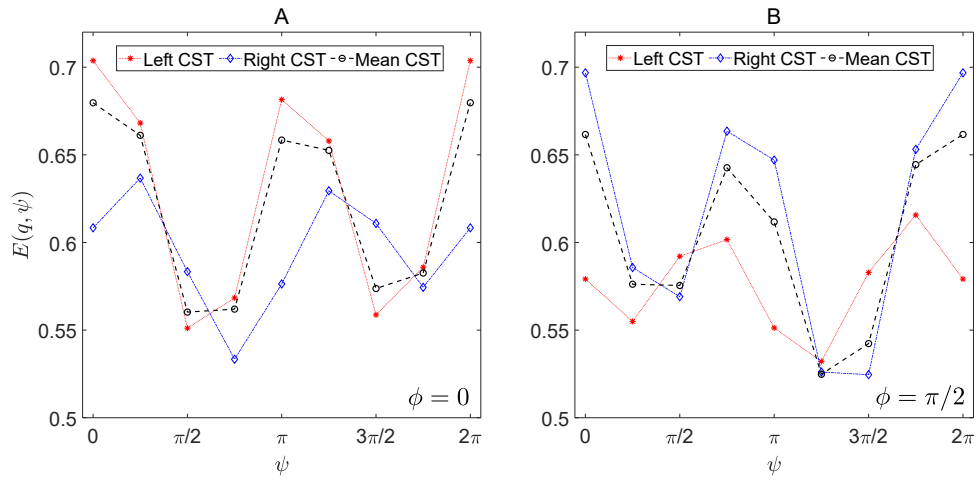

Figure 4.16: *In-vivo* results for volunteer no. 8; DDE-weighted signal attenuation (averaged over a ROI comprising the left or right CST) vs. the angle ψ between diffusion gradient wave vectors. The first diffusion gradient, which is constant in each subplot, is set to **A)** $\mathbf{G}^{(1)} = (G, G, 0)/\sqrt{2}$ (i.e., $\phi = 0$) and **B)** $\mathbf{G}^{(1)} = (G, -G, 0)/\sqrt{2}$ (i.e., $\phi = \pi/2$), respectively.

geometric mean over the $\phi = 0, \phi = \pi/2$ cases effectively suppresses the effect of eccentric cross-sections in the diffusion signal, resulting in a $\cos(\psi)$ profile. However, when the signal from tilted cylinders is mixed with that from an extracellular component (described by a tensor model in the simulations as shown in Fig. 4.8), the geometric mean does not completely eliminate the signal minima at perpendicular gradient orientations. This can be attributed to diffusion along the directions perpendicular to the first tensor eigenvector (corresponding to the largest eigenvalue), which is aligned with the cylinder axis. Hence, under the assumption that the intra-axonal compartment in white matter can be modeled as cylinders with circular base, any observed parallel–perpendicular difference surviving the geometric mean, as in $\cos(2\psi)$, can be attributed to either (1) contributions from eccentric extracellular compartments that do not have a common orientation throughout the voxel or (2) fiber dispersion in the voxel. Generally speaking, in experiments using diffusion gradients in the x-y plane, both cylinders along the z axis but with elliptical base and inclined cylinders with circular base can induce anisotropy of the apparent diffusion coefficient in the x-y plane. The distinction between these two cases may be possible by more specialized diffusion experiments.

4.5.2 Spinal cord experiment

The results showed that after averaging over four ϕ, separeted by π/2, the signal exhibits the cosine modulation predicted for spherical pores, e.g. at "short" τ_{m} ($\tau_{\mathrm{m}} = \delta + t_r$). Since

the plane of the applied diffusion gradients is approximately perpendicular to the cylindrical fibers, the cross-section is assumed to be a circle, as illustrated in Fig. 4.2 B, and a cosine modulation in that plane is expected. The estimated diameter agrees well with histological results provided by Komlosh et al. [188] for porcine spinal cord. Nonetheless, care needs to be taken since histological studies in porcine spinal cord showed that axon diameter [188, 88] and axon density and myelin membrane thickness [199] vary between different white matter tracts. The current experiment did not provide statistical evidence that the diffusion signal using parallel gradients was different from that using perpendicular ones. Hence, there is no indication of a compartment with a non-circular cross-section, such as eccentric extracellular compartments of random orientation. The axon density can be correlated with the restricted water fraction (intra-axonal water) [87], which was reported to be 44 % in spinothalamic tract and 55 % in the cuneatus in spinal cord in humans *in vivo* [200]. The intracellular water fraction in the CST was also reported to be slightly higher at the *Capsula interna* level than at more cranial parts [201]. However, a common problem with formalin fixation is that it dehydrates the sample [202]. This means that the axon density may be higher in fixed than in fresh specimens. In a densely packed fiber tract, the extracellular space is likely to have a circular horn triangle cross-section (see Fig. 4.2B). Such a shape is not expected to induce parallel–perpendicular differences in the DDE signal.

4.5.3 *In vivo* experiments

The *in vivo* results shown in Fig. 4.11 A exhibit minima at perpendicular gradient orientations, in accordance with expectation. In contrast to the spinal cord sample, the geometrically averaged *in vivo* results did show a statistically significant difference between parallel and perpendicular diffusion gradient orientations in all volunteers. Hence, the geometric mean does not successfully suppress the signal difference between parallel and perpendicular diffusion gradient orientations in the human CST *in vivo*. This suggests the contribution of an unaligned compartment without rotational symmetry, or the presence of different fiber directions per voxel. The more pronounced signal dependence on the intergradient angle without averaging over absolute orientations specified by ϕ (Fig. 4.16) is consistent with a cylindrical compartment that is tilted away from the z axis. A signal difference between the two minima was observed. Such curve asymmetries were observed in previously published DDE data [121]. They may arise from cross-terms with residual background gradients. Note that, in the other experiments, such cross-terms would also be suppressed by taking the geometric mean over all four ϕ values [166], rendering the graphs in Fig. 4.11 symmetric.

While the order could have an influence due to eddy currents, it is irrelevant otherwise. An angle $\beta \approx 45°$ was determined from the DTI data in this volunteer. Hence, the projection of the right CST onto the x-y plane is almost parallel to the (1,1,0) direction, along $\mathbf{G}^{(1)}$ at $\phi = 0$. This is consistent with the stronger signal attenuation in the right CST in Fig. 4.16 as compared with the left CST. The brain's left-right symmetry causes the left CST projection to have $\beta \approx -45°$, coinciding with the $\phi = \pi/2$ line. Reflecting the gradient pair about the (1,1,0) line leads to an interchange of the relative angles subtended by the gradient pair and the left and right CST. This explains the observed symmetry between the curves in Fig. 4.16. The minima in the right CST graph for $\phi = 0$ may be due to between-voxel differences of the fiber projection onto the x-y plane.

Some degree of fiber dispersion can be found in different white matter tracts [203, 204, 205]. Indeed, the region investigated here is part of the *Corona radiata*, where the ascending CST fibers diverge. However, within the *Capsula interna*, fibers are expected to be most densely packed. Hence, it appears unlikely that the observed minima at perpendicular orientations purely arise from intravoxel fanning of fibers.

In one volunteer, an additional experiment was performed that aimed at a comparison between the mixing times $\tau_{m1} = 10.9$ ms and $\tau_{m2} = 25.9$ ms. The difference between parallel and antiparallel orientations is expected to vanish at long τ_m for spherical compartments (isotropic) [28]. However, no statistically significant difference was found between the diffusion attenuation obtained for $\tau_{\mathrm{m},1}$ and $\tau_{\mathrm{m},2}$. The reasons for this result remain unclear. Possibly, the chosen mixing time $\tau_{\mathrm{m},2}$ was not long enough. This would be consistent with the view that a relatively large compartment dominates the parallel–antiparallel difference: the parallel–antiparallel difference decays only slowly with increasing τ_m if the compartments are large [107, 206].

The calculated size estimates $\langle Q \rangle$ observed in the CST were similar to the values found in a previous study [29], where fitting an analytic signal expression [108] to the experimental data yielded cylinder diameters of approximately 13 μm. In histological studies of the human CST, axon diameters between 0.5 μm [207] and 20 μm [208] were found after fixation, where 84 % of the fibers are smaller than 2 μm [209]. In fixed human spinal cord white matter, the diameter distribution was reported to peak between 2 and 4 μm [154]. Given these values, the results presented here are in the correct order of magnitude but relatively large. A possible reason for the parallel–perpendicular difference surviving the geometric mean could be that the axonal cross-section is intrinsically eccentric, i.e. that the axonal compartment resembles a cylinder with elliptic base. In cats, the circularity index (ratio of the shortest and the largest cross-sectional diameter) was demonstrated to range from 0.8 to 0.9, approximately, and to decrease with increasing diameter

[210]. Hence, the vast majority of fibers are thin and have an almost circular perpendicular cross-section. However, large-diameter fibers comprise a relatively high volume and hence make a high relative contribution to results based on diffusion-weighted MR techniques. Still, the method chosen here is not very sensitive to slight deviations from the circular shape. Overall, it appears unlikely that the intra-axonal compartment shape deviates sufficiently from a circular cylinder to induce the observed behavior. It should be noted that only few axons can be expected to have diameters above the resolution limit for diffusion-based cylinder diameter estimation using standard clinical MRI systems. This limit was estimated to lie somewhere between 4 and 8 μm [211]. In addition, it was pointed out before that DDE-based measurements are biased to larger pore diameters because the amplitude of the ψ modulation increases with the pore size [29]. Here, the quantity $\langle Q \rangle$ was used as an estimate of the pore size. The cylinder diameter itself could be derived from fitting the data with the analytic expressions describing the DDE signal [108]. In contrast to using the quantity $2r_{\mathrm{lim}}$ (Eq. 4.7), this would also account for finite values of δ, Δ, and τ_{m} [29]. For the purpose of the present work, however, this was not required.

Post-mortem studies have described anatomical differences between left and right CST axonal size [212]. In this work, a statistically significant difference in $\langle Q \rangle$ was found between left and right CST in 7 out of 8 volunteers. This directly translates to a difference in the estimated diameter. Here, the right CST was found to have larger compartments than the left one, where the estimated compartment size is in the same order of magnitude as in Kamiya et al. [201]. Similar left–right differences were reported previously [213]. This asymmetry is essential for the understanding of several brain illnesses as, for example, multiple sclerosis or stroke, where the asymmetry between tracts is expected to be larger than in healthy subjects [214].

4.6 Conclusion

This study aimed to determine whether a pore size estimate in the CST based on double diffusion encoding measurements may reflect the extracellular space rather than the intra-axonal compartment. To this aim, it was exploited that the twice diffusion-weighted signal used for size assessment also depends on the compartment shape. This dependence leads to a signal difference between parallel and perpendicular diffusion gradient orientation. However, such a difference also occurs for cylinders with a perfectly circular base if the cylinder axis is not perpendicular to the plane spanned by the diffusion gradients. A geometric mean was employed to average out the effect of such an inclination, taken

over measurements differing by a 90° rotation of all diffusion gradients about the axis perpendicular to the diffusion gradients.

Eight volunteers were investigated *in vivo*. In all of these, a parallel–perpendicular signal difference after the geometric mean was observed. The results suggest a not negligible contribution of the interstitial compartment to the pore size estimate obtained with this double diffusion-encoding approach. However, the results are also consistent with the intra-axonal compartment being the predominant signal origin combined with a sufficiently broad orientation distribution of the axonal fibers in the voxels investigated. To rule out this alternative explanation, further experiments would be required. It should further be noted that the results presented cannot easily be transferred to experiments employing different experimental parameters as these possibly are associated with different relative signal contributions.

Care needs to be taken in analyzing size estimates calculated from DDE measurements. Misestimation of fiber dimensions might influence the correct diagnosis of neurological pathologies. Even though DWI is a relevant clinical tool there is still no consensus on the origin of the changes in ADC due to e.g. stroke [13, 12]. Determining the origin of the diffusion-weighted signal is a fundamental step for understanding the biophysical phenomena underlying pathological processes. The sensitivity of the twice diffusion-weighted signal to both pore shape and size may turn out helpfull in investigating subtle pathological and physiological changes in the microscopic structure of brain or other tissues. Possible applications may be possible in a number of tissues and pathologies, including pathological changes of the tissue microstructure in the corticospinal tracts. Such changes appear for instance due, to the death of individual axons in motor neuron disease [215] or in Wallerian degeneration due to stroke [216].

5

Bias in apparent exchange rate measurements

5.1 Introduction

In the brain, during molecular exchange, water can pass directly through the cellular membrane, or via specialized channels called aquaporins [35]. When the aquaporins' mechanism to control membrane permeability is affected, pathological conditions such as cancer [39] and brain edema [38, 217] can occur. Therefore, there is a need to develop methods to study water exchange across cell membranes in a non-invasive manner [40, 32]. Double diffusion encoding (DDE), which comprises two diffusion-weighting periods separated by a variable mixing time between excitation and acquisition, provides non-invasive means to investigate molecular exchange between compartments. In the study of molecular exchange, Callaghan and Furó [110] developed the diffusion exchange spectroscopy (DEXSY) technique. This technique considers a two-compartment system, where molecules diffuse during the mixing time. Applying an inverse Laplace transform generates a 2 D diffusion spectrum, where the off-diagonal peaks are a signature of molecular exchange between compartments [110].

A disadvantage of the DEXSY method is that it requires an MR system with strong

gradient systems and long acquisition times. Therefore, Åslund et al. [40], developed filter exchange spectroscopy FEXSI based on DEXSY. In contrast with DEXSY, FEXSY replaces the variable gradient strength in the first diffusion-weighted block (also called "filter block") with a fixed gradient, significantly reducing the acquisition time of the experiments. By doing this, the ADC of the different compartments do not depend on the time scale for exchange of the experiments. This results in a simpler mathematical data analysis. Additionally, the FEXSY protocol is optimized to allow a model-free analysis, being the basis for the imaging version implemented by Lasič et al. [32].

Filter exchange imaging (FEXI) [32] is the imaging version of FEXSY, which introduces the concept of Apparent eXchange Rate (AXR) as a model-free method to estimate molecular exchange between compartments. For measuring AXR [32], a stimulated echo version of DDE (DDE-STE) (see Fig. 5.1) is used, and the time between the two innermost diffusion gradient pulses, τ_{m}, is varied (increased), while all the other parameters remain constant. For the FEXI method, to estimate an AXR, the theory considers a system in which water molecules can be separated into two components: one with "slow" (s) moving spins, and a second one, with "fast" (f) moving spins, as shown in Fig. 5.2. In the sequence shown in Fig. 5.1, the first pair of diffusion gradient pulses acts as a "diffusion filter", attenuating the signal from the "fast" diffusing spins. The second diffusion gradient pulse pair is used to calculate a τ_{m}-dependent apparent diffusion coefficient, $ADC'(\tau_{\mathrm{m}})$, from [32]

$$S(b, \tau_{\mathrm{m}}) = S_{\mathrm{f}}(\tau_{\mathrm{m}}) \exp[-ADC'(\tau_{\mathrm{m}})\, b], \tag{5.1}$$

where $S_{\mathrm{f}}(\tau_{\mathrm{m}})$ is the signal from an experiment with $\mathbf{G}_2 = 0$, $b = (\gamma\delta\mathrm{G})^2 t_{\mathrm{d}}$ and $t_{\mathrm{d}} = \Delta - \delta/3$.

Then, the $ADC'(\tau_{\mathrm{m}})$ is given by [32]

$$ADC'(\tau_{\mathrm{m}}) = ADC\,[1 - \sigma \exp(-AXR\,\tau_{\mathrm{m}})]. \tag{5.2}$$

where ADC (also called "equilibrium ADC") is obtained from an experiment with no active diffusion filter ($\mathbf{G}_1 = 0$), as in a single diffusion experiment, such as

$$S(b) = S_0 \exp(-ADC\, b), \tag{5.3}$$

where S_0 is non-diffusion weighted. The equilibrium ADC is reached once the τ_{m} is long enough so that the effect of the filter block is negligible. The efficiency of the diffusion filter, σ, is a quantification of $ADC'(\tau_{\mathrm{m}})$ reduction after the application of the first diffusion weighting (with values from 0 to 1). The value of σ is related to the difference between intra- and extracellular apparent diffusivities, and to the effect of the diffusion filter on the fractional water population [32, 42].

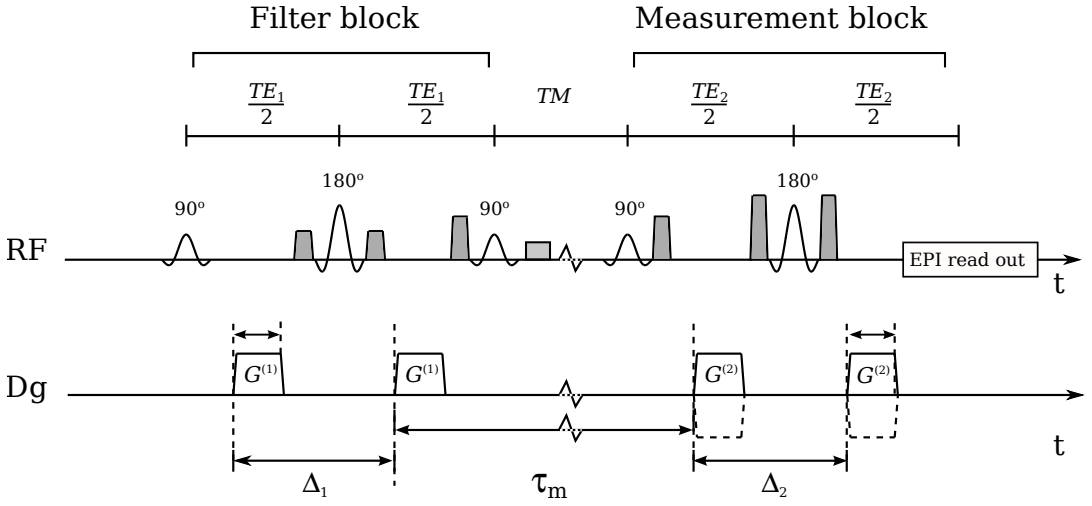

Figure 5.1: DDE-STE pulse sequence. The filter block is followed by the detection block, separated by time TM. Diffusion gradients are shown in the "Dg" timeline, where δ_{f} and δ are the gradient durations for $\mathbf{G}^{(1)}$ and $\mathbf{G}^{(2)}$, respectively. The diffusion time during the filter block and measurement block are Δ_{f} and Δ, respectively. Diffusion gradients drawn with a solid line correspond to an experiment with $\psi = 0$, while diffusion gradients drawn with dashed lines correspond to $\psi = \pi$.

Promising results have been published in the estimation of molecular exchange in terms of AXR in yeast [32], cancer cells [41], and in humans *in vivo* [42, 43, 44, 45].

However, DDE is also sensitive to other microstructural characteristics of a sample [27, 117]. These features include estimation of size [117] and shape of compartments (e.g., cells) [112, 152], and perfusion fraction [187]. Further to the sensitivity of DDE to molecular exchange, all those effects are entangled together. One simple way to isolate those effects is to vary the mixing time. For $\tau_{\mathrm{m}} = 0$, the theoretical work performed by Mitra [28] predicts when varying the angle between the diffusion gradients (ψ), and under idealized conditions (i.e. $\delta \to 0$ and $\Delta \to \infty$), a cosine angular dependence of the diffusion-weighted signal, $S(q, \psi)$, is expected. The signal amplitude will be proportional to the size of the compartment when $\tau_{\mathrm{m}} = 0$ for small values of $q = \gamma\delta G$ (γ: gyromagnetic ratio, δ: gradient duration and G: gradient strength). The signal amplitude increases with the pore size and is independent of the pore shape. Experiments have shown that it is possible to estimate sizes in various samples: chive [218], water-filled microcapillaries [130, 127, 142], emulsions, quartz sand, yeast [136] and isolated grey matter from pigs [120] using an MR spectrometer; and in the space between plastic beads, radish, porcine spinal cord [107] and *in vivo* human brain [29] using clinical MR systems.

The situation changes when the mixing time is long. At $\tau_{\mathrm{m}} \to \infty$, the angular dependence of the diffusion signal vanishes for spherical pores [28]. However, for non-spherical

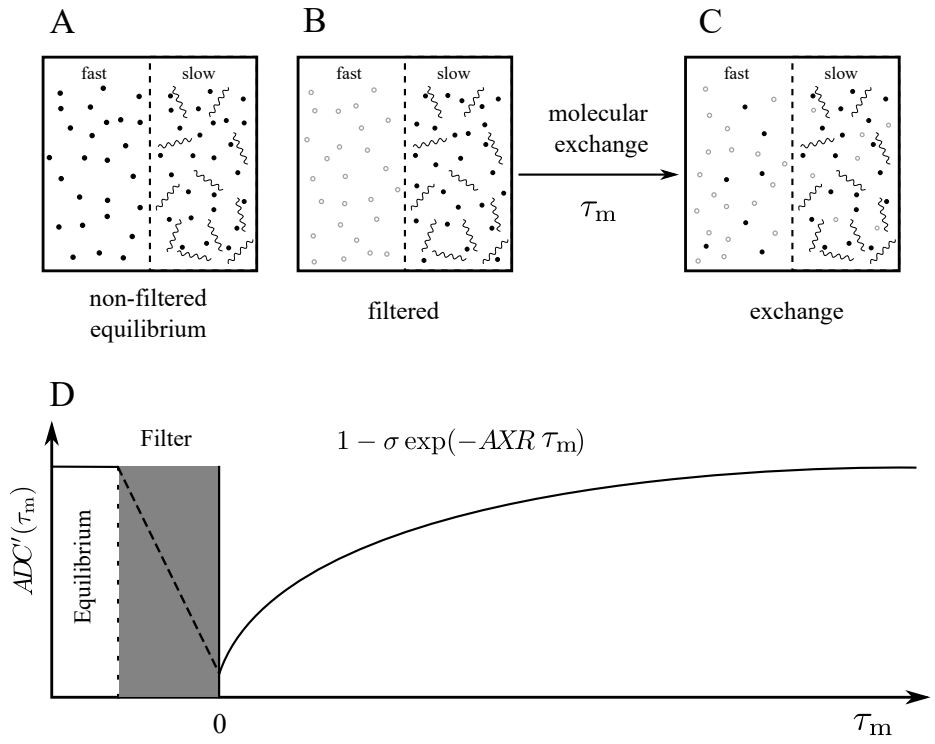

Figure 5.2: The FEXI principle for exchange estimation is described as it follow. **A)** A voxel contains two compartments, with fast and slow diffusing MR-visible spins (black dots), separated by a permeable membrane. **B)** The application of the first diffusion-weighting cancels the MR signal that arises from the fast diffusing spins. **C)** The molecular exchange occurs during τ_{m}, which allows particles to move between compartments. **D)** The apparent exchange rate (AXR) can be estimated by calculating a time-dependent $ADC'(\tau_{\mathrm{m}})$.

pores, a different angular dependence yields a $\cos(2\psi)$ signal modulation [28, 113]. This is due to the DDE's sensitivity to compartmental shape.

To relate AXR to tissue characteristics, it is generally assumed that the slow diffusion component corresponds to a restricted compartment with membrane permeability, e.g., intra-cellular (or intra-axonal) space. Meanwhile, the compartment with fast diffusing spins can be related to the extracellular space.

The problem arises due to the fact that AXR measurements occur in a large range of τ_{m} values. According to Mitra [28], at short τ_{m} the restriction effect is present independently of the compartment shape. While at long τ_{m}, the signal will contain the effects of compartment anisotropy. These two effects are present in measurements with increasing τ_{m}, affecting the AXR results.

This work aims to quantify the restriction and size effects' contribution to the AXR results. Concluding that it is possible to calculate an AXR in systems where no molecular

exchange is present. For this, computer simulations using impermeable compartment models were performed , as well as MR experiments using a water-in-oil emulsion phantom[1] [U4], where no molecular exchange is present.

5.2 Material and methods

5.2.1 Simulations

Simulations were performed using the Microstructure Imaging Sequence Simulation Toolbox (MISST) v0.93 [193, 194, 195] [2] with Matlab2015b (The MathWorks, Natick, Massachusetts, United States of America). MISST uses a 3 D extension of the matrix formalism (or multiple propagator) introduced by Callaghan [196]. Additionally, MISST has several isotropic and anisotropic compartment models available, which attempt to represent different cellular structures by assuming non-permeable membranes [193, 194, 195, 219]. In the simulations performed here, two diffusion-weighted periods, separated by a varying mixing time (τ_{m}), were applied successively. The diffusion gradients are rotated in the x-y plane.

The sequence simulation parameters were chosen to be achievable in a clinical MR system. The parameters of the filter block were: gradient duration $\delta_{\mathrm{f}} = 11$ ms, effective diffusion time $t_{\mathrm{d,f}} = 21$ ms, and $b_{\mathrm{f}} = 1300 \cdot 10^6$ s m^{-2}. The parameters for the measurement block were: $\delta = 9$ ms, $t_{\mathrm{d}} = 22$ ms, and $b_{\mathrm{m}} = 900 \cdot 10^6$ s m^{-2}, as in Lasič et al. [32]. Eighty three equally-spaced τ_{m} values between 11 and 421 ms were used to separate the diffusion periods.

This work studies the effects of size in $ADC'(\tau_{\mathrm{m}})$ and AXR by simulationing spherical compartments. The spherical compartment is intended to simulate the signal arising from glial cells in the brain or any spherical compartment.

Previously published AXR results were performed in yeast cells [32]. The size of yeast cells varies depending on species and environment. The diameter of yeast cells is usually between 3 and 4 μm. However, some species can reach diameters of 40 μm. In previous publications, baker's yeast was used [32], which appears as a spherical compartment under the microscope, with a diameter in the range of 5-10 μm [220]. Therefore, here, spherical compartments of diameters (d) 1, 5, 10, 15, 20 and 25 μm, with intrinsic diffusivity (D) of $2 \cdot 10^{-9}$ m^{2}s^{-1} were used in simulations.

Additionally, a simulation of the diffusion signal in a rat's white matter model was per-

[1] Bachelor internship Anastasia Benedik and Rabea Landmesser, 2016

[2] The package can be downloaded from https://www.nitrc.org/projects/misst

Table 5.1: Simulation parameters for rat's brain white matter (three-compartment model)

Compartment	Volume fraction	Parameter description	Value
Sphere	0.382	D_s: diffusivity inside the sphere	$802 \cdot 10^{-12}$ m^2s^{-1}
		R_s: sphere radius	2.94 μm
Cylinder	0.516	D_c: diffusivity inside the cylinder	$802 \cdot 10^{-12}$ m^2s^{-1}
		R_c: cylinder radius	8 μm
		α: angle from z-axis	1.57 rad
		β: angle from x-axis	1.57 rad
Tensor	0.101	D_{par}: parallel diffusivity	$802 \cdot 10^{-12}$ m^2s^{-1}
		D_{per1}: perpendicular diffusivity (1)	$321 \cdot 10^{-12}$ m^2s^{-1}
		D_{per2}: perpendicular diffusivity (2)	$169 \cdot 10^{-12}$ m^2s^{-1}
		α: angle from z-axis	1.57 rad
		β: azimuthal angle from x-axis	1.57 rad
		ζ: rotation angle of the tensor	2.318 rad

formed in order to investigate the diffusion signal and $ADC'(\tau_{\mathrm{m}})$ behavior in an anisotropic (tissue-like) environment. This was obtained combining three compartments in different volume fractions, as suggested by Panagiotaki et al. (Table 5 - TensorCylinderSphere A) [219]. These three compartments were: cylinder, diffusion tensor and sphere, which represented the intra-axonal space, the extracellular space and glial cells, respectively. The total diffusion signal for a three-compartment model arises from the sum of the volume fractions, f_i, where i is the number of compartments, restricted with $0 \leq f_i \leq 1$. The simulation parameters of the diffusion signal in white matter are shown in Table 5.1. In the tensor model, the parallel diffusivity, d_{par}, corresponds to the largest tensor eigenvalue and the perpendicular diffusivities (d_{per1} and d_{per2}) correspond the middle and smallest tensor eigenvalues, respectively. The $ADC'(\tau_{\mathrm{m}})$ in these simulations was calculated using Eq. 5.1. The parameters AXR and σ were then fitted to the calculated $ADC'(\tau_{\mathrm{m}})$ using Eq. 5.2. The "equilibrium ADC", or simply ADC, is reached when the simulated signal hits the plateau.

5.2.2 MR experiments

For MR experiments, a water-in-oil emulsion was used as a phantom where no molecular exchange between compartments is expected [U4]. Figures 5.3 A and B show a T_1-weighted image of the phantom. In Fig. 5.3 C, the region-of-interest ROI for analysis is overlaid on a non-diffusion weighted image acquired using the DDE-STE pulse sequence shown in Fig. 5.1. The ROI was selected in an area without visible artifacts. The water-in-

oil emulsion has a mean droplet diameter of approximately 15 μm (determined using an optical microscope). It was prepared using 79% water and 20% safflower oil, emulsifiers DMG-0295 (0.6%) and PGPR-4175 (0.4%) (Palsgaard, Juelsminde, Denmark) [U4].

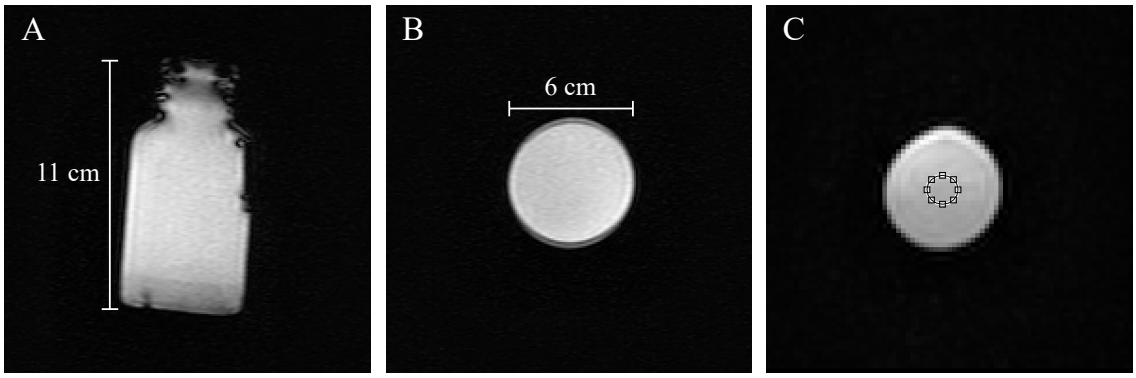

Figure 5.3: MR images of the water-in-oil emulsion. **A)** and **B)** show sagittal and coronal views in T_1-weighted TFE images. In B), it is possible to see a chemical shift artifact due to the presence of oil in the emulsion. In **C)** an non-diffusion weighted image (S_0) is seen, which was obtained using the DDE-STE pulse sequence shown in Fig. 5.1. The circle inside marks the ROI used for analysis.

DDE-measurements were performed in a clinical whole-body system operating at 3 T (Ingenia, Philips, Amsterdam), using an in-house implemented DDE-STE sequence with EPI read-out, as shown in Fig. 5.1. An 8-channel head coil was used. All the RF pulses were slice-selective. The crusher gradient pairs were applied perpendicular to the diffusion gradient pulses, differing from the previous pair by a factor of two in amplitude. Spectral Presaturation with Inversion Recovery (SPIR) [59] was used for fat suppression. In order to investigate the effect of different b-values in the $ADC'(\tau_\mathrm{m})$ and AXR estimations, two experimental protocols were performed in one slice with a field-of-view of $196 \times 196 \times 5$ mm^3 and a voxel size of $3 \times 3 \times 5$ mm^3. The experimental parameters are shown in Table 5.2. The delay between the innermost diffusion gradient pulses is modified by changing the parameter TM (time between the two inner 90° RF pulses). For each TM, one non-diffusion weighted (S_0) image and nine diffusion-weighted images were acquired. The diffusion gradients pulses were applied along $x-$, y- and z-axes in the following scheme: one with $\mathbf{G}^{(1)} = \mathbf{G}_\mathrm{f}$ and $\mathbf{G}^{(2)} = 0$, one with $\mathbf{G}^{(1)} = \mathbf{G}_\mathrm{f}$ and $\mathbf{G}^{(2)} = \mathbf{G}_{\mathrm{m}(1)}$ and one with $\mathbf{G}^{(1)} = \mathbf{G}_\mathrm{f}$ and $\mathbf{G}^{(2)} = \mathbf{G}_{\mathrm{m}(2)}$. The $x-$, y- and z-axes correspond to read-out, phase-encoding and slice-selection directions, respectively. $\mathbf{G}_\mathrm{m}$ ($\mathbf{G}^{(2)}$) are the gradient pulses in the second diffusion period (or measurement block). The amplitude of $\mathbf{G}^{(1)}$ and $\mathbf{G}^{(2)}$ are selected to reach the b-values shown in Table 5.2. The voxels inside the ROI are arithmetically averaged, which results in a single signal value per (τ_m) measurement. The $ADC'(\tau_\mathrm{m})$ was calculated from Eq. (5.1), where $S(b, \tau_\mathrm{m})$ was the re-

Table 5.2: Experimental parameters used for MR experiments.

Parameter	Protocol 1	Protocol 2
TE_1, TE_2, TR	60, 85, 2500 ms	65, 90, 2500 ms
$\delta_f = \delta$	16 ms	19.8 ms
$\Delta_f = \Delta$	30 ms	33 ms
τ_m	TM + 41.5 ms	TM + 44 ms
TM	10, 20, 30, 40, 50, 60, 80, 100, 150, 200, 250, 300, 350 and 400 ms	10, 20, 30, 40, 50, 60, 80, 100, 150, 200, 250, 300, 350 and 400 ms
b_f	$915 \cdot 10^{-6}$ s m^{-2}	$1500 \cdot 10^{-6}$ s m^{-2}
$b_{m(1)}$	$618 \cdot 10^{-6}$ s m^{-2}	$907 \cdot 10^{-6}$ s m^{-2}
$b_{m(2)}$	$915 \cdot 10^{-6}$ s m^{-2}	$1500 \cdot 10^{-6}$ s m^{-2}

sulting signal value obtained from the average inside the ROI. Equation (5.2) was fitted to estimate AXR, ADC and σ using a non-linear least squares method.

5.3 Results

5.3.1 Simulations

5.3.1.1 Sphere model

Figure 5.4 shows the signal dependence on ψ for spherical pores of diameter (d) 10, 15, 20 and 25 μm. As expected in the simulations, an increase in the signal amplitude with an increasing pore diameter was observed. This effect has already been reported by Koch and Finsterbusch [126]. With increasing τ_m the signal modulation decreases for spherical pores, as expected.

The plots shown in Fig. 5.5 display another perspective of the plots shown in Fig. 5.4. Figure 5.5 shows the diffusion signal behavior when the angle between the diffusion gradients is parallel ($\psi = 0$), perpendicular ($\psi = \pi/2$) and antiparallel ($\psi = \pi$). The "equilibrium ADC" is reached when the simulated signal hits the plateau. Figure 5.5 A shows the expected signal decay for spherical pores if $\psi = 0$ and τ_m is increased. The signal decay was more noticeable for spherical compartments with diameters larger or equal to 15 μm than for smaller compartments. Figure 5.5 B) shows that in the case of spherical compartments, the diffusion signal for $\psi = \pi/2$ was not dependent on τ_m. Figure 5.5 C shows an increase in the simulated diffusion signal in the case of $\psi = \pi/2$. This increase was observed to be larger for spheres of diameter d$\geq$ 15 μm.

The simulated $ADC'(\tau_m)$ for impermeable spheres of different diameters for $\psi = 0$ is

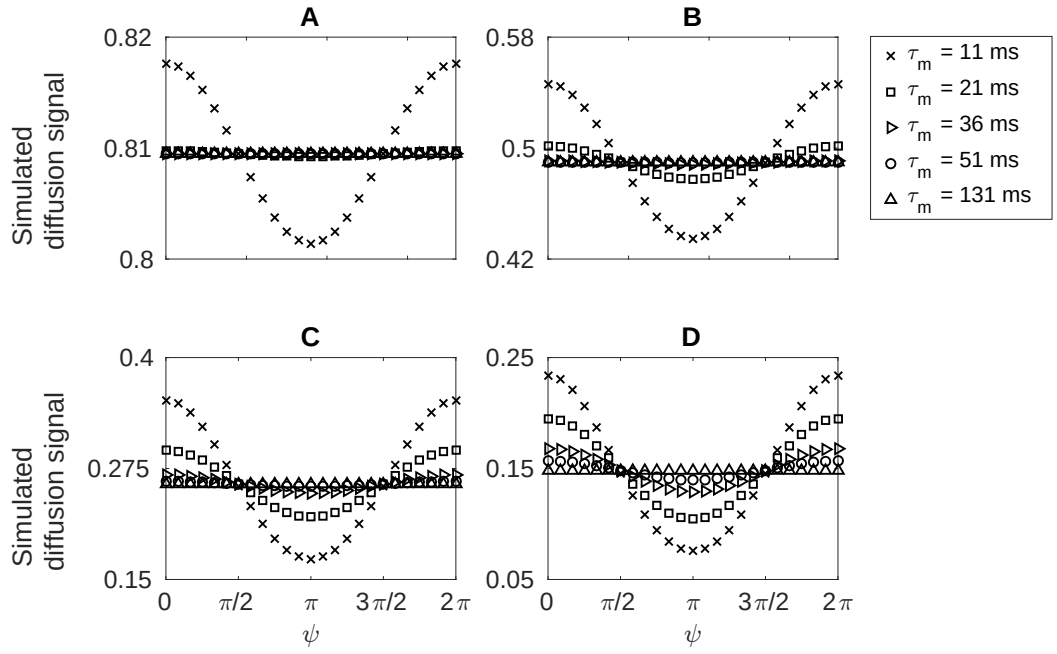

Figure 5.4: Simulated diffusion signal for spherical compartments of different diameters with increasing τ_{m}. **A)** d $= 10$ μm, **B)** d $= 15$ μm, **C)** d $= 20$ μm and **D)** d $= 25$ μm. The modulation's amplitude decreased with increasing τ_{m}.

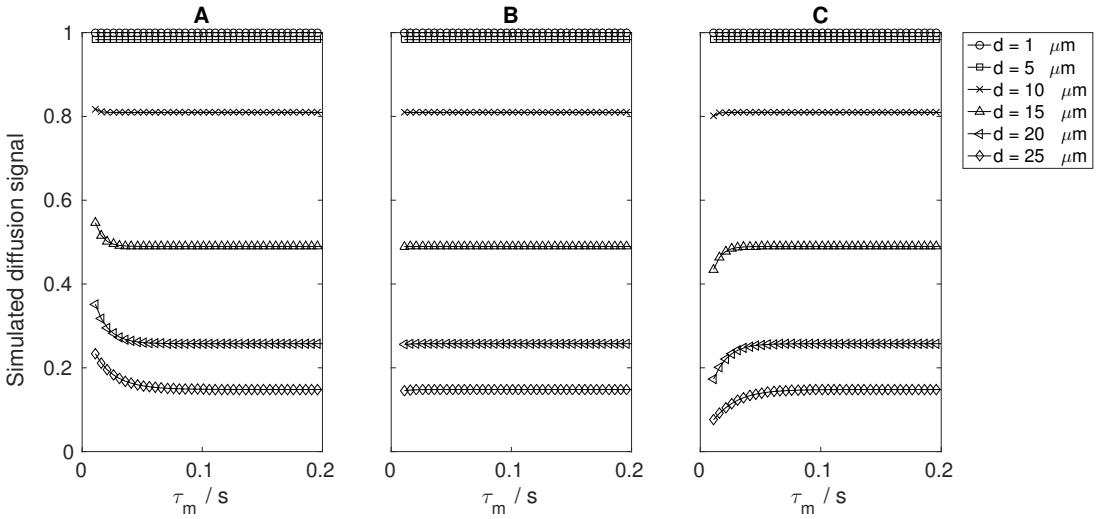

Figure 5.5: Simulated diffusion signal for a spherical model when τ_{m} is increased and the angle between the diffusion gradients is **A)** $\psi = 0$ (parallel), **B)** $\psi = \pi/2$ (perpendicular) and **C)** $\psi = \pi$ (antiparallel).

shown in Fig. 5.6. Table 5.3 displays a summary of the results. Only the parallel diffusion gradients are analyzed since this angle was used in previous publications [40, 32]. As

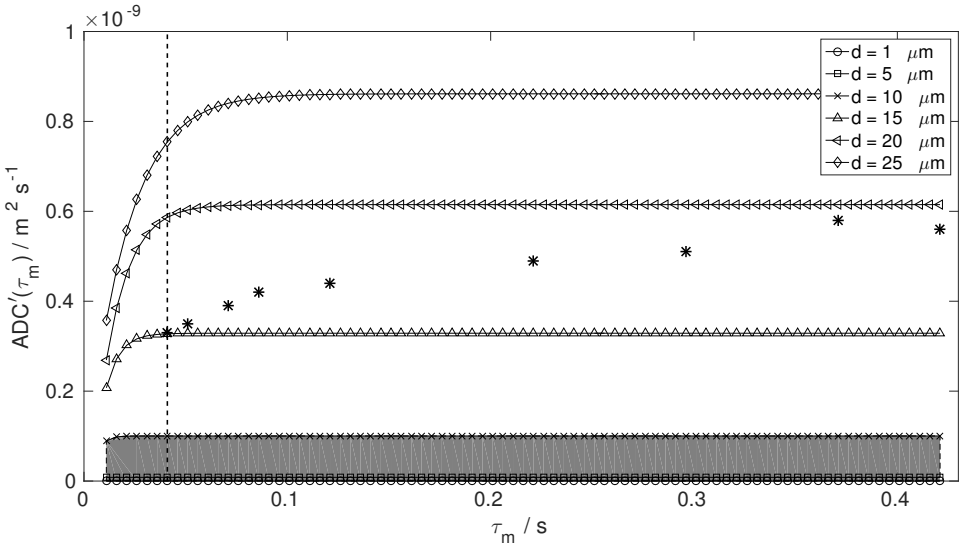

Figure 5.6: Simulated $ADC'(\tau_{\mathrm{m}})$ for spherical compartments. The applied diffusion gradients were parallel ($\psi = 0$). The black dashed line marks the minimum τ_{m} (41 ms) achievable in a DDE-STE sequence with the parameters used (accounting for δ_{f} and spoiler gradient pulses before, after and within the longitudinal storage period). The black stars show the experimental results performed in yeast from Lasič et al. [32], where permeable membranes are expected (for visual comparison). The grey background marking the low area of the plot highlights the simulated $ADC'(\tau_{\mathrm{m}})$ of spheres with diameters between 1 and 10 μm, which corresponds to expected range sizes for yeast cells [220].

expected, an increase in $ADC'(\tau_{\mathrm{m}})$ can be observed when spherical compartment are studied.

Moreover, several additional observations can be made from Fig. 5.6 and Table 5.3. 1) A size dependence on the increase in the $ADC'(\tau_{\mathrm{m}})$ is observed. For large compartments, the increase on the amplitude is slower than for smaller compartments. 2) It can be observed that when the sphere diameter is increased, the time required to reach the "equilibrium ADC" also increases. This time lies between 11 ms and 150 ms for spheres of diameter 1 and 25 μm, respectively. This may imply that the effects of restriction are present in that τ_{m} range. 3) From Table 5.3, the AXR appears to be inversely proportional to the sphere size. These three effects have not been observed in previous research. As the $ADC'(\tau_{\mathrm{m}})$ is proportional to the natural logarithm of the diffusion signal, for $\psi = \pi/2$ the $ADC'(\tau_{\mathrm{m}})$ will be constant and its value will depend on the sphere's size. For $\psi = \pi$, the $ADC'(\tau_{\mathrm{m}})$ will decrease with increasing τ_{m}.

Table 5.3: Simulation results for spherical compartments of different diameters.

Diameter (d)	τ_m when equilibrium ADC is reached	Equilibrium ADC	AXR	Contribution short τ_m	Contribution long τ_m
1 μm	11 ms	$2.6 \cdot 10^{-14}$ m^2 s^{-1}	0	0.008%	0.005%
5 μm	16 ms	$8.3 \cdot 10^{-12}$ m^2 s^{-1}	479.6 s^{-1}	2.5%	1.5%
10 μm	32 ms	$1.0 \cdot 10^{-10}$ m^2 s^{-1}	284.6 s^{-1}	3.0%	18%
15 μm	56 ms	$3.3 \cdot 10^{-10}$ m^2 s^{-1}	153.8 s^{-1}	100%	59%
20 μm	102 ms	$6.1 \cdot 10^{-10}$ m^2 s^{-1}	85.96 s^{-1}	100%	100%
25 μm	150 ms	$8.6 \cdot 10^{-10}$ m^2 s^{-1}	54.47 s^{-1}	100%	100%

5.3.1.2 Three-compartment model

Figure 5.7 shows the simulations performed on the three-compartment model. Figure 5.7 A shows the combined simulated signal of the tensor, cylinder and spherical model. A W-shaped signal dependence is observed. This is consistent with the findings described in Chapter 4, where the plane spanned by the diffusion gradients is not perpendicular to the cylinder's (and tensor's) main axis. Therefore, the cross-section consists of eccentric-shaped pores. As expected, the perpendicular diffusion gradients ($\psi = \pi/2$ and $\psi = 3\pi/2$) did not show dependency on τ_m. However, for parallel and antiparallel gradient orientations the simulated diffusion signal is dependent on τ_m, where the signal decreases for parallel wave-vectors and increases for antiparallel ones. The calculated $ADC'(\tau_m)$ is shown in Fig. 5.7 B. An increase in $ADC'(\tau_m)$ is observed with increasing τ_m. The equilibrium ADC is reached at $\tau_m \approx 201$ ms. This could mean that effect of restriction in this model is present for $\tau_m < 201$ ms. The estimated AXR was 0.042 s^{-1}.

5.3.2 MR experiments

Figure 5.8 A and C, and Fig. 5.9 A and C, show the $ADC'(\tau_m)$ calculated from Eq. (5.1), which was obtained by applying two diffusion encoding along the x- (read-out), y- (phase-encoding) and z-axes (slice-selection), from protocol 1 and protocol 2, respectively. An increase in $ADC'(\tau_m)$ can be observed for all measurements. This behavior is expected for spherical compartments if $\psi = 0$, and agrees with the simulation results from Sec. 5.3.1. Surprisingly, a difference among diffusion encoding directions was observed. In these experiments, when the diffusion gradients were applied along the x-axes, the ADC was between 10 to 20% larger than along the y- and z-axes.

Figure 5.8 B and D, and Fig. 5.9 B and D show the arithmetic mean of $ADC'(\tau_m)$ over the x-, y- and z-axes for each protocol used (circles in the plot), for protocol 1 and

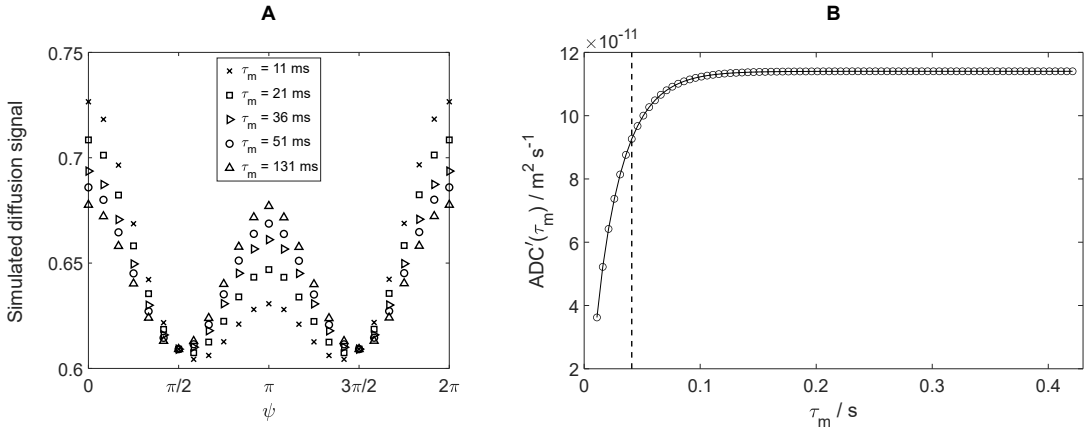

Figure 5.7: Simulated diffusion signal for the three-compartment model. **A)** Combination of the three signals in the different fractions. **B)** Simulated $ADC'(\tau_\mathrm{m})$ for three-compartment model for parallel wave-vectors ($\psi = 0$). The black dashed line marks the minimum $\tau_\mathrm{m} = 41$ ms achievable in a DDE-STE sequence for the used parameters (accounting for δ_f and spoiler gradient pulses before, after and within the longitudinal storage period). The estimated $AXR = 0.042$ s^{-1} was calculated from fitting Eq. (5.2) to the calculated $ADC'(\tau_\mathrm{m})$ from Eq. (5.1).

protocol 2, respectively. The solid line was calculated by fitting Eq. (5.2) to the averaged $ADC'(\tau_\mathrm{m})$. After calculating the arithmetic mean over perpendicular diffusion encoding, an increase in $ADC'(\tau_\mathrm{m})$ is observed in all protocols if τ_m is increased. It can be seen that the values of $ADC'(\tau_\mathrm{m})$ depend on the selected protocol, showing a decrease in value when increasing the diffusion weighting. This could indicate that the AXR is dependent on the MR acquisition parameters.

Table 5.4 shows the estimated values for ADC, σ and AXR, which were obtained from fitting Eq. (5.2) to the $ADC'(\tau_\mathrm{m})$ calculated from Eq. (5.1) (using a nonlinear least squares method). The estimated values of ADC depended on the protocol used. The filter efficiency, σ, which is controlled by the diffusion-weighting of the first diffusion block, had an approximate value 0.2, and the estimated AXR was between 10 s^{-1} and 16 s^{-1}, depending on the protocol used.

Table 5.4: Summary of results obtained from fitting Eq. (5.2) to the $ADC'(\tau_\mathrm{m})$ calculated from the experimental data.

Protocol	$ADC'(\tau_\mathrm{m})$	σ	AXR
Protocol 1 - $b_{\mathrm{m}(1)}$	$2.46 \cdot 10^{-10}$ m^2 s^{-1}	0.19	12.3 s^{-1}
Protocol 1 - $b_{\mathrm{m}(2)}$	$2.15 \cdot 10^{-10}$ m^2 s^{-1}	0.23	15.7 s^{-1}
Protocol 2 - $b_{\mathrm{m}(1)}$	$1.33 \cdot 10^{-10}$ m^2 s^{-1}	0.19	10.1 s^{-1}
Protocol 2 - $b_{\mathrm{m}(2)}$	$1.10 \cdot 10^{-10}$ m^2 s^{-1}	0.21	11.3 s^{-1}

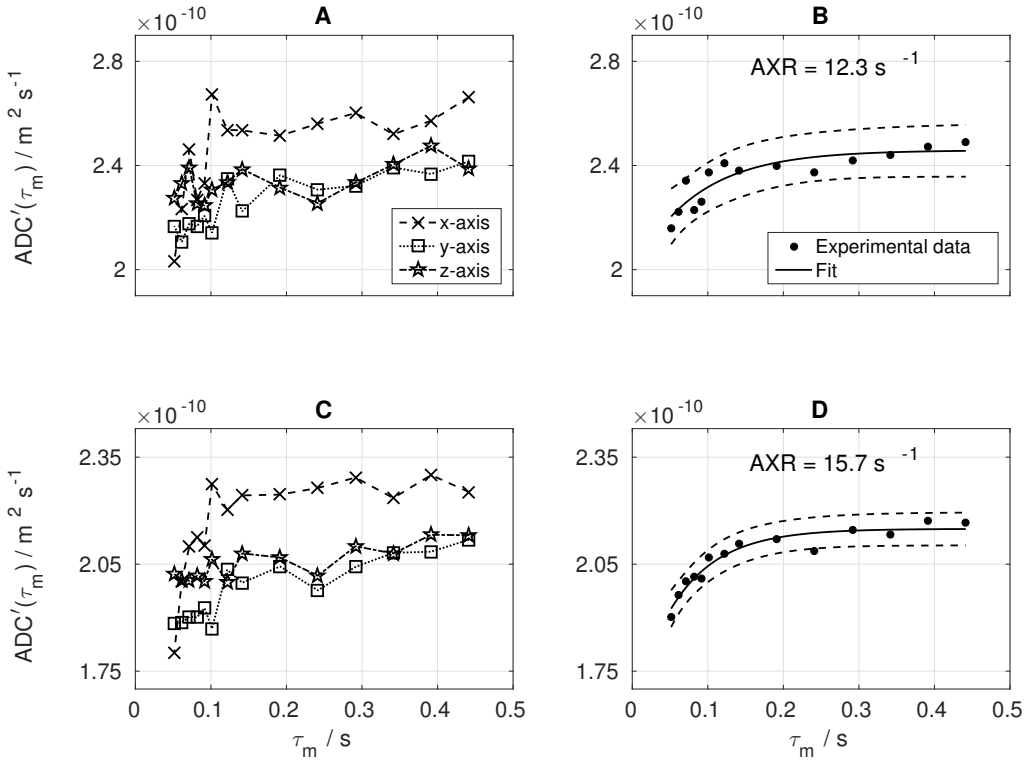

Figure 5.8: Observed $ADC'(\tau_{\mathrm{m}})$ resulting from fitting Eq. (5.1) to the experimental data obtained using Protocol 1 with $b_{\mathrm{f}} = 915 \cdot 10^6$ s m^{-2}, and **A)** $b_{\mathrm{m(1)}} = 618 \cdot 10^6$ s m^{-2}, and **C)** $b_{\mathrm{m(2)}} = 915 \cdot 10^6$ s m^{-2} in the water-in-oil emulsion. For all measurements, $\psi = 0$. In Figures A and C, crosses, squares and stars represent the $ADC'(\tau_{\mathrm{m}})$ when the diffusion gradients were applied along x- (read-out), y- (phase-encoding)- and z-axes (slice-selection), respectively. A considerable difference can be observed between the resulting data from the x-axis in comparison to the data from the y- and z-axes. In figures **B)** and **D)**, circles mark the $ADC'(\tau_{\mathrm{m}})$ obtained after the arithmetic mean of the individually calculated $ADC'(\tau_{\mathrm{m}})$ along the x-, y- and z-axes from A and C, respectively. After the average, an increase in $ADC'(\tau_{\mathrm{m}})$ is observed when increasing τ_{m}. The solid line in figures B and D shows the fit to Eq. (5.2) to the calculated $ADC'(\tau_{\mathrm{m}})$. ADC, σ and AXR were fitted to the experimental data (see Table 5.4). The dashed lines mark the confidence interval of the fitted coefficients with a certainty of 95%.

5.4 Discussion

5.4.1 Simulations

5.4.1.1 Sphere model

The objective of the simulations performed here is to study the effect of the angle between diffusion gradients on the diffusion signal and its τ_{m} dependence. Afterwards, the signal

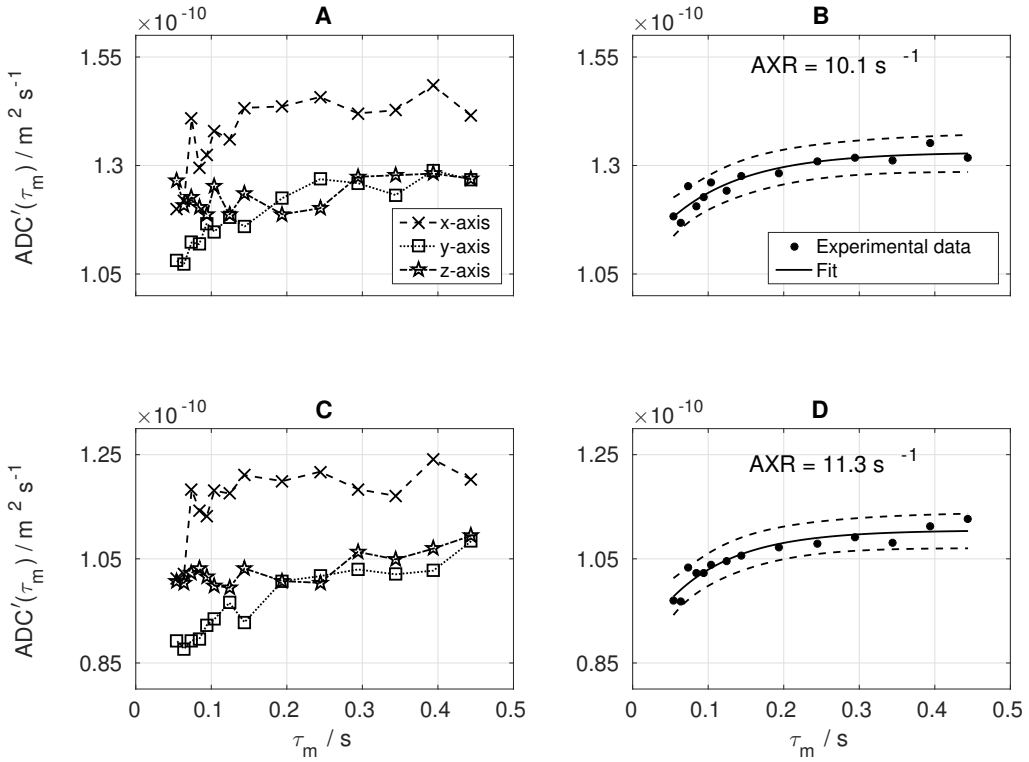

Figure 5.9: Observed $ADC'(\tau_{\mathrm{m}})$ resulting from fitting Eq. (5.1) to the experimental data obtained from Protocol 2 with $b_{\mathrm{f}} = 1500 \cdot 10^6$ s m^{-2}, and **A)** $b_{\mathrm{m(1)}} = 900 \cdot 10^6$ s m^{-2}, and **C)** $b_{\mathrm{m(2)}} = 1500 \cdot 10^6$ s m^{-2} in the water-in-oil emulsion. For all measurements, $\psi = 0$. A considerable difference can be observed between the resulting data from the x-axis in comparison to the data from the y- and z-axes. In figures **B)** and **D)**, circles mark the $ADC'(\tau_{\mathrm{m}})$ obtained after the arithmetic mean of the individually calculated $ADC'(\tau_{\mathrm{m}})$ along the x-, y- and z-axes from A and C, respectively. After the average, an increase in $ADC'(\tau_{\mathrm{m}})$ is observed when increasing τ_{m}. The solid line in figures B and D shows the fit to Eq. (5.2) to the calculated $ADC'(\tau_{\mathrm{m}})$. ADC, σ and AXR were fitted to the experimental data (see Table 5.4). The dashed lines mark the confidence interval of the fitted coefficients with a certainty of 95%.

effects in the $ADC'(\tau_{\mathrm{m}})$ when increasing τ_{m} are also investigated. Numerical simulations using non-permeable spherical compartments were performed. In Fig. 5.4, a signal modulation for spheres of different sizes is observed . The amplitude of the signal modulation depends on the size of the sphere, and scales up with increasing diameter, as expected from previous computer simulations [126] and experiments [107, 136].

The plots shown in Fig. 5.5 offer another perspective of the signal's behavior for spherical compartments. The diffusion signal is shown for parallel, perpendicular and antiparallel diffusion gradients ($\psi = 0$, $\psi = \pi/2$ and $\psi = \pi$, respectively) when τ_{m} is increased. In these plots (Fig. 5.5) it can be seen that for $\psi = 0$ there is a decrease of the diffusion

signal if τ_{m} is increased. In contrast, if the diffusion gradients are antiparallel ($\psi = \pi$), the signal increases with increasing τ_{m}. For $\psi = \pi/2$, no τ_{m} dependency is observed. These results show the importance of the angle between the wave-vectors when analyzing DDE results. Depending on the angle between the diffusion gradients, the diffusion signal will display a different behavior if τ_{m} is varied, thus affecting the calculated $ADC'(\tau_{\mathrm{m}})$ and, consecuently, the estimated AXR.

In FEXI experiments, an increase in $ADC'(\tau_{\mathrm{m}})$ is expected when τ_{m} is increased. This effect is attributed to molecular exchange between compartments [40, 32]. Based on the observation of the sequence diagrams shown in the publications, it was concluded that $\psi = 0$ was used. However, it is not clearly stated in those investigations, which was the angle between the diffusion gradients.

An increase in $ADC'(\tau_{\mathrm{m}})$ means that the diffusion signal shows an exponential decay with increasing τ_{m} (if $\psi = 0$). In the simulations performed using impermeable spheres, it is observed that an exponential decay of the diffusion signal is also present for $\psi = 0$ (Fig. 5.5 A)). It is only due to the restriction present in the sample that this effect arises, and it is not related to molecular exchange.

The $ADC'(\tau_{\mathrm{m}})$ dependence for simulated spheres on τ_{m} is shown in Fig. 5.6. The observed increase in $ADC'(\tau_{\mathrm{m}})$ is only due to restriction present in the sample, and not to membrane permeability. Moreover, in Table 5.3, it is observed that the estimated AXR may depend on the size of the compartment, which decreases with increasing size. This effect has not been reported before. The stars in Fig 5.6, which work as visual reference, correspond to the $ADC'(\tau_{\mathrm{m}})$ values published in Lasič et al. [32]. It can be clearly observed that the experimental data published by Lasič et al. [32] is well above the highlighted area, in grey. The plot's highlighted area in Fig. 5.6 marks the $ADC'(\tau_{\mathrm{m}})$ for spherical compartments with diameter between 1 and 10 μm, which is typical for yeast cells [220].

However, and due to several reasons, direct analysis and comparison between the published experimental data [32] and the simulations presented here was not possible. First, the simulation parameters are restricted to a single spherical compartment, with a known size and diffusivity inside the sphere. The yeast suspension MR measurements have many additional variables. Second, a yeast suspension in water could be considered as a two-compartment system with molecular exchange. The diffusion coefficients from intra- and extracellular space are expected to be different, and probably not the equivalent to free-diffusion at certain temperature. Therefore, the effect of temperature in the $ADC'(\tau_{\mathrm{m}})$ may need to be considered. Third, the extracellular space may also contribute to the increase in $ADC'(\tau_{\mathrm{m}})$. This is an observation from Chapter 4. If the DDE-size estimates are above the expected axonal diameter, this may be due to a signal contribution from

the extra-axonal space. In FEXI experiments, a contribution from the extracellular space may be interpreted as a larger compartment, showing a more pronounced signal decay. Therefore, a misinterpretation of the $ADC'(\tau_m)$ may occur. And fourth, the size of yeast cells in the experiments was not published.

In the study of AXR in cancer characterization for different cell lines, MCF-7 carcinoma cells with a diameter between 10 and 15 μm yielded an AXR of 5 s^{-1} [43]. Blood cells also have diameters of about 10 μm. Compared with our simulations, AXR estimations for spherical compartments in that range is 110.6 s^{-1}, only due to the effects of restriction. This means that the contribution of the restriction effect in AXR calculations in large size compartments may be significant and would need to be corrected or compensated.

5.4.1.2 Three-compartment model

Additionally, the three-compartment model that simulates a rat's brain white matter published by Panagiotaki et.al [219] was investigated using MISST. This simulated tissue model may be a more appropriate manner than a single sphere. The three-compartment model (TensorCylinderSphere) consists in a sphere and a cylinder, representing the intracellular space, which represent the intracellular space, and a tensor representing the extracellular space, without molecular exchange between compartments. The diffusion signals that arise from these compartments are then summed up in different volume fractions (Fig, 5.7). The W-shape arises from the eccentric pores in the cross-section of the tissue compartments and the plane spanned by diffusion gradients. An increase in $ADC'(\tau_m)$ was observed in Fig. 5.7. This increase reflects the presence of compartments, and it is not related to molecular exchange. Therefore, it is possible to calculate AXR from the signal decay arising exclusively from the restriction effect. The estimated AXR resulted in a much lower value than the single compartment simulations ($AXR = 0.042$ s^{-1}). Hence, the effects of restriction should be considered when studying biological tissue.

AXR values have been reported in human brain *in vivo*, with values of 1.6 ± 0.11 s^{-1}, 1.0 ± 0.12 s^{-1} in frontal and parietal white matter, and 0.8 ± 0.08 s^{-1} in the internal capsule [42]. There, the contribution of the compartmental restriction is not accounted for, and it may need to be considered in further research.

5.4.2 MR experiment

In previously published MR filter exchange imaging (FEXI) results using yeast, an increase in $ADC'(\tau_m)$ is assumed as an indicator of molecular exchange with an AXR estimate of 1.8 s^{-1} [32]. The results obtained here showed that, in the case of parallel

wave-vectors, the diffusion signal decay when increasing τ_{m} may be due to microscopic structural features of the sample, but not to molecular exchange. Here, in MR experiments, it can be observed that in a sample without molecular exchange between compartments, an increment in $ADC'(\tau_{\mathrm{m}})$ occurs when the τ_{m} increases. Therefore, it is possible to make an AXR estimation, even in the absence of molecular exchange.

The estimated AXR values in the experiments shown here are well above the previously published results for yeast [32], fixated monkey brain [46], breast cancer cells [43] and in human brain *in vivo* [42, 45]. Therefore, high values of AXR may be an indicative of low or no membrane permeability in the sample or tissue under study.

The difference between the $ADC'(\tau_{\mathrm{m}})$ calculated from the signal decay of the diffusion weighting along the read-out direction (x-axis), in comparison with y- and z-axes could be explained due to a long echo train in the EPI read-out as T_2* decay occurs during this period. The T2* decay could also be due to imperfect shimming along the x-axis. Unfortunately, acquisitions with EPI read-out are very vulnerable to artifacts. Blurring and distortion are the most dominant artifacts present in single-shot EPI [221]. Even though the acquired images did not show evident signs of blurring, they show distortion and Gibbs ringing. The image in Fig. 5.3 C shows a small distortion in the upper area of the phantom, along the phase-encoding direction (y-axis). This may be due to an air bubble inside the bottle. Gibbs ringing was observed in the outer area of the phantom. The ROI selected for the analysis of $ADC'(\tau_{\mathrm{m}})$ and AXR estimations did not show evident signs of artifacts.

The water-droplet size in the water-in-oil emulsion used for these experiments was approximately 15 μm, according to optical microscopy. A disadvantage of this phantom is that it has a broad size distribution due to an unoptimized emulsification process.

Unfortunately, previous published $FEXI$ work does not clearly state the angle between the wave-vectors. From the sequence schematic shown in those publications, it was concluded that parallel wave-vectors were used. Interestingly, in the work by Sønderby et al. [46], the sequence schematic suggested that they used antiparallel wave-vectors in accordance with the conventions from Shemesh et al. [70]. The use of antiparallel wave-vectors will result in a diffusion signal increase. This would show a decrease in $ADC'(\tau_{\mathrm{m}})$.

During this work, it was not possible to reproduce the results of the experiments performed on yeast cell suspensions by Lasič et al. [32] and Sønderby et al. [46], which could be due to hardware limitations. The MR clinical system used here has gradients up to 45 mT m^{-1}, while the ones used for the other studies had gradient systems that can provide up to 80 mT m^{-1} [32] and 400 mT m^{-1} [46] (experimental 4.7 T MR system). The

availability of high gradient strengths translates into shorter δ and Δ to reach a given b-value. This reduces the total echo time required for the experiment. The baker's yeast cells available for this study, prepared in a mixture of 2/1 (yeast/water weight ratio), had a T_2 of 39.6 ms (multi-echo acquisition) and a T_1 (multi-inversion time measurement) of 292.3 ms. Due to the short T_2, short echo times are required. Given that the echo times used here were 1.6× (i.e., 60%) larger than Lasič et al. [32] and 3.6× larger than in Sønderby et al. [46], it can be assumed that the main obstacle when reproducing the published results in yeast was the limited gradient strength and its influence on the echo time. The water-in-oil emulsion used here had longer relaxation times than the yeast sample, which makes possible to acquire DDE measurements using long echo times.

Note that the results in DDE experiments strongly depend on the parameters used, and their optimization needs to be considered. Lampinen et al. [45] proposed optimal parameters for filter exchange imaging of the human brain. These parameters are highly dependent on the sequence implementation and on the available gradient strength. In the case of the experiments presented here, the maximum available gradient strength was 45 $\mathrm{mT\,m^{-1}}$ (half of that in other AXR-FEXI studies). This hardware limitation makes it difficult to reach the suggested protocol values from Lampinen et al. [45]. Other protocol optimizations that consider clinical systems with weaker gradient strengths should be developed.

The FEXI technique has several biases to consider. Eriksson et al. [47] reported that FEXSY results are influenced by the differences in T_2 relaxation between the intra- and extracellular space, and suggested a combination of techniques (FEXSY and diffusion-relaxation correlation) to mitigate the problem. Imaging gradients such as crusher gradients pairs, in conjunction with slice-selective gradient pulses, could also influence FEXI results [222]. The imaging gradients can introduce additional diffusion-weighting, significantly harming the original MR sequence design. Therefore, those effects should also be considered [222, 223]. Sønderby et al. [46] studied for the first time the effects of microscopic anisotropy in AXR results using fixated monkey brain tissue sample. They showed that the calculated $ADC'(\tau_\mathrm{m})$ varies depending on the gradient directions, and that this effect needs to be considered in further research involving AXR estimations. Moreover, it has been observed that the AXR estimation is anisotropic even in simple compartment systems (e.g., intra- and extracellular space are eccentric compartments) [224].

In this work, an additional bias in the FEXI experiment is presented. Previously published results did not consider that an observed τ_m-dependence of $ADC'(\tau_\mathrm{m})$ could also be due to the restriction effect of the pore size in the sample under study. This issue needs to the considered and addressed in further molecular exchange research involving DDE.

5.5 Conclusions

In the brain, when the ability of the cells to control their membrane permeability interferes with normal molecular exchange, pathological conditions can occur [39, 38, 217]. Therefore, it is relevant to find new non-invasive techniques for studying membrane permeability to improve and promote the development of diagnostic tools in the clinic.

Diffusion-weighted MRI appears as a technique to study tissue microstructure and molecular exchange *in vivo*. Unfortunately, diffusion-weighted MR sequences are affected by a lack of specificity. By using DDE, it is possible to disentangle, in some degree, different effects that are distinguishable in conventional SDE sequences. However, the interpretation of the signal decay in DDE experiments needs to be carefully analyzed, given that the measured data does not exclusively contain information related to molecular exchange but is also tightly coupled with the microstructural characteristics of the sample, as observed here. Further research on this topic is required. The additional degrees of freedom of DDE, and the possible application of signal models, may provide additional tools to increase the sensitivity of this sequence to a specific characteristic [18].

In the simulations performed here, it is possible to see that for $\psi = \pi/2$ the diffusion signal is independent of τ_{m}. Therefore, the use of perpendicular wave-vectors may be more appropriate than the use of parallel wave-vector for FEXI measurements, given that for $\psi = \pi/2$ the signal appeared to be independent of restriction in the absence of exchange.

The FEXI method and the estimation of AXR have proved useful in the study of water exchange. Nevertheless, some biases need to be considered. Here, the effect of restriction and compartment size in the FEXI experiment, and their influence in the AXR estimation were investigated. From the results, it could be concluded that the effects of restriction, size and exchange are entangled in the short τ_{m} regime. For compartments with diameters up to 10 μm, the effect of restriction is present when $\tau_{\mathrm{m}} < 32$ ms. Increasing the starting τ_{m} in FEXI experiments may be a way to partially isolate the molecular exchange from the restriction and size effects. However, for compartments with diameters larger than 10 μm (like e.g., blood cells or cancer cells [43]), the effects of restriction and compartment size need to be considered and corrected for. As a preventive measure, here it is suggested to start the FEXI experiments with $\tau_{\mathrm{m}} > 100$ ms. This way, the effects of restriction would not interfere with the AXR calculations.

Alternatively, an average of results for $\psi = 0$ and $\psi = \pi$ could be used, but it would require longer acquisition times. The use of perpendicular wave-vectors may also be beneficial. Considering that biological tissues are mainly anisotropic, a good alternative,

would be the use of a multi-directional FEXI experiment to estimate an averaged AXR. This measurement was implemented in the MR experiments performed here, and for *in-vivo* experiments by Lasič et al. [43] using the average of three orthogonal directions. It is expected that the simple suggestions presented here would improve the accuracy of AXR results.

6

Conclusions and future work

6.1 Summary

It has been observed that microscopic changes in the microstructure of the brain, such as axonal diameter, may be related to e.g., abnormalities in the brain development or degeneration of white matter. As an example, studies have shown that changes in the axonal diameter are present in brain disorders such as autism spectrum disorder [225] and schizophrenia [226].

Double diffusion encoding provides a way to study size and shape of a compartment (restriction effect and microscopic anisotropy, respectively) [117, 112, 152], perfusion fraction (intra-voxel incoherent motion) [187] and membrane permeability (molecular exchange) [40, 32]. All these factors are present in the acquired data. It is difficult to design a set of gradients (or experiments) that would improve specificity to a single effect in the diffusion signal. So far, it has been inevitable to obtain results influenced, in some degree, by another measurable effect using the same technique. This thesis aims to exploit the sensitivity of DDE to the size and shape of a compartment and molecular exchange. This work studies how these microstructural characteristics affect the DDE MR signal.

In Chapter 4, the origin of the DDE signal in human CST is studied. This is because the

DDE size estimates obtained in the CST are well above the axonal diameter expected in that brain area [29]. The hypothesis presented here is that the measured signal has a high contribution from diffusion in the extra-axonal space, which may be the main origin of the DWI signal in SDE [227].

One way of inferring the origin of the DDE signal in the human CST is by using its sensitivity to microscopic anisotropy combined with its sensitivity to compartmental restriction. In the human CST, the intra-axonal space is expected to be a coherently organized bundle of fibers. Here, as a simplification, axons can be represented as coherently organized parallel cylinders that are not tightly packed, creating an eccentric space between the fibers (considered as extra-axonal space). In this scenario, if the plane spanned by the diffusion gradients is perpendicular to the cylinder's main axis, the signal arising from inside the parallel cylinders will only contribute to the DDE signal with the signature of restriction at short τ_{m} ($\cos(\psi)$). However, the DDE signal arising from the space between the fibers will exhibit the typical angular dependence of microscopic anisotropy ($\cos(2\psi)$). In these measurements, the problem arises when the diffusion gradients' plane is not perfectly perpendicular to the CST fibers.. This results in a cross-section containing eccentric compartments that correspond to the intracellular space of tilted cylinders, and will exhibit the DDE characteristic $\cos(2\phi)$ modulation arising from its microscopic anisotropy.

After calculating the geometric mean, as described in Chap. 4, the difference between parallel and perpendicular wave-vector will be an indicative of the shape of the compartment dominating the origin of the DDE signal. A positive parallel-perpendicular difference can be attributed to either (1) contributions from eccentric extracellular compartments that do not have a common orientation throughout the voxel, or (2) fiber dispersion within the voxel. However, if there is no significant difference between parallel and perpendicular wave-vectors, it reflects that the compartment dominating the DDE signal inside the voxel has low eccentricity.

The results presented here have shown that there is a positive difference between parallel and perpendicular wave-vectors in the human CST *in vivo*. This would be consistent with the notion that the DDE signal might not be dominated by the narrow intracellular axonal compartment, but rather by a wider (and eccentric) extracellular compartment.

As the structure of the CST suggests that axons are coherently organized in a fiber bundle, it is passable to conclude that the signal's origin can be the extracellular space. However, the effects of fiber dispersion cannot be simply overruled. A certain degree of fiber dispersion can be found in different white matter tracts [203, 204, 205]. However, in CST specially in fibers are expected to be more densely packed, especially within the *Capsula*

interna. Although it appears unlikely that the observed minima at perpendicular orientations arise purely from intravoxel fanning of fibers, the possibility cannot be excluded. The effects of fiber dispersion would need to be considered in future research, involving the estimation of axonal orientation distribution functions in high spatial resolution data.

This conclusion is congruent with the resolution limit of a clinical scanner reported by Nilsson et al. [211]. In the case of cylinder diameter estimation, the reported resolution limit was between 4 to 8 μm for clinical systems with a maximum gradient strength of 60 to 80 mT m^{-1}. According to that estimation, it would not be possible to estimate pores smaller than 8 μm in the experiments presented here. Considering that less than 1% of the axons in the brain have diameters larger than 3 μm [228], an alternative diffusion weighting, such as oscillating gradients, would be more appropriate to estimate compartment size [211]. However, this is out of the scope of the present work.

Chapter 5 studies the molecular exchange application of DDE. Molecular exchange across biological membranes is a highly controlled process responsible for water homeostasis inside cells [229, 230]. Water can pass through the cellular membrane directly through the bilipid layer or via water-channel proteins called aquaporins (AQPs). When the ability of the AQPs to facilitate membrane transport is affected, pathological conditions such as brain edema can occur [217, 231]. Thus, there is a need for clinical imaging techniques capable to assess water transport across cellular membranes *in vivo* [42].

In conventional diffusion-weighted MRI (SDE), the most common assumption is that slowly diffusing molecules are located within the axon, while the water located in the extracellular space will exhibit fast diffusion. Additionally, it is assumed that there is no appreciable transmembrane molecular exchange on the experiment's time scale (diffusion time) [42]. Multiple diffusion time experiments can be performed to quantify molecular exchange. Unfortunately, the effects of restriction can hinder the accuracy of this quantification, due to, for example, fiber orientation dispersion in brain tissue [232].

Double diffusion encoding was suggested and used to quantify molecular exchange [110, 40]. Lasič et al. [32] implemented an imaging version that allows the estimation of an apparent exchange rate using clinical MR scanners. As mentioned before, in DDE different effects are entangled together. Sønderby et al. [46] have studied the dependence of microscopic anisotropy in the AXR estimations. They showed that in a sample with isotropic compartments, the AXR calculations are rotationally invariant. However, in anisotropic systems (brain tissue), the AXR varies with the fibers' orientation. Additionally, due to the difference of intra- and extracellular transverse relaxation times, the influence of T_2 should also be considered to avoid measurement bias in the AXR calculation [47]

In this thesis, the influence of the restriction effect in AXR is investigated by means of

DDE. The problem arises in the τ_{m}- dependence of ADC when using parallel wave-vector. In this case, the $ADC'(\tau_{\mathrm{m}})$ is not only affected by the molecular exchange, but also by the restriction present in the tissue. Moreover, the increase in ADC as a function of τ_{m} also depends on the size of the compartments.

Here, computer simulations performed in MISST using impermeable spheres showed that the increase in $ADC'(\tau_{\mathrm{m}})$ (when using parallel diffusion gradients) depends on the compartment size. It has been found that the effects of restriction are important for compartments larger than 10 μm. Additionally, in these simulations, it has been observed that $ADC(\tau_{\mathrm{m}})$ depends on the angle between the wave-vectors. If antiparallel wave-vectors are applied, a decrease in $ADC(\tau_{\mathrm{m}})$ is observed as a result of restriction. However, perpendicular gradients do not exhibit such dependency.

Experimental DDE MR measurements (using exclusively parallel wave-vectors) in a water-in-oil emulsion with non-permeable water droplets were performed. As molecular exchange is not present in this phantom, an increase in $ADC(\tau_{\mathrm{m}})$ would not be expected. However, an increase in $ADC(\tau_{\mathrm{m}})$ has been observed and an AXR was calculated. These estimated values arise solely due to the restriction present in the sample.

From the simulations and experimental results, it could be concluded that the effects of restriction are important and need to be accounted for when studying samples, or tissues, with compartments larger than 10 μm at clinical gradient strengths. Additionally, it has been observed that the influence of restriction is present only at short τ_{m}. Therefore, to reduce the effects of restriction in τ_{m}, here it is proposed that the FEXI experiments should not consider $\tau_{\mathrm{m}} > 100$ ms in the AXR estimates. To obtain AXR estimation without influence of the restriction effect, DDE MR measurements using perpendicular wave-vectors would be preferred. This is because they are not influenced restriction nor size effects. Another way to cancel the effects of restriction could be to use the signal average between parallel and antiparallel gradient acquisitions.

6.2 Artifacts and pitfalls

Like any other MR technique, diffusion MRI is susceptible to artifacts and pitfalls. Le Bihan [162] and Jones et al. [233] provided an extensive list in diffusion MRI. Single diffusion encoding and DDE have common system-related pitfalls. Here, the focus will be directed at eddy currents (EC) and background gradients. These topics are covered below.

Due to hardware limitations in clinical systems, the magnetic field gradient strength is relatively weak. Therefore, long duration gradient pulses are used to compensate for the

lack of gradient power to reach the required b-value [162]. These gradient pulses complicate the diffusion measurement analysis in comparison with those obtained using a delta-function pulse [234]. A solution to this problem would be the use of high-performance gradient coils; however, this is not always possible.

Another source of problems are EC that arise when the amplifiers are forced to produce fast on and off switching (such as in an EPI readout) [162]. These currents generate new magnetic fields that add up with imaging and diffusion gradients, producing distorted images and ADC miscalculation, respectively. Also, magnetic susceptibility and B_0 inhomogeneities (due to poor shimming) in both the sample and its surroundings generate background gradients, which causes signal loss and geometric distortions. Many techniques have been suggested to correct for geometric distortions due to the EPI acquisition scheme [235, 236, 237]. In addition, the presence of background gradients can cause unwanted dephasing and rephasing of the spins, adding a cross-term between the background gradient and the applied diffusion gradients, which can interfere with the correct analysis of the diffusion measurements [157, 238, 239]. In the following sections, the implications that background gradient cross-terms and eddy currents have in DDE experiments will be discussed.

6.2.1 Background gradient cross-terms

Arising from the magnetic susceptibility of heterogeneous samples and magnetic field inhomogeneities [165], BGG may interfere with DDE measurements by introducing additional and unwanted diffusion-weighting. If this is not taken into consideration, it could lead to a systematic error in ADC estimations [240, 167, 241]. In DDE, the BGG cross-terms are known to induce DDE signal modulation in free diffusion samples at high magnetic fields [155]. In Chap. 3, BGG cross-terms calculations were performed in the most used DDE sequences *in vivo*. There, it was observed that the BGG cross-term depends on the angle between the wave-vectors, which was previously described by Shemesh and Cohen [155]. In addition, it was observed that under specifically timed sequence conditions, the cross-terms could be reduced or even canceled out. This can be achieved by positioning the diffusion gradient pairs before and after the refocusing pulses in a symmetric manner.

The DDE sequence used in Chap. 4 reduces the BGC in comparison with a DDE sequence with only one RF pulse [125]. If Δ is kept short, the cross-term is reduced and could be neglected. This is the *in vivo* situation, where the compartments are small, and therefore, Δ can be set to a short value. However, if the pore size is large, or if the imaging area suffers from susceptibility artifacts, then a DDE sequence that completely

suppresses the BGG cross-terms [107], or a bipolar-based approach as in Shemesh and Cohen [155], would be preferred.

BGG cross-terms in the DDE stimulated echo version used in Chap. 5 has not been studied before. It was observed that the cross-term depend on the angle between the diffusion gradients. It was also observed that when $\phi = \pi$, and the gradient pulses are symmetrically positioned before and after the refocusing pulses, then the cross-term simplified to zero. However, this is not of great relevance, given that for FEXI experiments $\psi = 0$ is used. The BGG cross-terms are known to influence the DDE measurement. However, this has not been studied in detail yet. More research in this area would be of general interest.

6.2.2 Eddy currents

Due to the motion sensitivity of diffusion MRI, it is common to perform image acquisition using echo planar imaging (EPI) [55]. However, this imaging technique is susceptible to different artifacts, such as distortion in size, shift and shear of the imaged object, which in combination with the imaging gradient pulses generate image artifacts [242, 243, 162]. The effect of eddy currents can be reduced by careful gradient coil design [244] and active shielding [245]. However, due to the fast switching of the gradient coils, eddy currents can still have a substantial effect and distort the image.

In diffusion-weighted MRI, eddy currents arise mainly from by long gradient pulses with high strength. This could result in an ADC overestimation [246]. The distortions produced by EPI readout in diffusion-weighted imaging can be corrected with image registration [247] or imaging post-processing [248, 249]. Another option is correcting for the effect of eddy currents directly in the design of the pulse sequence. The addition of "dummy" gradients to the diffusion-weighted pulse sequence have been implemented in order to reduce the effects of the induced eddy currents [250, 251]. Also, bipolar gradients (e.g. two gradient pulses of inverse polarities positioned before and after a refocusing pulse) have shown to be efficient in reducing eddy current distortions [252], as in twice-refocused spin echo (TRSE), developed by Reese et al. [253]. This technique consists on adding two pairs of bipolar gradients pulses of different duration (δ_1, δ_2, δ_3, δ_4 where $\delta_1 + \delta_2 = \delta_3 + \delta_4$), where the refocusing pulses divides each bipolar pair.

Recently, Müller et al. [254] adapted this last approach to DDE sequences using asymmetric gradient pulse duration (see Fig. 6.1). The diffusion encodings can be compensated independently using a twice-refocusing spin-echo approach [253] for each diffusion encoding individually, reducing the post-processing and the acquisition time. A disad-

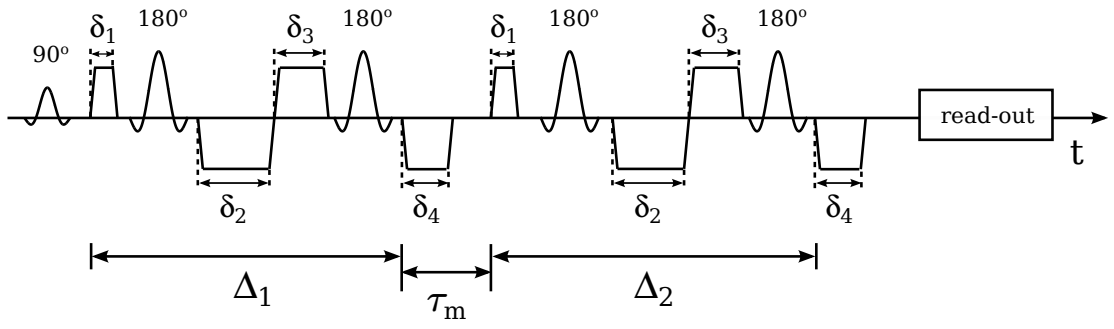

Figure 6.1: DDE sequence with eddy current compensation using twice-refocusing spin-echo scheme from Müller et al. [254]

vantage of this method is that it requires long echo times, resulting in SNR loss due to T_2 relaxation. However, eddy current compensation diminishes distortion artifacts and the total measurement times are "reduced" because multiple acquisitions (e.g., additional measurements with diffusion gradients with opposite signs) are not required.

6.3 Future work

Apart from the work presented in this thesis, some further topics and improvements will help to bring closer the primary goal of DDE: virtual histology. Diffusion MRI provides a non-invasive method to study biological tissues, avoiding biopsies and the consequences of such an invasive tissue sampling. Additionally, it provides a wide field of view in MR measurements, which usually covers a complete organ in relatively short scanning times [255]. Optimized AXR acquisitions with full brain coverage can reduce the measurement time from 45 min [42] to 15 min [45]. However, those scan times are still too long to be feasible during clinical routine (5 min approx.) [30].

It is necessary to overcome several challenges to make use of the benefits of virtual histology, such as hardware availability, pulse sequence implementation and protocol optimization for clinically compatible scan times.

6.3.1 Hardware

Physical phantoms provide a simplified model of tissue where the microstructural characteristics can be controlled and useful for testing sequences. Several materials have been used for phantom development e.g. mimicking axons fiber using glass capillaries [136], emulsions [256] or yeast cells [117] to approximate spherical cells. Yeast cells possess

the advantage of having a permeable cell wall for which the molecular exchange rate can be estimated by means of DDE [40] and cell sizes between 5 to 10 μm. These microstructure characteristics of yeast cell make their suspensions an ideal phantom for size estimations and molecular exchange. However, those suspensions have a relatively short T_2, thus requiring short TE acquisitions, which sometimes are difficult to reach. Here, a water-in-oil emulsion was presented as a simple phantom for DDE sequence testing [U4]. It contains a high water percentage, which provides high SNR without signal averaging and long T_2. This makes possible fast testing in systems with limited gradient strengths, since it does not require multiple signal averages to increase the SNR. Unfortunately, it does not provide a narrow size distribution due to an inefficient emulsification process. Further phantom development with ultrasonic emulsification would be more appropriate to create phantoms with narrower size distribution.

Long echo times may be required when high b-values are needed and the MR system has limited gradient strength, which in clinical systems is in the range of 40 to 80 mT m^{-1}. Higher magnetic field gradient strengths increase SNR by reducing TE for a specific b-value, allowing for size estimation of smaller pores [211]. The Connectom scanner [257] is equipped with gradient strengths up to 300 mT m^{-1}, and it has shown encouraging results in axon diameter estimations on patients with multiple sclerosis by using a three-compartment model in a simplified AxCaliber approach [258]. Stronger magnetic fields are beneficial to diffusion-weighted imaging and microstructure imaging, increasing SNR and spatial resolution [255].

6.3.2 Advanced pulse sequences

There are several pulse sequences used in DDE experiments. Depending on the parameter of interest, it is possible to select the most appropriate one for each situation. For example, when estimating size of compartments, having access to short mixing times is crucial. This can be achieved by using a DDE sequence with two refocusing pulses (Fig. 3.5). However, if the interest lays in the study of molecular exchange, long mixing times are required, and a stimulated echo sequence would be more appropriate. Independently of the experiment, it is important to be aware of the effects of eddy currents, background gradients and susceptibility differences [155].

As described in Sections 6.2.1 and 6.2.2, BGG cross-terms and eddy currents hamper the calculation of diffusion coefficients, and those effects need to be considered. Müller et al. [254] presented a scheme to compensate for eddy currents. However, approaches to compensate for background gradient cross-terms in the presence of eddy currents need to be developed, especially if strong gradients are available *in vivo*. Note that the ECC

scheme proposed by Müller et al. [254] is not applicable when the mixing time is zero, due to the overlapping of the inner gradients. Therefore, further work is required in order to compensate or correct for these effects, ideally in one sequence.

6.3.3 Protocol optimization

One limitation of diffusion MRI acquisition schemes is the need for several gradient directions for accurate estimation of parameters like fiber orientation in DTI, size or microscopic anisotropy estimations in DDE. Unfortunately, the times required for acquisition are relatively long, restricting its applicability in the clinical environment. In this area, further investigation is required to achieve clinically compatible scanning times. Parameters like diffusion time, echo time and gradient duration and strength, need to be carefully tailored to reach an adequate b-value without losing SNR. Additionally, optimization of the number of gradient directions and optimal sequence timings parameters (e.g. TE, TR, Δ, δ) for clinical scanners need to be implemented.

6.4 Potential applications

The potential applications for DDE and related sequences are extensive, not only in the clinical environment but also in other areas, such as porous materials [259] or polymers [260]. The MR community has shown a strong interest in the application of these techniques in biological tissue, especially in the brain. In the brain, the current applications of DDE have been for estimation of axonal size, cellular shape and membrane permeability. Therefore, the most natural extension would be its application to other organs, such as heart, liver, kidney or lungs. Recently, one exciting application, which gave very promising results, has been cancer imaging [261, 262, 263]. Additionally, imaging of the kidneys using DDE for estimation of molecular exchange could be useful to estimate their glomerular filtration rate non-invasively. This would be a new application of DDE outside the brain. However, this comes with additional challenges such as correction for breathing movement, or large areas surrounded by air in the lungs.

6.5 Conclusions

Diffusion MRI and microstructural imaging provide means for the non-invasive study of biological tissues. Double diffusion encoding is an extension of the Stejskal and Tanner sequence in which two diffusion weighting periods are applied between excitation and

acquisition. With this new sequence, it is possible to investigate microscopic anisotropy, size of compartments and molecular exchange.

This work aimed to exploit the unique sensitivity of DDE to microscopic anisotropy and axonal size estimation in the human CST *in vivo*. It was observed that complications arise when the plane in which the diffusion gradients are applied is not perpendicular to the axonal fibers. A specific averaging scheme was presented as a way to cancel the signal contribution arising from tilted axons.It could be concluded that due to the particular signature of the diffusion signal from eccentric compartments, the size estimates may represent a measurement of the extracellular space.

Additionally, this work studied the influence of the restriction effect on the apparent exchange rate during the molecular exchange. Several biases have been reported in the literature. However, the influence of the restriction effect was not studied before. Here, this effect was studied in phantoms where molecular exchange was not expected on the time scale of the experiment. During simulations and experiments, it was observed that the impact of restriction is relevant for large compartmental sizes and for short mixing times. Consequently, it was concluded that in the presence of a sample with compartments of diameters larger than 10 μm (for example, red blood cells), the effects of restriction need to be considered. Two simple strategies are suggested to compensate for this bias: limiting the minimum mixing time for AXR estimations, specific signal averaging schemes or the use of perpendicular wave-vector.

Publication list

[U1] P. Ulloa, V. Wottschel, and M. A. Koch, "Extracellular space contribution to the double wave vector diffusion-weighted signal," *Biomed. Engin. / Biomed. Tech.*, vol. 59, Suppl. 1, pp. S568, 2014.

[U2] P. Ulloa, V. Wottschel, and M. A. Koch, "Studying the extracellular contribution to the double wave vector diffusion-weighted signal," *Curr. Dir. Biomed. Engin.*, vol. 1, no. 1, pp. 240–244, 2015.

[U3] P. Ulloa, V. Wottschel, and M. A. Koch, "Investigating the extracellular contribution to the double-wave-vector diffusion-weighted signal," *Proc. Intl. Soc. Mag. Reson. Med. 23*, pp. 2786, 2015.

[U4] P. Ulloa, A. Benedik, R. Landmesser, and M. A. Koch, "Water-in-oil emulsion as a simple phantom for validation of double diffusion encoding MRI sequences," *Magn. Reson. Mater. Phys. Biol. Med. 33*, vol. 29, Suppl. 1, pp. S48–S49, 2016.

[U5] P. Ulloa, V. Methot, and M. A. Koch, "Bias in the apparent exchange rate measurements: insight from numerical simulations," *Proc. Intl. Soc. Mag. Reson. Med. 25*, pp. 1085. 2017.

[U6] P. Ulloa, V. Methot, and M. A. Koch, "Experimental validation of a bias in apparent exchange rate measurements," *Curr. Dir. Biomed. Engin.*, vol. 3, no. 2, pp. 529–532, 2017.

[U7] P. Ulloa, V. Methot, and M. A. Koch, "Experimental study of bias in apparent exchange rate measurements," *Magn. Reson. Mater. Phys. Biol. Med. 34*, vol. 30, Suppl. 1, pp. S173–S174, 2017.

[U8] M. A. Koch and P. Ulloa, "Determination of the pore size distribution by double diffusion encoding," *Front. Phys.*, p. 12, 2016.

[U9] V. Methot, P. Ulloa, and M. A. Koch, “Pore size estimation using the mixing time dependence of a double diffusion encoding experiment: experimental validation on a clinical MR system,” *Proc. Intl. Soc. Mag. Reson. Med. 25*, p. 717, 2017.

[U10] V. Methot, P. Ulloa, and M. A. Koch, “Varying the mixing time of the double diffusion experiment: A better experimental design for pore size estimation,” *Magn. Reson. Mater. Phys. Biol. Med. 33*, vol. 30, Suppl. 1, pp. S633–S634, 2017.

[U11] V. Methot, P. Ulloa, and M. A. Koch, “Pore size estimation from double diffusion encoding,” *Curr. Dir. Biomed. Engin.*, vol. 30, no. 2, pp. 627–630, 2017.

[U12] P. Ulloa, A. Reiber, L. Quest, N. Kirschke, M. Sieren, A. M. Stroth, H. Kooijman-Kurfürst, J. Barkhausen, A. Frydrychowicz and T. H. Oechtering, “ Validation of accelerated 4D-flow MRI: SENSE vs. compressed SENSE 4D-flow sequences (preliminary results),” *Ger. Chapter Intl. Soc. Mag. Reson. Med.*, 2019.

[U13] P. Gurumurthy, C. Hagen, P. Ulloa, V. Methot, T. H. Oechtering, A. Frydrychowicz, M. A. Koch, and T. M. Buzug, “Time-resolved, 3-dimensional, 3-directionally velocity sensitive phase-contrast MRI for the investigation of flow patterns in a human pharynx phantom during obstructive sleep apnea,” *Magn. Reson. Mater. Phys. Biol. Med. 34*, vol. 30, p. S23, 2017.

[U14] P. Gurumurthy, P. Ulloa, C. Kluck, T. M. Buzug, and M. A. Koch, “Study of fluid flow patterns in a human pharynx phantom using phase contrast-MRI,” *Magn. Reson. Mater. Phys. Biol. Med. 33*, vol. 29, Suppl. 1, pp. S201–S202, 2016.

[U15] P. Gurumurthy, C. Hagen, P. Ulloa, M. A. Koch, and T. M. Buzug, “Computational fluid dynamics simulations and phase contrast-MRI validation of airflow in human pharynx during obstructive sleep apnea,” *Biomed. Eng. / Biomed. Tech.*, vol. 62, Suppl. 1, p. S507, 2017.

[U16] P. Gurumurthy, P. Ulloa, C. Kluck, T. M. Buzug, and M. A. Koch, “Investigation of pharyngeal flow patterns using phase contrast-MRI,” *Biomed. Engin. / Biomed. Tech.*, vol. 61, Suppl. 1, p. S227, 2016.

[U17] L. Quest, N. Kirschke, P. Ulloa, A. Reiber, M. Sieren, S. A, N. Jin, J. Graessner, H. Kooijman, J. Barkhausen, A. Frydrychowicz, and T. Oechtering, "Biologische und technische Variabilität von 4D Fluss MRT gesunder Probanden im zirkadianen Vergleich und an Scannern verschiedener Hersteller," *RöFo – Fortschr. Geb. Röntgenstrahlen bildgeb. Verfahr.*, 2020.

[U18] A. Reiber, P. Ulloa, L. Quest, A. Stroth, M. Sieren, N. Kirschke, J. Jin, N; Graessner, H. Kooijman, J. Barkhausen, A. Frydrychowicz, and T. Oechtering, "Validierung von Compressed Sensing beschleunigten 4D Fluss MRT Sequenzen an Scannern unterschiedlicher Hersteller im Vergleich zu konventioneller paralleler Bildgebung," *RöFo – Fortschr. Geb. Röntgenstrahlen bildgeb. Verfahr.*, 2020.

[U19] A. Stroth, A. Reiber, L. Quest, N. Kirschke, M. Sieren, J. Barkhausen, A. Frydrychowicz, T. Oechtering, P. Ulloa, J. Graessner, N. Jin, and H. Kooijmann, "4D Fluss MRT – Messung der aortalen Wandschubspannung: Crossover Analyse zirkadianer Unterschiede, unterschiedlicher Scanner und Beschleunigungsmethoden," *RöFo – Fortschr. Geb. Röntgenstrahlen bildgeb. Verfahr.*, 2020.

[U20] G. Bringout, J. Löfberg, P. Ulloa, M. A. Koch, and T. M. Buzug, "Designing coils to minimize the maximal induced electrical field amplitude in a patient," *Int. Workshop Magn. Part. Imaging*, p. 32, 2016.

[U21] S. Chabert, M. Villalobos, P. Ulloa, R. Salas, C. Tejos, S. San Martin, and J. Pereda, "Quantitative description of the morphology and ossification center in the axial skeleton of 20-week gestation formalin-fixed human fetuses using magnetic resonance images," *Prenat. Diagn.*, vol. 32, no. 3, pp. 252–258, 2012.

[U22] M. Cyris, M. González Lagunilla, P. Ulloa Almendras, and T. C. Schmidt, "Gadolinium-based diagnostics in water treatment," *Wasser*, 2012.

[U23] E. Peschke, P. Ulloa, O. Jansen, and J. B. Hoevener, "Metallic implants in MRI – Hazards and imaging artifacts," *RöFo – Fortschr. Geb. Röntgenstrahlen bildgeb. Verfahr.* (in press), 2021.

Bibliography

[1] M. E. Moseley, Y. Cohen, J. Mintorovitch, L. Chileuitt, H. Shimizu, J. Kucharczyk, M. F. Wendland, and P. R. Weinstein, "Early detection of regional cerebral ischemia in cats: Comparison of diffusion- and T2-weighted MRI and spectroscopy," *Magn. Reson. Med.*, vol. 14, pp. 330–346, 1990.

[2] E. L. Hahn, "Spin echoes," *Phys. Rev.*, vol. 80, pp. 580–594, 1950.

[3] E. O. Stejskal and J. E. Tanner, "Spin diffusion measurements: Spin echoes in the presence of a time-dependent field gradient," *J. Chem. Phys.*, vol. 42, pp. 288–292, 1965.

[4] K.-O. Lövblad, H.-J. Laubach, A. E. Baird, F. Curtin, G. Schlaug, R. R. Edelman, and S. Warach, "Clinical experience with diffusion-weighted MR in patients with acute stroke," *Am. J. Neuroradiol.*, vol. 19, pp. 1061–1066, 1998.

[5] Q. Yang, B. M. Tress, P. A. Barber, P. M. Desmond, D. G. Darby, R. P. Gerraty, T. Li, and S. M. Davis, "Serial study of apparent diffusion coefficient and anisotropy in patients with acute stroke," *Stroke*, vol. 30, pp. 2382–2390, 1999.

[6] G. Thomalla, B. Cheng, M. Ebinger, Q. Hao, T. Tourdias, O. Wu, J. S. Kim, L. Breuer, O. C. Singer, S. Warach, S. Christensen, A. Treszl, N. D. Forkert, I. Galinovic, M. Rosenkranz, T. Engelhorn, M. Köhrmann, M. Endres, D.-W. Kang, V. Dousset, A. G. Sorensen, D. S. Liebeskind, J. B. Fiebach, J. Fiehler, and C. Gerloff, "DWI-FLAIR mismatch for the identification of patients with acute ischaemic stroke within 4–5 h of symptom onset (PRE-FLAIR): a multicentre observational study," *Lancet Neurol.*, vol. 10, no. 11, pp. 978–986, 2011.

[7] R. N. Al-Okaili, J. Krejza, S. Wang, J. H. Woo, and E. R. Melhem, "Advanced MR imaging techniques in the diagnosis of intraaxial brain tumors in adults," *Radiographics*, vol. 26, no. Suppl. 1, pp. S173–S189, 2006.

[8] S. Lu, D. Ahn, G. Johnson, M. Law, D. Zagzag, and R. I. Grossman, "Diffusion-tensor MR imaging of intracranial neoplasia and associated peritumoral edema: introduction of the tumor infiltration index," *Radiology*, vol. 232, pp. 221–228, 2004.

[9] P. J. Basser, J. Mattiello, and D. LeBihan, "Estimation of the effective self-diffusion tensor from the NMR spin echo," *J. Magn. Reson. B*, vol. 103, pp. 247–254, 1994.

[10] S. Mori, B. J. Crain, V. P. Chacko, and P. C. M. van Zijl, "Three-dimensional tracking of axonal projections in the brain by magnetic resonance imaging," *Ann. Neurol.*, vol. 45, pp. 265–269, 1999.

[11] P. J. Basser, S. Pajevic, C. Pierpaoli, J. Duda, and A. Aldroubi, "In vivo fiber tractography using DT-MRI data," *Magn. Reson. Med.*, vol. 44, pp. 625–632, 2000.

[12] K. D. Harkins, J.-P. Galons, T. W. Secomb, and T. P. Trouard, "Assessment of the effects of cellular tissue properties on ADC measurements by numerical simulation of water diffusion," *Magn. Reson. Med.*, vol. 62, no. 6, pp. 1414–1422, 2009.

[13] J. Pfeuffer, W. Dreher, E. Sykova, and D. Leibfritz, "Water signal attenuation in diffusion-weighted 1H NMR experiments during cerebral ischemia: influence of intracellular restrictions, extracellular tortuosity, and exchange," *Magn. Reson. Imaging*, vol. 16, no. 9, pp. 1023–1032, 1998.

[14] Y. Assaf and Y. Cohen, "Non-mono-exponential attenuation of water and n-acetyl aspartate signals due to diffusion in brain tissue," *J. Magn. Reson.*, vol. 131, no. 1, pp. 69–85, 1998.

[15] Y. Cohen and Y. Assaf, "High b-value q-space analyzed diffusion-weighted MRS and MRI in neuronal tissues - a technical review," *NMR Biomed.*, vol. 15, no. 7-8, pp. 516–542, 2002.

[16] D. Le Bihan, J. F. Mangin, C. Poupon, C. A. Clark, S. Pappata, N. Molko, and H. Chabriat, "Diffusion tensor imaging: concepts and applications," *J. Magn. Reson. Imaging*, vol. 13, no. 4, pp. 534–546, 2001.

[17] N. Shemesh, E. Özarslan, M. E. Komlosh, P. J. Basser, and Y. Cohen, "From single-pulsed field gradient to double-pulsed field gradient MR: gleaning new microstructural information and developing new forms of contrast in MRI," *NMR Biomed.*, vol. 23, pp. 757–780, 2010.

[18] D. S. Novikov, V. G. Kiselev, and S. N. Jespersen, "On modeling," *Magn. Reson. Med.*, vol. 79, no. 6, pp. 3172–3193, 2018.

[19] B. Lampinen, F. Szczepankiewicz, J. Martensson, D. van Westen, P. C. Sundgren, and M. Nilsson, "Neurite density imaging versus imaging of microscopic anisotropy in diffusion MRI: A model comparison using spherical tensor encoding," *NeuroImage*, vol. 147, pp. 517–531, 2017.

[20] B. Lampinen, F. Szczepankiewicz, M. Novén, D. van Westen, O. Hansson, E. Englund, J. Mårtensson, C.-F. Westin, and M. Nilsson, "Searching for the neurite density with diffusion MRI: Challenges for biophysical modeling," *Hum. Brain Mapp.*, vol. 40, no. 8, pp. 2529–2545, 2019.

[21] D. S. Novikov, J. Veraart, I. O. Jelescu, and E. Fieremans, "Rotationally-invariant mapping of scalar and orientational metrics of neuronal microstructure with diffusion MRI," *NeuroImage*, vol. 174, pp. 518–538, 2018.

[22] F. O. Stephens and K. R. Aigner, *Basics of Oncology*. Springer, 2009.

[23] L. He, L. R. Long, S. Antani, and G. R. Thoma, "Histology image analysis for carcinoma detection and grading," *Comput. Methods Programs Biomed.*, vol. 107, no. 3, pp. 538–556, 2012.

[24] A. Fritz, C. Percy, A. Jack, K. Shanmugaratnam, L. Sobin, D. M. Parkin, and S. Whelan, *International classification of diseases for oncology*, 3rd ed. World Health Organization, 2013.

[25] C. Mannelli, "Tissue vs liquid biopsies for cancer detection: Ethical issues," *J. Bioeth. Inq.*, vol. 16, pp. 551–557, 2019.

[26] S. M. Esagian, G. . Grigoriadou, I. P. Nikas, V. Boikou, P. M. Sadow, J.-K. Won, and K. P. Economopoulos, "Comparison of liquid-based to tissue-based biopsy analysis by targeted next generation sequencing in advanced non-small cell lung cancer: a comprehensive systematic review," *J. Cancer Res. Clin. Oncol.*, vol. 146, pp. 2051–2066, 2020.

[27] D. G. Cory, A. N. Garroway, and J. B. Miller, "Applications of spin transport as a probe of local geometry," *Polym. Preprints*, vol. 31, pp. 149–150, 1990.

[28] P. P. Mitra, "Multiple wave-vector extensions of the NMR pulsed-field-gradient spin-echo diffusion measurement," *Phys. Rev. B*, vol. 51, pp. 15 074–15 078, 1995.

[29] M. A. Koch and J. Finsterbusch, "Towards compartment size estimation in vivo based on double wave vector diffusion weighting," *NMR Biomed.*, vol. 24, no. 10, pp. 1422–1432, 2011.

[30] G. Yang, Q. Tian, C. Leuze, M. Wintermark, and J. A. McNab, "Double diffusion encoding MRI for the clinic," *Magn. Reson. Med.*, vol. 80, pp. 507–520, 2018.

[31] G. Duchêne, J. Abarca-Quinones, I. Leclercq, T. Duprez, and F. Peeters, "Insights into tissue microstructure using a double diffusion encoding sequence on a clinical scanner: Validation and application to experimental tumor models," *Magn. Reson. Med.*, vol. 83, no. 4, pp. 1263–1276, 2020.

[32] S. Lasič, M. Nilsson, J. Lätt, F. Ståhlberg, and D. Topgaard, "Apparent exchange rate mapping with diffusion MRI," *Magn. Reson. Med.*, vol. 66, pp. 356–365, 2011.

[33] N. J. Yang and M. J. Hinner, *Getting Across the Cell Membrane: An Overview for Small Molecules, Peptides, and Proteins*. New York: Springer New York, 2015, pp. 29–53.

[34] A. Finkelstein, "Water and nonelectrolyte permeability of lipid bilayer membranes," *J. Gen. Physiol.*, vol. 68, pp. 127–135, 1976.

[35] P. Agre, L. King, M. Yasui, W. Guggino, O. Ottersen, Y. Fujiyoshi, A. Engel, and S. Nielsen, "Aquaporin water channels - from atomic structure to clinical medicine," *J. Physiol.*, vol. 542, pp. 3–16, 2002.

[36] A. Verkman, "Aquaporins in clinical medicine," *Annu. Rev. Med.*, vol. 63, no. 1, pp. 303–316, 2012.

[37] A. Verkman, "Dissecting the roles of aquaporins in renal pathophysiology using transgenic mice," *Semin. Nephrol.*, vol. 28, no. 3, pp. 217–226, 2008.

[38] M. C. Papadopoulos, G. T. Manley, S. Krishna, and A. S. Verkman, "Aquaporin-4 facilitates reabsorption of excess fluid in vasogenic brain edema," *FASEB J.*, vol. 18, no. 11, pp. 1291–1293, 2004.

[39] J. Hu and A. Verkman, "Increased migration and metastatic potential of tumor cells expressing aquaporin water channels," *FASEB J.*, vol. 20, pp. 1892–1894, 2006.

[40] I. Åslund, A. Nowacka, M. Nilsson, and D. Topgaard, "Filter-exchange PGSE NMR determination of cell membrane permeability," *J. Magn. Reson.*, vol. 200, pp. 291–295, 2009.

[41] X. Tian, H. Li, X. Jiang, J. Xie, J. C. Gore, and J. Xu, "Evaluation and comparison of diffusion MR methods for measuring apparent transcytolemmal water exchange rate constant," *J Magn. Reson.*, vol. 275, pp. 29–37, 2017.

[42] M. Nilsson, J. Lätt, D. van Westen, S. Brockstedt, S. Lasič, F. Ståhlberg, and D. Topgaard, "Noninvasive mapping of water diffusional exchange in the human brain using filter-exchange imaging," *Magn. Reson. Med.*, vol. 69, pp. 1572–1580, 2013.

[43] S. Lasič, S. Oredsson, S. C. Partridge, L. H. Saal, D. Topgaard, M. Nilsson, and K. Bryskhe, "Apparent exchange rate for breast cancer characterization," *NMR Biomed.*, vol. 29, no. 5, pp. 631–639, 2016.

[44] F. Schilling, S. Ros, D.-E. Hu, P. D'Santos, S. McGuire, R. Mair, A. J. Wright, E. Mannion, R. J. M. Franklin, A. A. Neves, and K. M. Brindle, "MRI measurements of reporter-mediated increases in transmembrane water exchange enable detection of a gene reporter," *Nat. Biotechnol.*, vol. 35, no. 1, pp. 75–80, 2017.

[45] B. Lampinen, F. Szczepankiewicz, D. van Westen, E. Englund, P. C. Sundgren, J. Lätt, F. Ståhlberg, and M. Nilsson, "Optimal experimental design for filter exchange imaging: Apparent exchange rate measurements in the healthy brain and in intracranial tumors," *Magn. Reson. Med.*, vol. 77, no. 3, pp. 1104–1114, 2017.

[46] C. K. Sønderby, H. M. Lundell, L. V. Søgaard, and T. B. Dyrby, "Apparent exchange rate imaging in anisotropic systems," *Magn. Reson. Med.*, vol. 72, no. 3, pp. 756–762, 2014.

[47] S. Eriksson, K. Elbing, O. Söderman, K. Lindkvist-Petersson, D. Topgaard, and S. Lasič, "NMR quantification of diffusional exchange in cell suspensions with relaxation rate differences between intra and extracellular compartments," *PLOS ONE*, vol. 12, no. 5, pp. 1–18, 2017.

[48] H. H. Mitchell, T. S. Hamilton, F. R. Steggerda, and H. W. Bean, "The chemical composition of the adult human body and its bearing on the biochemistry of growth," *J. Biol. Chem.*, vol. 168, pp. 625–637, 1945.

[49] L. G. Hanson, "Is quantum mechanics necessary for understanding magnetic resonance?" *Concepts Magn. Reson. Part A*, vol. 32A, no. 5, pp. 329–340, 2008.

[50] F. Bloch, W. W. Hansen, and M. Packard, "Nuclear induction," *Phys. Rev.*, vol. 69, p. 127, 1946.

[51] F. Bloch, "Nuclear induction," *Phys. Rev.*, vol. 70, pp. 460–474, 1946.

[52] Z. Liang and P. Lauterbur, *Principles of magnetic resonance imaging: A signal processing perspective*, ser. IEEE Press series in biomedical engineering. New york: SPIE Optical Engineering Press, 2000.

[53] M. A. Bernstein, K. F. King, and X. J. Zhou, *Handbook of MRI Pulse Sequences*. Amsterdam Boston: Academic Press, 2004.

[54] Y. Zhu, S. Gao, L. Cheng, and S. Bao, "Review: K-space trajectory development," in *2013 IEEE International Conference on Medical Imaging Physics and Engineering*, 2013, pp. 356–360.

[55] P. Mansfield, "Multi-planar image formation using NMR spin echoes," *J. Phys. C*, vol. 10, pp. L55–L58, 1977.

[56] R. J. Ordidge, P. Mansfield, and R. E. Coupland, "Rapid biomedical imaging by NMR," *Br. J. Radiol.*, vol. 54, no. 646, pp. 850–855, 1981.

[57] A. M. Howseman, M. K. Stehling, B. Chapman, R. Coxon, R. Turner, R. J. Ordidge, M. G. Cawley, P. Glover, P. Mansfield, and R. E. Coupland, "Improvements in snap-shot nuclear magnetic resonance imaging," *Br. J. Radiol.*, vol. 61, pp. 822–828, 1988.

[58] G. Johnson and J. M. S. Hutchison, "The limitations of NMR recalled-echo imaging techniques," *J. Magn. Reson.*, vol. 63, pp. 14–30, 1985.

[59] E. Kaldoudi, S. C. Williams, G. J. Barker, and P. S. Tofts, "A chemical shift selective inversion recovery sequence for fat-suppressed MRI: Theory and experimental validation," *Magn. Reson. Imaging*, vol. 11, no. 3, pp. 341–355, 1993.

[60] R. Brown, "XXVII. A brief account of microscopical observations made in the months of June, July and August 1827, on the particles contained in the pollen of plants; and on the general existence of active molecules in organic and inorganic bodies," *Philos. Mag.*, vol. 4, no. 21, pp. 161–173, 1828.

[61] A. Fick, "Ueber Diffusion," *Ann. Phys. Chem.*, vol. 170, pp. 59–86, 1855.

[62] J. Crank, *The Mathematics of diffusion*, 2nd ed. Oxford: Clarendon Press, 1975.

[63] H. C. Torrey, "Bloch equations with diffusion terms," *Phys. Rev.*, vol. 104, pp. 563–565, 1956.

[64] E. O. Stejskal, "Use of spin echoes in a pulsed magnetic-field gradient to study anisotropic, restricted diffusion and flow," *J. Chem. Phys.*, vol. 43, pp. 3597–3603, 1965.

[65] A. Einstein, "Über die von der molekularkinetischen Theorie der Wärme geforderte Bewegung von in ruhenden Flüssigkeiten suspendierten Teilchen," *Ann. Phy. Chem.*, vol. 17, pp. 549–560, 1905.

[66] J. Kärger and W. Heink, "The propagator representation of molecular transport in microporous crystallites," *J. Magn. Reson.*, vol. 51, pp. 1–7, 1983.

[67] W. S. Price, "Pulsed-field gradient nuclear magnetic resonance as a tool for studying translational diffusion: Part I. Basic theory," *Concepts Magn. Reson.*, vol. 9, pp. 299–336, 1997.

[68] D. E. Woessner, "NMR spin-echo self-diffusion measurements on fluids undergoing restricted diffusion," *J. Phys. Chem*, vol. 67, no. 6, pp. 1365–1367, 1963.

[69] P. J. Basser, J. Mattiello, and D. LeBihan, "MR diffusion tensor spectroscopy and imaging," *Biophys. J.*, vol. 66, pp. 259–267, 1994.

[70] N. Shemesh, S. N. Jespersen, D. C. Alexander, Y. Cohen, I. Drobnjak, T. B. Dyrby, J. Finsterbusch, M. A. Koch, T. Kuder, F. Laun, , M. Lawrenz, H. Lundell, P. P. Mitra, M. Nilsson, E. Özarslan, D. Topgaard, and C.-F. Westin, "Conventions and nomenclature for double diffusion encoding NMR and MRI," *Magn. Reson. Med.*, vol. 75, no. 1, pp. 82–87, Sep 2015.

[71] R. Forghani and P. W. Schaefer, *Functional Neuroradiology: Principles and Clinical Applications*. New York: Springer, 2012.

[72] D. Le Bihan and E. Breton, "Imagerie de diffusion in-vivo par résonance magnétique nucléaire," *C. R. Acad. Sci.*, vol. 93, no. 5, pp. 27–34, 1985.

[73] D. Le Bihan, E. Breton, D. Lallemand, P. Grenier, E. Cabanis, and M. Laval-Jeantet, "MR imaging of intravoxel incoherent motions: application to diffusion and perfusion in neurologic disorders," *Radiology*, vol. 161(2), pp. 401–407, 1986.

[74] D. Le Bihan, "Molecular diffusion nuclear magnetic resonance imaging," *Magn. Reson. Q*, vol. 7, pp. 1–30, 2 1991.

[75] P. Sen, "Time-dependent diffusion coefficient as a probe of geometry," *Concepts Magn. Reson. A*, vol. 23A, pp. 1–21, 2004.

[76] M. Doran, J. V. Hajnal, N. Van Bruggen, M. D. King, I. R. Young, and G. M. Bydder, "Normal and abnormal white matter tracts shown by MR imaging using directional diffusion weighted sequences," *J. Comput. Assist. Tomogr.*, vol. 14, pp. 865–873, 1990.

[77] T. L. Chenevert, J. A. Brunberg, and J. G. Pipe, "Anisotropic diffusion in human white matter: Demonstration with MR techniques in vivo," *Radiology*, vol. 177, pp. 401–405, 1990.

[78] H. Johansen-Berg and T. E. Behrens, *Diffusion MRI: From Quantitative Measurement to In vivo Neuroanatomy*, 2nd ed. London: Academic press, Elsevier, 2014.

[79] D. K. Jones and P. J. Basser, "'Squashing peanuts and smashing pumpkins': How noise distorts diffusion-weighted MR data," *Magn. Reson. Med.*, vol. 52, pp. 979–993, 2004.

[80] D. C. Alexander and G. J. Barker, "Optimal imaging parameters for fiber-orientation estimation in diffusion MRI," *NeuroImage*, vol. 27, no. 2, pp. 357–367, 2005.

[81] J. Kärger, H. Pfeifer, and W. Heink, "Principles and application of self-diffusion measurements by nuclear magnetic resonance," in *Advances in Magnetic and Optical Resonance*, J. S. Waugh, Ed. Academic Press, 1988, vol. 12, pp. 1–89.

[82] S. Warach, J. Gaa, B. Siewert, P. Wielopolski, and R. R. Edelman, "Acute human stroke studied by whole brain echo planar diffusion-weighted magnetic resonance imaging," *Ann Neurol*, vol. 37, no. 2, pp. 231–241, 1995.

[83] P. J. Basser and C. Pierpaoli, "Microstructural and physiological features of tissues elucidated by quantitative-diffusion-tensor MRI," *J. Magn. Reson. B*, vol. 111, pp. 209–219, 1996.

[84] D. K. Jones, A. Simmons, S. C. R. Williams, and M. A. Horsfield, "Non-invasive assessment of axonal fiber connectivity in the human brain via diffusion tensor MRI," *Magn. Reson. Med.*, vol. 42, pp. 37–41, 1999.

[85] C. Poupon, J.-F. Mangin, V. Frouin, J. Régis, D. Le Bihan, and I. Bloch, "Towards inference of human brain connectivity from MR diffusion tensor data," *Med. Image Anal.*, vol. 5, pp. 1–15, 2001.

[86] M. A. Koch, D. G. Norris, and M. Hund-Georgiadis, "An investigation of functional and anatomical connectivity using magnetic resonance imaging," *NeuroImage*, vol. 16, pp. 241–250, 2002.

[87] D. C. Alexander, P. L. Hubbard, M. G. Hall, E. A. Moore, M. Ptito, G. J. M. Parker, and T. B. Dyrby, "Orientationally invariant indices of axon diameter and density from diffusion MRI," *Neuroimage*, vol. 52, pp. 1374–1389, 2010.

[88] Y. Assaf, A. Mayk, and Y. Cohen, "Displacement imaging of spinal cord using q-space diffusion-weighted MRI," *Magn. Reson. Med.*, vol. 44, pp. 713–722, 2000.

[89] Y. Assaf, D. Ben-Bashat, J. Chapman, S. Peled, I. E. Biton, M. Kafri, Y. Segev, T. Hendler, A. D. Korczyn, M. Graif, and Y. Cohen, "High b-value q-space analyzed diffusion-weighted MRI: Application to multiple sclerosis," *Magn. Reson. Med.*, vol. 47, pp. 115–126, 2002.

[90] C. Beaulieu, "The basis of anisotropic water diffusion in the nervous system - a technical review," *NMR Biomed.*, vol. 15, pp. 435–455, 2002.

[91] P. T. Callaghan, C. D. Eccles, and Y. Xia, "NMR microscopy of dynamic displacements: k-space and q-space imaging," *J. Phys. E*, vol. 21, pp. 820–822, 1988.

[92] D. G. Cory and A. N. Garroway, "Measurement of translational displacement probabilities by NMR: An indicator of compartmentation," *Magn. Reson. Med.*, vol. 14, pp. 435–444, 1990.

[93] H. H. Ong, A. C. Wright, S. L. Wehrli, A. Souza, E. D. Schwartz, S. N. Hwang, and F. W. Wehrli, "Indirect measurementof regional axon diameter in excised mouse spinal cord with q-space imaging: Simulation and experimental studies," *NeuroImage*, vol. 40, no. 4, pp. 1619–1632, 2008.

[94] A. Bar-Shir, I. D. Duncan, and Y. Cohen, "QSI and DTI of excised brains of the myelin-deficient rat," *NeuroImage*, vol. 48, no. 1, pp. 109–116, 2009.

[95] I. E. Biton, A. Mayk, D. Kidron, Y. Assaf, and Y. Cohen, "Improved detectability of experimental allergic encephalomyelitis in excised swine spinal cords by high b-value q-space DWI," *Exp. Neurol.*, vol. 195, no. 2, pp. 437–446, 2005.

[96] P. P. Mitra and B. I. Halperin, "Effects of finite gradient-pulse widths in pulsed-field-gradient diffusion measurements," *J. Magn. Reson. A*, vol. 113, pp. 94–101, 1995.

[97] G. J. Stanisz, A. Szafer, G. A. Wright, and R. M. Henkelman, "An analytical model of restricted diffusion in bovine optic nerve," *Magn. Reson. Med.*, vol. 37, pp. 103–111, 1997.

[98] T. E. J. Behrens, M. W. Woolrich, M. Jenkinson, H. Johansen-Berg, R. G. Nunes, S. Clare, P. M. Matthews, J. M. Brady, and S. M. Smith, "Characterization and propagation of uncertainty in diffusion-weighted MR imaging," *Magn. Reson. Med.*, vol. 50, pp. 1077–1088, 2003.

[99] T. Behrens, H. J. Berg, S. Jbabdi, M. Rushworth, and M. Woolrich, "Probabilistic diffusion tractography with multiple fibre orientations: What can we gain?" *NeuroImage*, vol. 34, no. 1, pp. 144–155, 2007.

[100] Y. Assaf, R. Z. Freidlin, G. K. Rohde, and P. J. Basser, "New modeling and experimental framework to characterize hindered and restricted water diffusion in brain white matter," *Magn. Reson. Med.*, vol. 52, pp. 965–978, 2004.

[101] Y. Assaf and P. J. Basser, "Composite hindered and restricted model of diffusion (CHARMED) MR imaging of the human brain," *NeuroImage*, vol. 27, pp. 48–58, 2005.

[102] Y. Assaf, T. Blumenfeld-Katzir, Y. Yovel, and P. J. Basser, "AxCaliber: A method for measuring axon diameter distribution from diffusion MRI," *Magn. Reson. Med.*, vol. 59, pp. 1347–1354, 2008.

[103] F. Aboitiz, A. B. Scheibel, R. S. Fisher, and E. Zaidel, "Fiber composition of the human corpus callosum," *Brain Res.*, vol. 598, pp. 143–153, 1992.

[104] P. J. B. Daniel Barazany and Y. Assaf, "In vivo measurement of axon diameter distribution in the corpus callosum of rat brain," *Brain*, vol. 132, pp. 1210–1220, 2009.

[105] D. C. Alexander, "A general framework for experiment design in diffusion MRI and its application in measuring direct tissue-microstructure features," *Magn. Reson. Med.*, vol. 60, no. 2, pp. 439–448, 2008.

[106] D. Jones, D. Alexander, R. Bowtell, M. Cercignani, F. Dell'Acqua, D. McHugh, K. Miller, M. Palombo, G. Parker, U. Rudrapatna, and C. Tax, "Microstructural imaging of the human brain with a 'super-scanner': 10 key advantages of ultra-strong gradients for diffusion MRI," *NeuroImage*, vol. 182, pp. 8–38, 2018.

[107] M. A. Koch and J. Finsterbusch, "Compartment size estimation with double wave vector diffusion-weighted imaging," *Magn. Reson. Med.*, vol. 60, pp. 90–101, 2008.

[108] E. Özarslan and P. J. Basser, "Microscopic anisotropy revealed by NMR double pulsed field gradient experiments with arbitrary timing parameters," *J. Chem. Phys.*, vol. 128, p. 154511, 2008.

[109] J. Finsterbusch, "Multiple-wave-vector diffusion-weighted NMR," in *Annual Reports on NMRSpectroscopy*, G. A. Webb, Ed. Burlington: Academic Press, 2011, vol. 72, ch. 6, pp. 225–299.

[110] P. T. Callaghan and I. Furó, "Diffusion-diffusion correlation and exchange as a signature for local order and dynamics," *J. Chem. Phys.*, vol. 120, no. 8, pp. 4032–4038, 2004.

[111] E. Özarslan, U. Nevo, and P. J. Basser, "Anisotropy induced by macroscopic boundaries: surface-normal mapping using diffusion-weighted imaging," *Biophys. J.*, vol. 94, pp. 2809–2818, 2008.

[112] M. E. Komlosh, F. Horkay, R. Z. Freidlin, U. Nevo, Y. Assaf, and P. J. Basser, "Detection of microscopic anisotropy in gray matter and in a novel tissue phantom using double pulsed gradient spin echo MR," *J. Magn. Reson.*, vol. 189, pp. 38–45, 2007.

[113] E. Özarslan, "Compartment shape anisotropy (CSA) revealed by double pulsed field gradient MR," *J. Magn. Reson.*, vol. 199, pp. 56–67, 2009.

[114] S. N. Jespersen, "Equivalence of double and single wave vector diffusion contrast at low diffusion weighting," *NMR Biomed.*, vol. 25, pp. 813–818, 2012.

[115] S. N. Jespersen, H. Lundell, C. K. Sønderby, and T. B. Dyrby, "Orientationally invariant metrics of apparent compartment eccentricity from double pulsed field

gradient diffusion experiments," *NMR Biomed.*, vol. 26, no. 12, pp. 1647–1662, 2013, erratum: NMR Biomed. 27, 738 (2014).

[116] N. Shemesh, D. Barazany, O. Sadan, L. Bar, Y. Zur, Y. Barhum, N. Sochen, D. Offen, Y. Assaf, and Y. Cohen, "Mapping apparent eccentricity and residual ensemble anisotropy in the gray matter using angular double-pulsed-field-gradient MRI," *Magn. Reson. Med.*, vol. 68, pp. 794–806, 2012.

[117] Y. Cheng and D. G. Cory, "Multiple scattering by NMR," *J. Am. Chem. Soc.*, vol. 121, pp. 7935–7936, 1999.

[118] M. E. Komlosh, M. J. Lizak, F. Horkay, R. Z. Freidlin, and P. J. Basser, "Observation of microscopic diffusion anisotropy in the spinal cord using double-pulsed gradient spin echo MRI," *Magn. Reson. Med.*, vol. 59, pp. 803–809, 2008.

[119] N. Shemesh and Y. Cohen, "Microscopic and compartment shape anisotropies in gray and white matter revealed by angular bipolar double-PFG MR," *Magn. Reson. Med.*, vol. 65, pp. 1216–1227, 2011.

[120] N. Shemesh, T. Adiri, and Y. Cohen, "Probing microscopic architecture of opaque heterogeneous systems using double-pulsed-field-gradient NMR," *J. Am. Chem. Soc.*, vol. 133, pp. 6028–6035, 2011.

[121] M. Lawrenz and J. Finsterbusch, "Detection of microscopic diffusion anisotropy on a whole-body MR system with double wave vector imaging," *Magn. Reson. Med.*, vol. 66, pp. 1405–1415, 2011.

[122] A. V. Avram, E. Özarslan, J. E. Sarlls, and P. J. Basser, "In vivo detection of microscopic anisotropy using quadruple pulsed-field gradient (qPFG) diffusion MRI on a clinical scanner," *NeuroImage*, vol. 64, pp. 229–239, 2013.

[123] M. Lawrenz and J. Finsterbusch, "Double-wave-vector diffusion-weighted imaging reveals microscopic diffusion anisotropy in the living human brain," *Magn. Reson. Med.*, vol. 69, pp. 1072–1082, 2013.

[124] M. Lawrenz, S. Brassen, and J. Finsterbusch, "Microscopic diffusion anisotropy in the human brain: Reproducibility, normal values, and comparison with the fractional anisotropy," *NeuroImage*, vol. 109, pp. 283–297, 2015.

[125] M. Lawrenz and J. Finsterbusch, "Mapping measures of microscopic diffusion anisotropy in human brain white matter in vivo with double-wave-vector

diffusion-weighted imaging." *Magn. Reson. Med.*, vol. 73, no. 2, pp. 773–783, 2015.

[126] M. A. Koch and J. Finsterbusch, "Numerical simulation of double-wave vector experiments investigating diffusion in randomly oriented ellipsoidal pores," *Magn. Reson. Med.*, vol. 62, pp. 247–254, 2009.

[127] N. Shemesh, E. Özarslan, T. Adiri, P. J. Basser, and Y. Cohen, "Noninvasive bipolar double-pulsed-field-gradient NMR reveals signatures for pore size and shape in polydisperse, randomly oriented, inhomogeneous porous media," *J. Chem. Phys.*, vol. 133, p. 044705, 2010.

[128] N. Shemesh, J. T. Rosenberg, J.-N. Dumez, J. A. Muniz, S. C. Grant, and L. Frydman, "Metabolic properties in stroked rats revealed by relaxation-enhanced magnetic resonance spectroscopy at ultrahigh fields." *Nat. Commun.*, vol. 5, p. 4958, 2014.

[129] Y. Grant, T. Qiyuan, L. Christoph, W. Max, and M. J. A., "Double diffusion encoding MRI for the clinic," *Magn. Reson. Med.*, vol. 80, no. 2, pp. 507–520, 2018.

[130] N. Shemesh, E. Özarslan, P. J. Basser, and Y. Cohen, "Measuring small compartmental dimensions with low-q angular double-PGSE NMR: The effect of experimental parameters on signal decay," *J. Magn. Reson.*, vol. 198, pp. 15–23, 2009.

[131] J. Finsterbusch, "The parallel–antiparallel signal difference in double-wave-vector diffusion-weighted MR at short mixing times: A phase evolution perspective," *J. Magn. Reson.*, vol. 208, pp. 114–121, 2011.

[132] E. Özarslan, N. Shemesh, and P. J. Basser, "A general framework to quantify the effect of restricted diffusion on the NMR signal with applications to double pulsed field gradient NMR experiments," *J. Chem. Phys.*, vol. 130, p. 104702, 2009.

[133] D. Benjamini, Y. Katz, and U. Nevo, "A proposed 2D framework for estimation of pore size distribution by double pulsed field gradient NMR," *J. Chem. Phys.*, vol. 137, no. 22, p. 224201, 2012.

[134] A. Ianuş, I. Drobnjak, and D. C. Alexander, "Model-based estimation of microscopic anisotropy using diffusion MRI: a simulation study," *NMR Biomed*, vol. 29, no. 5, pp. 672–685, 2016.

[135] M. E. Komlosh, E. Özarslan, M. J. Lizak, F. Horkay, V. Schram, N. Shemesh, Y. Cohen, and P. J. Basser, "Pore diameter mapping using double pulsed-field

gradient MRI and its validation using a novel glass capillary array phantom," *J. Magn. Reson.*, vol. 208, pp. 128–135, 2011.

[136] N. Shemesh, E. Özarslan, P. J. Basser, and Y. Cohen, "Accurate noninvasive measurement of cell size and compartment shape anisotropy in yeast cells using double-pulsed field gradient MR," *NMR Biomed.*, vol. 25, no. 2, pp. 236–246, 2012.

[137] T. Weber, C. H. Ziener, T. Kampf, V. Herold, W. R. Bauer, and P. M. Jakob, "Measurement of apparent cell radii using a multiple wave vector diffusion experiment," *Magn. Reson. Med.*, vol. 61, pp. 1001–1006, 2009.

[138] D. Morozov, L. Bar, and Y. Sochen, N. Cohen, "Microstructural information from angular double-pulsed-field-gradient NMR: From model systems to nerves," *Magn. Reson. Med.*, vol. 74, pp. 25–32, 2015.

[139] D. Benjamini, M. E. Komlosh, L. A. Holtzclaw, U. Nevo, and P. J. Basser, "White matter microstructure from nonparametric axon diameter distribution mapping," *NeuroImage*, vol. 135, pp. 333–344, 2016.

[140] S. N. Jespersen and N. Buhl, "The displacement correlation tensor: Microstructure, ensemble anisotropy and curving fibers," *J. Magn. Reson.*, vol. 208, pp. 34–43, 2011.

[141] S. N. Jespersen, "Comment on "Measuring small compartments with relatively weak gradients by angular double-pulsed-field-gradient NMR" by Morozov, Bar, Sochen, and Cohen," *Magn. Reson. Imaging*, vol. 31, no. 9, pp. 1643–1644, 2013.

[142] D. Morozov, L. Bar, N. Sochen, and Y. Cohen, "Measuring small compartments with relatively weak gradients by angular double-pulsed-field-gradient NMR," *Magn. Reson. Imaging*, vol. 31, no. 3, pp. 401–407, 2013.

[143] Y. Katz and U. Nevo, "Quantification of pore size distribution using diffusion NMR: Experimental design and physical insights," *J. Chem. Phys.*, vol. 140, no. 16, p. 164201, 2014.

[144] D. Benjamini, M. E. Komlosh, P. J. Basser, and U. Nevo, "Nonparametric pore size distribution using d-PFG: Comparison to s-PFG and migration to MRI," *J. Magn. Reson.*, vol. 246, pp. 36–45, 2014.

[145] M. Goldman and L. Shen, "Spin-spin relaxation in LaF_3," *Phys. Rev.*, vol. 144, pp. 321–331, 1966.

[146] M. Voda, D. Demco, A. Voda, T. Schauber, M. Adler, T. Dabisch, A. Adams, M. Baias, and B. Blümich, "Morphology of thermoplastic polyurethanes by 1H spin-diffusion NMR," *Macromolecules*, vol. 39, no. 14, pp. 4802–4810, 2006.

[147] D. E. Demco, A. Johansson, and J. Tegenfeldt, "Proton spin diffusion for spatial heterogeneity and morphology investigations of polymers," *Solid State Nucl. Magn. Reson.*, vol. 4, no. 1, pp. 13–38, 1995.

[148] A. Ianuş, S. N. Jespersen, T. S. Duarte, D. C. Alexander, I. Drobnjak, and N. Shemesh, "Accurate estimation of microscopic diffusion anisotropy and its time dependence in the mouse brain," *NeuroImage*, vol. 183, pp. 934–949, 2018.

[149] N. Shemesh, "Axon diameters and myelin content modulate microscopic fractional anisotropy at short diffusion times in fixed rat spinal cord," *Front. Phys.*, vol. 6, p. 49, 2018.

[150] N. Shemesh and Y. Cohen, "The effect of experimental parameters on the signal decay in double-PGSE experiments: negative diffractions and enhancement of structural information," *J. Magn. Reson.*, vol. 195, pp. 153–161, 2008.

[151] N. Shemesh, E. Özarslan, A. Bar-Shir, P. J. Basser, and Y. Cohen, "Observation of restricted diffusion in the presence of a free diffusion compartment: single- and double-PFG experiments," *J. Magn. Reson.*, vol. 200, pp. 214–225, 2009.

[152] M. Lawrenz, M. A. Koch, and J. Finsterbusch, "A tensor model and measures of microscopic anisotropy for double-wave-vector diffusion-weighting experiments with long mixing times," *J. Magn. Reson.*, vol. 202, pp. 43–56, 2010.

[153] N. Shemesh, E. Özarslan, P. J. Basser, and Y. Cohen, "Detecting diffusion-diffraction patterns in size distribution phantoms using double-pulsed field gradient NMR: Theory and experiments," *J. Chem. Phys.*, vol. 132, p. 034703, 2010.

[154] G. Sobue, Y. Hashizume, T. Mitsuma, and A. Takahashi, "Size-dependent myelinated fiber loss in the corticospinal tract in shy-drager syndrome and amyotrophic lateral sclerosis," *Neurology*, vol. 37, pp. 529–532, 1987.

[155] N. Shemesh and Y. Cohen, "Overcoming apparent susceptibility-induced anisotropy (aSIA) by bipolar double-pulsed-field-gradient NMR," *J. Magn. Reson.*, vol. 212, no. 2, pp. 362–369, 2011.

[156] R. Bai, Z. Li, C. Sun, Y.-C. Hsu, H. Liang, and P. Basser, "Feasibility of filter-exchange imaging (FEXI) in measuring different exchange processes in human brain," *NeuroImage*, vol. 219, p. 117039, 2020.

[157] G. Zheng and W. S. Price, "Suppression of background gradients in (B_0 gradient-based) NMR diffusion experiments," *Concepts Magn. Reson. A*, vol. 30A, pp. 261–277, 2007.

[158] P. T. Callaghan, *Translational dynamics and magnetic resonance: principles of pulsed gradient spin echo NMR*. Oxford New York: Oxford University Press, 2011.

[159] J. Zhong, R. P. Kennan, and J. C. Gore, "Effects of susceptibility variations on NMR measurements of diffusion," *J. Magn. Reson.*, vol. 95, no. 2, pp. 267–280, 1991.

[160] W. S. Price, P. Stilbs, B. Jönsson, and O. Söderman, "Macroscopic background gradient and radiation damping effects on high-field PGSE NMR diffusion measurements," *J. Magn. Reson.*, vol. 150, pp. 49–56, 2001.

[161] J. Pipe, "Pulse sequences for diffusion-weighted MRI," in *Diffusion MRI. From quantitative measurement to in vivo neuroanatomy*, second edition ed., H. Johansen-Berg and T. E. Behrens, Eds. San Diego: Academic Press, 2014, pp. 11–34.

[162] D. L. Bihan, C. Poupon, A. Amadon, and F. Lethimonnier, "Artifacts and pitfalls in diffusion MRI," *J. Magn. Reson. Imaging*, vol. 24, pp. 478–488, 2006.

[163] O. Rodrigues, "Des lois géométriques qui regíssent les déplacements d'un systéme solide dans l'espace et de la variation des coordonnées provenant de ses déplacements considérés indépendamment des causes qui peuvent les produire," *J. Math. Pures Appl.*, vol. 5, pp. 380–440, 1840.

[164] G. Wesbey, M. Moseley, and R. Ehman, "Translational molecular self-diffusion in magnetic resonance imaging. II. Measurement of the self-diffusion coefficient," *Invest. Radiol*, vol. 19, no. 6, pp. 491–498, 1984.

[165] W. S. Price, "Pulsed-field gradient nuclear magnetic resonance as a tool for studying translational diffusion: Part II. experimental aspects," *Concepts Magn. Reson.*, vol. 10, pp. 197–237, 1998.

[166] M. Neeman, J. P. Freyer, and L. O. Sillerud, "A simple method for obtaining cross-term-free images for diffusion anisotropy studies in NMR microimaging," *Magn. Reson. Med.*, vol. 21, pp. 138–143, 1991.

[167] J. Lian, D. Williams, and I. Lowe, "Magnetic resonance imaging of diffusion in the presence of background gradients and imaging of background gradients," *J. Magn. Reson.*, vol. 106, no. 1, pp. 65–74, 1994.

[168] Z. H. Endre, P. W. Kuchel, and B. E. Chapman, "Cell volume dependence of 1H spin-echo NMR signals in human erythrocyte suspensions: The influence of in situ field gradients," *Biochim. Biophys. Acta*, vol. 803, no. 3, pp. 137–144, 1984.

[169] W. D. Williams, E. Seymour, and R. Cotts, "A pulsed-gradient multiple-spin-echo NMR technique for measuring diffusion in the presence of background magnetic field gradients," *J. Magn. Reson.*, vol. 31, no. 2, pp. 271–282, 1978.

[170] L. L. Latour, L. Li, and C. H. Sotak, "Improved PFG stimulated-echo method for the measurement of diffusion in inhomogeneous fields," *J. Magn. Reson. B*, vol. 101, pp. 72–77, 1993.

[171] J. Trudeau, W. Dixon, and J. Hawkins, "The effect of inhomogeneous sample susceptibility on measured diffusion anisotropy using NMR imaging," *J. Magn. Reson. B*, vol. 108, no. 1, pp. 22–30, 1995.

[172] D. Benjamini and U. Nevo, "Estimation of pore size distribution using concentric double pulsed-field gradient NMR," *J. Magn. Reson.*, vol. 230, pp. 198–204, 2013.

[173] D. Benjamini, J. J. Elsner, M. Zilberman, and U. Nevo, "Pore size distribution of bioresorbable films using a 3-D diffusion NMR method," *Acta Biomater.*, vol. 10, no. 6, pp. 2762–2768, 2014.

[174] D. Topgaard, "Isotropic diffusion weighting using a triple-stimulated echo pulse sequence with bipolar gradient pulse pairs," *Micropor. Mesopor. Mat.*, vol. 205, pp. 48–51, 2015.

[175] D. Morozov, L. Bar, N. Sochen, and Y. Cohen, "Pore sizes and directionality in microcapillaries from angular double-pulsed-field-gradient NMR," *Micropor. Mesopor. Mat.*, vol. 225, pp. 105–115, 2016.

[176] N. Shemesh, J. T. Rosenberg, J.-N. Dumez, S. C. Grant, and L. Frydman, "Distinguishing neuronal from astrocytic subcellular microstructures using in vivo double diffusion encoded 1H MRS at 21.1 T," *PLOS ONE*, vol. 12, no. 10, pp. 1–19, 10 2017.

[177] M. Lawrenz and J. Finsterbusch, "Detection of microscopic diffusion anisotropy in human cortical gray matter in vivo with double diffusion encoding," *Magn. Reson. Med.*, vol. 81, no. 2, pp. 1296–1306, 2018.

[178] M. A. Koch and J. Finsterbusch, "In vivo pore size estimation in white matter with double wave vector diffusion weighting," in *Proc. Joint Annual Meeting ISMRM/ESMRMB, Stockholm, Sweden*, 2010, p. 194.

[179] A. Wetscherek, B. Stieltjes, and F. B. Laun, "Flow-compensated intravoxel incoherent motion diffusion imaging," *Magn. Reson. Med.*, vol. 74, no. 2, pp. 410–419, 2015.

[180] L. Preuße, *Effekte durch Hintergrundgradienten in der diffusionsgewichteten MRT*. Bachelor Thesis – University of Lübeck, 2016.

[181] M. Drake-Pérez, J. Boto, A. Fitsiori, K. Lovblad, and M. Vargas, "Clinical applications of diffusion weighted imaging in neuroradiology," *Insights Imaging*, vol. 9, no. 4, pp. 535–547, 2018.

[182] C. Mekkaoui, T. G. Reese, M. P. Jackowski, H. Bhat, and D. E. Sosnovik, "Diffusion MRI in the heart," *NMR Biomed*, vol. 30, no. 3, p. e3426, 2017.

[183] S. C. Partridge, N. Nissan, H. Rahbar, A. E. Kitsch, and E. E. Sigmund, "Diffusion-weighted breast MRI: Clinical applications and emerging techniques," *J. Magn. Reson. Imaging*, vol. 45, no. 2, pp. 337–355, 2017.

[184] J. Ye, B. S. Kumar, X.-b. Li, H.-m. Li, Y.-w. Zhou, and L.-q. Liu, "Clinical applications of diffusion-weighted magnetic resonance imaging in diagnosis of renal lesions - a systematic review," *Clin. Physiol. Funct. Imaging*, vol. 37, no. 5, pp. 459–473, 2017.

[185] D. C. Alexander, T. B. Dyrby, M. Nilsson, and H. Zhang, "Imaging brain microstructure with diffusion MRI: practicality and applications," *NMR Biomed*, vol. 32, no. 4, p. e3841, 2019.

[186] P. T. Callaghan and B. Manz, "Velocity exchange spectroscopy," *J. Magn. Reson. A*, vol. 106, pp. 260–265, 1994.

[187] A. Ahlgren, L. Knutsson, R. Wirestam, M. Nilsson, F. Ståhlberg, D. Topgaard, and S. Lasič, "Quantification of microcirculatory parameters by joint analysis of flow-compensated and non-flow-compensated intravoxel incoherent motion (IVIM) data," *NMR Biomed.*, vol. 29, no. 5, pp. 640–649, 2016.

[188] M. E. Komlosh, E. Özarslan, M. J. Lizak, I. Horkayne-Szakaly, R. Z. Freidlin, F. Horkay, and P. J. Basser, "Mapping average axon diameters in porcine spinal cord white matter and rat corpus callosum using d-PFG MRI," *NeuroImage*, vol. 78, pp. 210–216, 2013.

[189] E. Özarslan, M. E. Komlosh, M. J. Lizak, F. Horkay, and P. J. Basser, "Double pulsed field gradient (double-PFG) MR imaging (MRI) as a means to measure the size of plant cells," *Magn. Reson. Chem.*, vol. 49, pp. S79–S84, 2011.

[190] M. A. Koch and J. Finsterbusch, "Double wave vector diffusion weighting in Wallerian degeneration," 2012, p. 3564.

[191] P. T. Callaghan and M. E. Komlosh, "Locally anisotropic motion in a macroscopically isotropic system: displacement correlations measured using double pulsed gradient spin-echo NMR," *Magn. Reson. Chem.*, vol. 40, pp. S15–S19, 2002.

[192] F. B. Laun, T. A. Kuder, A. Wetscherek, B. Stieltjes, and W. Semmler, "NMR-based diffusion pore imaging," *Phys. Rev. E*, vol. 86, p. 021906, 2012.

[193] I. Drobnjak, B. Siow, and D. C. Alexander, "Optimizing gradient waveforms for microstructure sensitivity in diffusion-weighted MR," *J. Magn. Reson.*, vol. 206, no. 1, pp. 41–51, 2010.

[194] I. Drobnjak, H. Zhang, M. G. Hall, and D. C. Alexander, "The matrix formalism for generalised gradients with time-varying orientation in diffusion NMR," *J. Magn. Reson.*, vol. 210, pp. 151–157, 2011.

[195] A. Ianuş, B. Siow, I. Drobnjak, H. Zhang, and D. C. Alexander, "Gaussian phase distribution approximations for oscillating gradient spin echo diffusion MRI," *J. Magn. Reson.*, vol. 227, pp. 25–34, Feb 2013.

[196] P. T. Callaghan, "A simple matrix formalism for spin echo analysis of restricted diffusion under generalized gradient waveforms," *J. Magn. Reson.*, vol. 129, pp. 74–84, 1997.

[197] H. Weingärtner, "Self diffusion in liquid water. A reassessment," *Z. Phys. Chem.*, vol. 132, pp. 129–149, 1982.

[198] A. Leemans and D. K. Jones, "The B-matrix must be rotated when correcting for subject motion in DTI data," *Magn. Reson. Med.*, vol. 61, pp. 1336–1349, 2009.

[199] A. N. Dula, D. F. Gochberg, H. L. Valentine, W. M. Valentine, and M. D. Does, "Multiexponential T2, magnetization transfer, and quantitative histology in white matter tracts of rat spinal cord," *Magn. Reson. Med.*, vol. 63, no. 4, pp. 902–909, 2010.

[200] T. Duval, J. A. McNab, K. Setsompop, T. Witzel, T. Schneider, S. Y. Huang, B. Keil, E. C. Klawiter, L. L. Wald, and J. Cohen-Adad, "In vivo mapping of human spinal cord microstructure at 300 mT/m," *NeuroImage*, vol. 118, no. Supplement C, pp. 494–507, 2015.

[201] K. Kamiya, M. Hori, M. Miyajima, M. Nakajima, Y. Suzuki, K. Kamagata, M. Suzuki, H. Arai, K. Ohtomo, and S. Aoki, "Axon diameter and intra-axonal volume fraction of the corticospinal tract in idiopathic normal pressure hydrocephalus measured by Q-space imaging," *PLOS ONE*, vol. 9, no. 8, pp. 1–7, 2014.

[202] M. Werner, A. Chott, A. Fabiano, and H. Battifora, "Effect of formalin tissue fixation and processing on immunohistochemistry," *Am. J. Surg. Pathol.*, vol. 24, no. 7, pp. 1016–1019, 2000.

[203] H. Zhang, T. Schneider, C. A. Wheeler-Kingshott, and D. C. Alexander, "NODDI: Practical in vivo neurite orientation dispersion and density imaging of the human brain," *NeuroImage*, vol. 61, no. 4, pp. 1000–1016, 2012.

[204] F. Grussu, T. Schneider, H. Zhang, D. C. Alexander, and C. A. M. Wheeler-Kingshott, "Neurite orientation dispersion and density imaging of the healthy cervical spinal cord in vivo," *NeuroImage*, vol. 111, pp. 590–601, 2015.

[205] F. Grussu, T. Schneider, R. L. Yates, H. Zhang, C. A. M. Gandini Wheeler-Kingshott, G. C. DeLuca, and D. C. Alexander, "A framework for optimal whole-sample histological quantification of neurite orientation dispersion in the human spinal cord," *J. Neurosci. Methods*, vol. 273, pp. 20–32, 2016.

[206] M. A. Koch and P. Ulloa, "Determination of the pore size distribution by double diffusion encoding," *Front. Phys.*, no. 12, 2016.

[207] D. Graf von Keyserlingk and U. Schramm, "Diameter of axons and thickness of myelin sheaths of the pyramidal tract fibres in the adult human medullary pyramid," *Anat. Anz.*, vol. 157, no. 2, pp. 97–111, 1984.

[208] W. J. C. Verhaart, "On thick and thin fibers in the pyramidal tract," *Acta Psychiatr. Scand.*, vol. 22, no. 3–4, pp. 271–281, 1947.

[209] A. Saliani, B. Perraud, T. Duval, N. Stikov, S. Rossignol, and J. Cohen-Adad, "Axon and myelin morphology in animal and human spinal cord," *Front. Neuroanat.*, vol. 11, p. 129, 2017.

[210] M. A. Biedenbach, J. L. DeVito, and A. C. Brown, "Pyramidal tract of the cat: axon size and morphology," *Exp. Brain. Res.*, vol. 61, no. 2, pp. 303–310, 1986.

[211] M. Nilsson, S. Lasič, I. Drobnjak, D. Topgaard, and C.-F. Westin, "Resolution limit of cylinder diameter estimation by diffusion MRI: The impact of gradient waveform and orientation dispersion," *NMR Biomed.*, vol. 30, no. 7, p. e3711, 2017.

[212] A. Kertesz and N. Geschwind, "Patterns of pyramidal decussation and their relationship to handedness," *Arch. Neurol.*, vol. 24, no. 4, pp. 326–332, 1971.

[213] C. Büchel, T. Raedler, M. Sommer, M. Sach, C. Weiller, and M. A. Koch, "White matter asymmetry in the human brain: A diffusion tensor MRI study," *Cereb. Cortex*, vol. 14, pp. 945–951, 2004.

[214] D. S. Reich, S. A. Smith, C. K. Jones, K. M. Zackowski, P. C. van Zijl, P. A. Calabresi, and S. Mori, "Quantitative characterization of the corticospinal tract at 3T." *Am. J. Neuroradiol.*, vol. 27, no. 10, pp. 2168–2178, 2006.

[215] M. Sach, G. Winkler, V. Glauche, J. Liepert, B. Heimbach, M. A. Koch, C. Büchel, and C. Weiller, "Diffusion tensor MRI of early upper motor neuron involvement in amyotrophic lateral sclerosis," *Brain*, vol. 127, pp. 340–350, 2004.

[216] G. Thomalla, V. Glauche, M. A. Koch, C. Beaulieu, C. Weiller, and J. Röther, "Diffusion tensor imaging detects early Wallerian degeneration of the pyramidal tract after ischemic stroke," *NeuroImage*, vol. 22, pp. 1767–1774, 2004.

[217] M. J. Tait, S. Saadoun, B. A. Bell, and M. C. Papadopoulos, "Water movements in the brain: role of aquaporins," *Trends Neurosci.*, vol. 31, no. 1, pp. 37–43, 2008.

[218] Y. Qiao, P. Galvosas, and P. Callaghan, "Diffusion correlation NMR spectroscopic study of anisotropic diffusion of water in plant tissues," *Biophys J.*, vol. 89, no. 4, pp. 2899–2905, 2005.

[219] E. Panagiotaki, T. Schneider, B. Siow, M. G. Hall, M. F. Lythgoe, and D. C. Alexander, "Compartment models of the diffusion MR signal in brain white matter: A taxonomy and comparison," *NeuroImage*, vol. 59, pp. 2241–2254, 2012.

[220] C. A. Rosa and G. Péter, *Biodiversity and ecophysiology of yeasts*. Berlin: Springer-Verlag Berlin Heidelberg, 2006.

[221] W. Wu and K. L. Miller, "Image formation in diffusion MRI: A review of recent technical developments," *J. Magn. Reson. Imaging*, vol. 46, no. 3, pp. 646–662, 2017.

[222] S. Lasič, H. Lundell, D. Topgaard, and T. B. Dyrby, "Effects of imaging gradients in sequences with varying longitudinal storage time-case of diffusion exchange imaging," *Magn. Reson. Med.*, vol. 79, no. 4, pp. 2228–2235, 2017.

[223] T. Dyrby, H. Lundell, D. Topgaard, and S. Lasič, "Confounding effects of imaging gradients in stimulated echo: case of diffusion exchange imaging," *Front. Phys.*, no. 5, 2016.

[224] S. Lasič, S. N. Jespersen, H. Lundell, M. Nilsson, T. B. Dyrby, and D. Topgaard, "Apparent exchange rate in multi-compartment anisotropic tissue," *Front. Phys.*, no. 26, 2016.

[225] J. Piven, J. Bailey, B. Ranson, and S. Arndt, "An MRI study of the corpus callosum in autism," *Am. J. Psychiatry*, vol. 154, no. 8, pp. 1051–1056, 1997.

[226] F. Du, A. J. Cooper, T. Thida, A. K. Shinn, B. M. Cohen, and D. Öngür, "Myelin and axon abnormalities in schizophrenia measured with magnetic resonance imaging techniques," *Biol. Psychiatry*, vol. 74, no. 6, pp. 451–457, 2013.

[227] F. Fornasa, "Diffusion-weighted magnetic resonance imaging: What makes water run fast or slow?" *J. Clin. Imaging Sci.*, vol. 1, p. 27, 2011.

[228] G. M. Innocenti, R. Caminiti, and F. Aboitiz, "Comments on the paper by Horowitz et al. (2014)," *Brain Struct. Funct.*, vol. 220, no. 3, pp. 1789–1790, 2015.

[229] T. Zeuthen, "General models for water transport across leaky epithelia," in *Molecular Mechanisms of Water Transport Across Biological Membranes*, ser. Int. Rev. Cytol. Academic Press, 2002, vol. 215, pp. 285–317.

[230] S. Tripathi and E. L. Boulpaep, "Mechanisms of water transport by epithelial cells," *Q. J. Exp. Physiol.*, vol. 74, no. 4, pp. 385–417, 1989.

[231] M. C. Papadopoulos and A. S. Verkman, "Aquaporin-4 and brain edema," *Pediatr. Nephrol.*, vol. 22, no. 6, pp. 778–784, 2007.

[232] M. Nilsson, J. Lätt, E. Nordh, R. Wirestam, F. Ståhlberg, and S. Brockstedt, "On the effects of a varied diffusion time in vivo: is the diffusion in white matter restricted?" *Magn. Reson. Imaging*, vol. 27, pp. 176–187, 2009.

[233] D. K. Jones and M. Cercignani, "Twenty-five pitfalls in the analysis of diffusion MRI data," *NMR Biomed.*, vol. 23, pp. 803–820, 2010.

[234] D. Le Bihan, "Molecular diffusion, tissue microdynamics and microstructure," *NMR Biomed.*, vol. 8, pp. 375–86, 11 1995.

[235] P. J. Reber, E. C. Wong, R. B. Buxton, and L. R. Frank, "Correction of off resonance-related distortion in echo-planar imaging using EPI-based field maps," *Magn. Reson. Med.*, vol. 39, no. 2, pp. 328–330, 1998.

[236] P. S. Morgan, R. Bowtell, D. J. O. McIntyre, and B. S. Worthington, "Correction of spatial distortion in EPI due to inhomogeneous static magnetic fields using the reversed gradient method." *J. Magn. Reson. Imaging.*, vol. 19, pp. 499–507, 2004.

[237] K. V. Embleton, H. A. Haroon, D. M. Morris, M. A. L. Ralph, and G. J. Parker, "Distortion correction for diffusion-weighted MRI tractography and fMRI in the temporal lobes," *Hum. Brain Mapp.*, vol. 31, no. 10, pp. 1570–1587, 2010.

[238] R. Karlicek and I. Lowe, "A modified pulsed gradient technique for measuring diffusion in the presence of large background gradients," *J. Magn. Reson.*, vol. 37, no. 1, pp. 75–91, 1980.

[239] R. Cotts, M. Hoch, T. Sun, and J. Markert, "Pulsed field gradient stimulated echo methods for improved NMR diffusion measurements in heterogeneous systems," *J. Magn. Reson.*, vol. 83, no. 2, pp. 252–266, 1989.

[240] M. Neeman, J. P. Freyer, and L. O. Sillerud, "Pulsed-gradient spin-echo diffusion studies in NMR imaging. Effects of the imaging gradients on the determination of diffusion coefficients," *J. Magn. Reson.*, vol. 90, pp. 303–312, 1990.

[241] C. Meier, M. Zwanger, T. Feiweier, and D. Porter, "Concomitant field terms for asymmetric gradient coils: consequences for diffusion, flow, and echo-planar imaging," *Magn. Reson. Med.*, vol. 60, pp. 128–134, 2008.

[242] P. Jezzard, A. S. Barnett, and C. Pierpaoli, "Characterization of and correction for eddy current artifacts in echo planar diffusion imaging," *Magn. Reson. Med.*, vol. 39, no. 5, pp. 801–812, 1998.

[243] J.-Y. Chiou, O. Nalcioglu, L. Tugan Muftuler, and C. Beom Ahn, "Correction of shear artifact caused by unbalanced alternating readout gradient in echo-planar imaging," *Phys. Medica*, vol. 19, pp. 1214–1217, 2003.

[244] R. Bowtell and P. Mansfield, "Gradient coil design using active magnetic screening," *Magn. Reson. Med.*, vol. 17, no. 1, pp. 15–21, 1991.

[245] P. Mansfield and B. Chapman, "Multishield active magnetic screening of coil structures in NMR," *J. Magn. Reson.*, vol. 72, no. 2, pp. 211–223, 1987.

[246] S. J. Gibbs and C. S. Johnson, Jr., "A PFG NMR experiment for accurate diffusion and flow studies in the presence of eddy currents," *J. Magn. Reson.*, vol. 93, pp. 395–402, 1991.

[247] S. Mohammadi, H. E. Möller, H. Kugel, D. K. Müller, and M. Deppe, "Correcting eddy current and motion effects by affine whole-brain registrations: Evaluation of three-dimensional distortions and comparison with slicewise correction," *Magn. Reson. Med.*, vol. 64, no. 4, pp. 1047–1056, 2010.

[248] J. C. Haselgrove and J. R. Moore, "Correction for distortion of echo-planar images used to calculate the apparent diffusion coefficient," *Magn. Reson. Med.*, vol. 36, no. 6, pp. 960–964, 1996.

[249] N. Bodammer, J. Kaufmann, M. Kanowski, and C. Tempelmann, "Eddy current correction in diffusion-weighted imaging using pairs of images acquired with opposite diffusion gradient polarity," *Magn. Reson. Med.*, vol. 51, pp. 188–193, 2004.

[250] C. Boesch, R. Gruetter, and E. Martin, "Temporal and spatial analysis of fields generated by eddy currents in superconducting magnets: Optimization of corrections and quantitative characterization of magnet/gradient systems," *Magn. Reson. Med.*, vol. 20, no. 2, pp. 268–284, 1991.

[251] F. Calamante, D. A. Porter, D. G. Gadian, and A. Connelly, "Correction for eddy current induced B_0 shifts in diffusion-weighted echo-planar imaging," *Magn. Reson. Med.*, vol. 41, pp. 95–102, 1999.

[252] A. L. Alexander, J. S. Tsuruda, and D. L. Parker, "Elimination of eddy current artifacts in diffusion-weighted echo-planar images: The use of bipolar gradients," *Magn. Reson. Med.*, vol. 38, pp. 1016–1021, 1997.

[253] T. G. Reese, O. Heid, R. M. Weisskoff, and V. J. Wedeen, "Reduction of eddy-current-induced distortion in diffusion MRI using a twice-refocused spin echo," *Magn. Reson. Med.*, vol. 49, pp. 177–182, 2003.

[254] L. Mueller, A. Wetscherek, T. A. Kuder, and F. B. Laun, "Eddy current compensated double diffusion encoded (DDE) MRI," *Magn. Reson. Med.*, vol. 77, no. 1, pp. 328–335, 2017.

[255] D. C. Alexander, T. B. Dyrby, M. Nilsson, and H. Zhang, "Imaging brain microstructure with diffusion MRI: practicality and applications," *NMR Biomed.*, vol. 32, no. 4, p. e3841, 2019.

[256] K. J. Packer and C. Rees, "Pulsed NMR studies of restricted diffusion: I. Droplet size distributions in emulsions," *J. Colloid Interface Sci.*, vol. 40, pp. 206–218, 1972.

[257] K. Setsompop, R. Kimmlingen, E. Eberlein, T. Witzel, J. Cohen-Adad, J. McNab, B. Keil, M. Tisdall, P. Hoecht, P. Dietz, S. Cauley, V. Tountcheva, V. Matschl, V. Lenz, K. Heberlein, A. Potthast, H. Thein, J. V. Horn, A. Toga, F. Schmitt, D. Lehne, B. Rosen, V. Wedeen, and L. Wald, "Pushing the limits of in vivo diffusion MRI for the human connectome project," *NeuroImage*, vol. 80, pp. 220–233, 2013.

[258] S. Y. Huang, S. M. Tobyne, A. Nummenmaa, T. Witzel, L. L. Wald, J. A. McNab, and E. C. Klawiter, "Characterization of axonal disease in patients with multiple sclerosis using high-gradient-diffusion MR imaging," *Radiology*, vol. 280, no. 1, pp. 244–251, 2016.

[259] P. T. Callaghan, "NMR imaging, NMR diffraction and applications of pulsed gradient spin echoes in porous media," *Magn. Reson. Imaging*, vol. 14, pp. 701–709, 1996.

[260] A. Coy and P. T. Callaghan, "Pulsed gradient spin-echo NMR "diffusive diffraction" experiments on water surrounding close-packed polymer spheres," *J. Colloid Interface Sci.*, vol. 168, no. 2, pp. 373–379, 1994.

[261] N. S. White, C. R. McDonald, N. Farid, J. Kuperman, D. Karow, N. M. Schenker-Ahmed, H. Bartsch, R. Rakow-Penner, D. Holland, A. Shabaik, A. Bjørnerud, T. Hope, J. Hattangadi-Gluth, M. Liss, J. K. Parsons, C. C. Chen, S. Raman, D. Margolis, R. E. Reiter, L. Marks, S. Kesari, A. J. Mundt, C. J. Kane, B. S. Carter, W. G. Bradley, and A. M. Dale, "Diffusion-weighted imaging in cancer: Physical foundations and applications of restriction spectrum imaging," *Cancer Res.*, vol. 74, no. 17, pp. 4638–4652, 2014.

[262] E. Panagiotaki, S. Walker-Samuel, B. Siow, S. P. Johnson, V. Rajkumar, R. B. Pedley, M. F. Lythgoe, and D. C. Alexander, "Noninvasive quantification of solid tumor microstructure using VERDICT MRI," *Cancer Res.*, vol. 74, no. 7, pp. 1902–1912, 2014.

[263] E. Panagiotaki, R. W Chan, N. Dikaios, H. U Ahmed, J. O'Callaghan, A. Freeman, D. Atkinson, S. Punwani, D. J Hawkes, and D. Alexander, "Microstructural characterization of normal and malignant human prostate tissue with vascular, extracellular, and restricted diffusion for cytometry in tumours magnetic resonance imaging," *Invest. Radiol.*, vol. 50, pp. 218–227, 2015.

List of abbreviations

ADC apparent diffusion coefficient

AXR apparent exchange rate

BGG background gradient

CNS central nervous system

CST corticospinal tract

DTI diffusion tensor imaging

DDE double diffusion encoding

dMRI diffusion MRI

DW-MRI diffusion-weighted MRI

DWI diffusion-weighting imaging

EC eddy currents

EPI echo planar imaging

FEXI filter exchange imaging

FEXSI filter exchange spectroscopy

FID free induction decay

FOV field-of-view

FT fourier transform

MISST Microstructure Imaging Sequence Simulation ToolBox

MR magnetic resonance

MRI magnetic resonance imaging

PDF probability density function

NMR nuclear magnetic resonance

RF radiofrequency

ROI region-of-interest

SAR specific absorption rate

SDE single diffusion encoding

SNR signal-to-noise ratio

SE spin echo

SPIR spectral presaturation with inversion recovery

STE stimulated echo

TE echo time

TFE turbo field echo

TI inversion time

TR repetition time